Title of Thesis

Structural Design of Nanoporous Materials with Substance Formation on Two-Dimensional Materials Using Calcination

焼成による二次元物質上での物質形成を用いたナノポーラス材料の構造設計

March, 2025

Yuki Takeuchi

Graduate School of
Natural Science and Technology
(Doctor's Course)
OKAYAMA UNIVERSITY

Contents

Chapter 1. General introduction

1-1. Nanoporous materials

1-1-1. Characteristics of nanoporous materials

Owing to global warming in recent years, the achievement of carbon neutrality—a state of net-zero carbon emissions[1], has emerged as a societal goal. Accordingly, the development of environmentally friendly technologies and manufacturing processes, such as capturing and fixing greenhouse gases (e.g., CO_2)[2], and the construction of a system for producing chemicals (e.g., bioplastics)[3] and energy (e.g., H_2 production)[4] that do not rely on fossil resources, are required.

Nanoporous materials containing nanoscale pores exhibit high surface areas and large pore volumes. They have been applied to various fields, such as catalysts,[5] batteries,[6] separation membranes,[7] and adsorbents (e.g., CO_2).[8] Nanoporous materials support industries in environmental purification and material production. These materials include zeolite (Figure 1-1a),[9] activated carbon,[10] and metal–organic framework (MOF) (Figure 1-1b).[11] Studies on the fabrication of nanoporous materials with the desired pore size and surface structure that affect material performance have been actively conducted. According to the International Union of Pure and Applied Chemistry (IUPAC), pores are divided into three types: micropores (<2 nm), mesopores (2–50 nm), and macropores (>50 nm).[12] The functions of nanoporous materials can be controlled by adjusting the pore size. Microporous materials exhibit molecular sieving properties and strong adsorption at low-pressure regions because of the overlapping force fields between the pore walls.[13] Mesoporous materials possess high substance diffusivity in pores and modified properties of substances for catalytic and adsorption functions.[14,15] Moreover, macroporous materials have been used to recover relatively large adsorbates, such as viruses.[16]

In addition to the selection of the type of nanoporous materials, raw materials, and preparation conditions, typical examples of the methods for controlling the pore structure include the self-assembly strategy[17,18] and the templated synthesis described below. Designing the molecular structure of monomers (precursors) and their polymers is also employed to control the pore structure, including the covalent organic framework (COF, Figure 1-1c)) in organic polymers,[19] and MOF-derived carbon[20] and ordered carbonaceous frameworks[21,22] in carbon materials. To date,

various nanoporous materials have been constructed.

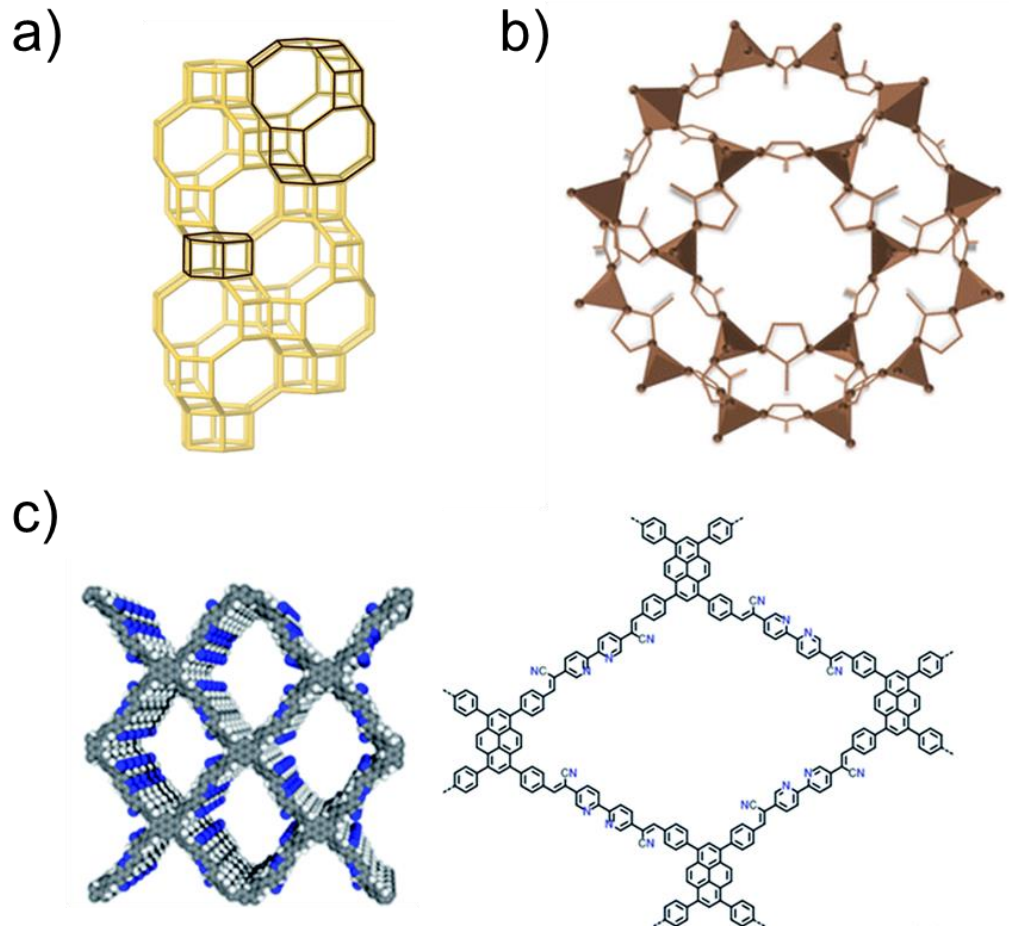

Figure 1-1. Nanoporous materials. a) Zeolite (chabazite), reproduced with permission from reference 23 (© 2024 The Authors, published by The Royal Society of Chemistry). b) MOF (zeolitic imidazole framework (ZIF-8)), reproduced with permission from reference 24 (© 2024 The Authors, published by The Royal Society of Chemistry). c) COF, reproduced with permission from reference 19 (© 2020 The Royal Society of Chemistry).

1-1-2. Analysis of nanoporous materials

Different methods have been used to conduct nanostructure analysis, including X-ray diffraction (XRD), small-angle X-ray scattering, small-angle neutron scattering, transmission electron spectroscopy (TEM), scanning electron microscopy (SEM), nuclear magnetic resonance

(NMR), and electron tomography (Figure 1-2). The analysis method was determined based on the target materials. For example, gas adsorption and mercury intrusion porosimetry were generally used to analyze the pore structure of nanoporous materials. In addition, gas adsorption was employed to analyze all micropores, mesopores, and macropores from a few Å to several 100 nm. Pores from large nanopores to 400 μm macropores were analyzed using mercury intrusion porosimetry.[25] Gas adsorption was used to analyze the materials with micropores and mesopores for this study. The analysis details are summarized in the IUPAC technical report[26] and the review written by Thommes et al.[25] In the gas adsorption method, physical adsorption is used to analyze the pore structure, and an extremely low temperature [boiling point of each substance N_2 (77 K) or Ar (87 K)] is used for the adsorbed gas.[26] In addition, by changing the gas type, various pore structures and properties (CO_2 for micropores, H_2O for hydrophilicity and hydrophobicity of the material surface, and Kr for the measurement of samples with a low specific surface area) can be analyzed.[26]

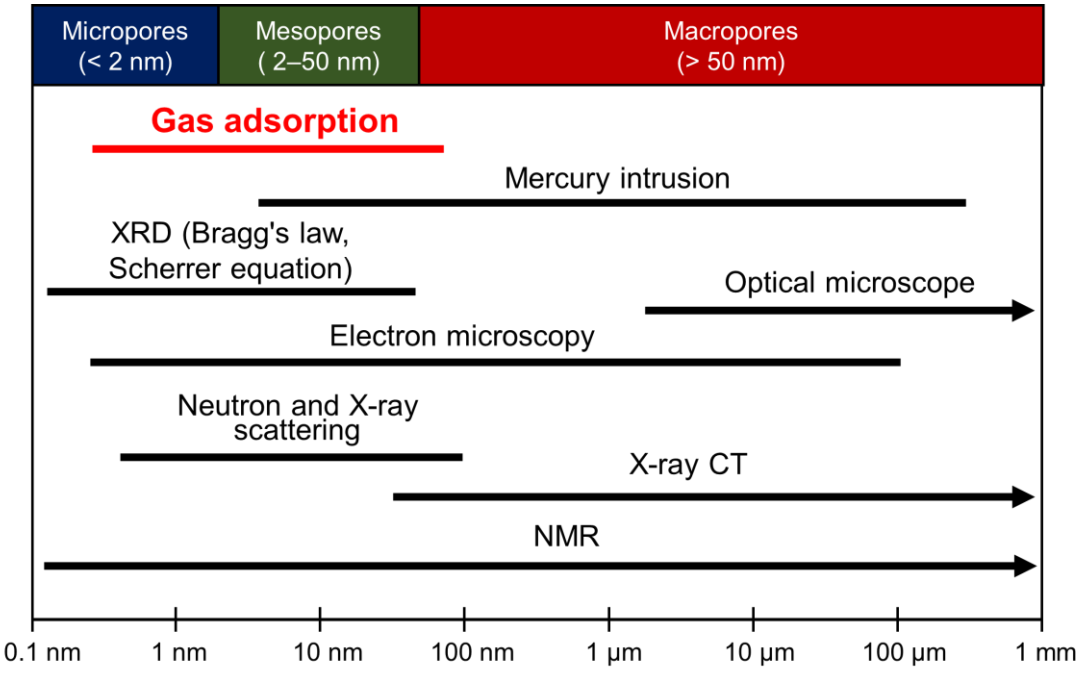

Figure 1-2. Characterization methods of the nanostructure of materials (nanoporous materials). Created using the information of reference 25 and 27.

In pore size analysis, the methods used to obtain the pore size distribution of micropores include the MP method,[28] derived from the slope of the *t*-plot compared with the adsorption layer thickness *t*, and the methods obtained from the average potential field inside the pores determined using the Lennard–Jones potential, including the Horvath and Kawazoe (HK) method for slit-shaped pores,[29] Saito and Foley method for cylindrical pores,[30] and Cheng and Yang method for spherical pores.[31] In addition, density functional theory (DFT) (non-local-DFT and quenched solid DFT method)[32] and molecular simulation (Grand Canonical Monte Carlo simulation)[33] have been proposed for more accurate and extensive analysis of the pore structures.

The Kelvin equation is generally applied to determine the pore size distribution of mesopores. The modified Kelvin equation for cylindrical pores, which represents the relationship between the relative pressure at which capillary condensation occurs and the Kelvin radius (r_k), is provided as follows:[26,34]

$$r_k = -\frac{2V_m\gamma\cos\theta}{RTln\left(\frac{p}{p_0}\right)}), \qquad (1.1)$$

where V_m is the molar volume of the adsorbates condensed in the pores at the measuring temperature, γ represents the surface tension, θ is the contact angle between the pore walls and the capillary condensate, R is the gas constant, and T represents the measuring temperature. The pore radius r_p can be obtained using the thickness t_{ad} of the adsorption layer when capillary condensation occurs and r_k:

$$r_p = r_k + t_{ad}. \qquad (1.2)$$

The Barrett, Joyner, and Halenda (BJH) method,[35] which is commonly used to obtain the pore size distribution of mesopores, is an analysis method based on the Kelvin equation described above. In addition, the Dollimore and Heal method[36] and the Cranston and Inkley method[37] are based on the Kelvin equation.

To analyze the specific surface areas of materials, the Brunauer–Emmett–Teller (BET) method is widely used. The specific surface areas in the BET method are calculated from the monolayer capacity as follows:[26]

$$a_s(\mathrm{BET}) = n_m \cdot L \cdot \sigma_m / m, \qquad (1.3)$$

where $a_s(\mathrm{BET})$ represents the BET-specific area, n_m is the specific monolayer capacity, L is the Avogadro constant, σ_m represents the molecular cross-sectional area, and m is the mass of the adsorbent. n_m is obtained using the following BET equation:[26]

$$\frac{p/p_0}{n(1-p/p_{0)}} = \frac{1}{n_m C} + \frac{C-1}{n_m C}(p/p_0), \qquad (1.4)$$

where n is the specific amount adsorbed at each relative pressure and C is the parameter exponentially related to the energy of monolayer adsorption.

1-2. Layered materials (nanosheet laminates) and nanosheets

Layered materials have a structure in which nanosheets, characterized by a two-dimensional structure with a nanoscale thickness, are stacked (Figure 1-3). Graphite and clay are typical examples of natural materials. Layered materials have a two-dimensional space between the nanosheets, and materials can be created for the storage and separation of targeted substances by transporting and storing substances in a two-dimensional space. Graphite has an interlayer structure suitable for the insertion and extraction of Li ions and is applied to anode materials of Li-ion batteries.[38] In addition, clay has a negatively charged structure and is used as an adsorbent for metal ions, such as Cs^+ ions.[39] Layered materials have excellent performance as a single substance. Further, the introduction of other substances between the layers can provide additional functions. Research on clay has been actively conducted for a long time. Graphene with a two-dimensional skeleton characterized by one carbon thickness was discovered in 2004.[40] Since then, research has been actively conducted on layered materials and nanosheets. In addition to graphite and negatively charged clay, other layered materials, such as layered double hydroxide, exhibit a positively charged surface and exchangeable anions,[41] and transition metal dichalcogenide (TMD) composed of transition metal and chalcogen atoms.[42]

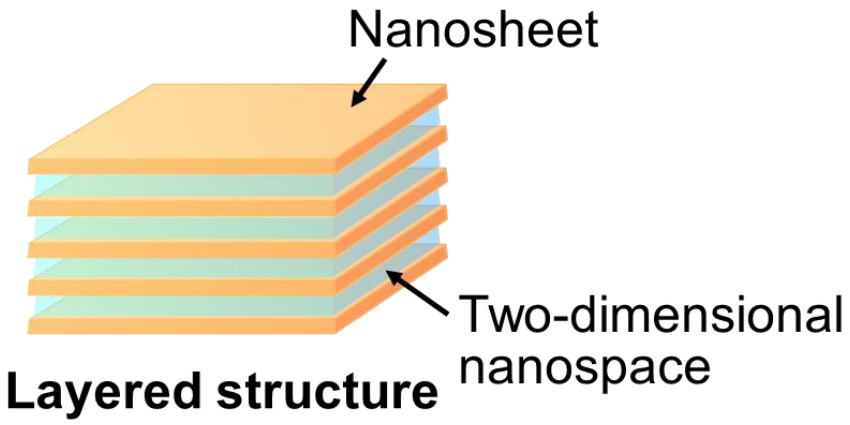

Figure 1-3. Pattern diagram of layered materials.

Nanosheets prepared by exfoliation of layered materials[43] or using the bottom-up method from a monomer[44] exhibit different features, such as two-dimensional structures, theoretically large surface areas, and high aspect ratios. By selecting and designing the composition and structure of nanosheets, it is possible to synthesize functional materials with excellent electronic, optical, magnetic, catalytic, and adsorption properties. In addition, two-dimensional nanospaces exist between the nanosheets. By controlling the properties of nanospaces (e.g., the size and affinity for target substances), nanoporous materials with various structures, such as high porosity and controlled pore structures, can be constructed. Research on the synthesis of porous (nanoporous) materials with nanosheets has utilized various approaches, such as the activation and exfoliation of nanosheets through chemical and thermal treatments,[45,46] pillarization by introducing substances between nanosheets,[47,48] and controlling the self-assembly of nanosheets (Figure 1-4).[49]

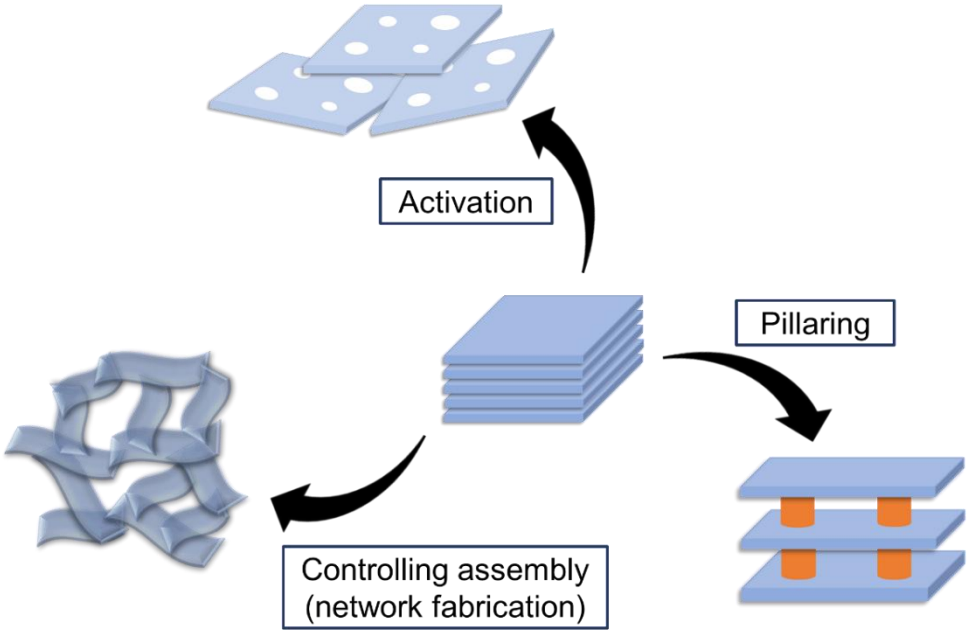

Figure 1-4. Preparation examples of porous (nanoporous) materials using nanosheets (layered materials).

1-2-1. Graphene oxide (GO)

Graphene, which is obtained by peeling graphite using scotch tape[40] and prepared using the chemical vapor deposition (CVD) method,[50] has different characteristics, including excellent thermal and electrical conductivity, theoretical large surface area, and high strength. GO, fabricated via the oxidation and exfoliation of graphite, is a two-dimensional material with diverse oxygen functional groups, such as epoxy, hydroxy, and carboxy groups (Figure 1-5).[51] The types of preparation methods including the Hummers method[52] and Brodie method[53] change the characteristics of GO such as the amounts and types of oxygen functional groups.[54] Given the presence of the functional groups and π–π interactions, GO has a high specific surface area, high mechanical strength, and functionalization properties.[55] However, GO has some issues, such as a decrease in porosity caused by stacking and embedding between sheets and a lack of permanent porosity, especially in the gas phase, due to changes in environmental conditions (e.g., humidity and pressure).[56,57] To date, robust porous structures derived from GO have been synthesized by constructing three-dimensional networks through the reduction of GO[58,59] and the centrifugal

vacuum evaporation of GO suspensions.[60] Given these properties, GO has been used in various applications, including catalyst supports[61,62] and energy storage devices, such as supercapacitors,[63,64] gas and virus sensors,[65,66] and adsorbents.[67,68]

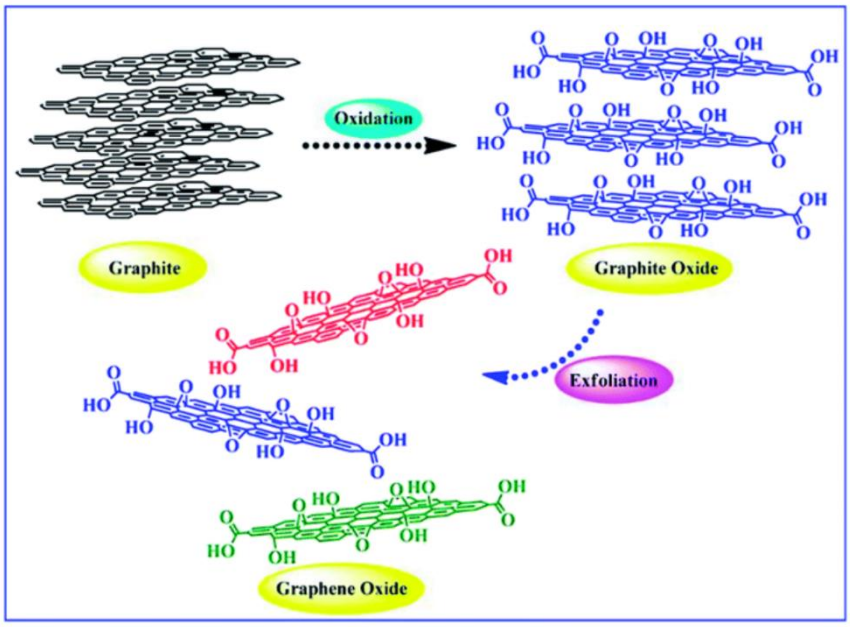

Figure 1-5. Pattern diagram of GO synthesis, reproduced with permission from reference 69 (© 2020 The Royal Society of Chemistry).

1-2-2. Clay

Clay is a natural material with abundant resources, is inexpensive, and has high chemical stability.[70] This material has been applied to various fields, such as adsorbents[71] and separation membranes.[72]

The name differs depending on the structure, including the ratio of the tetrahedral sheets composed of Si and O atoms and the octahedral sheets composed of Al and O atoms, as well as the shape. Montmorillonite (2:1 type layer, clay consisting of one octahedral sheet sandwiched between two tetrahedral sheets, Figure 1-6), kaolinite (1:1 type layer), and halloysite (1:1 type tube) are some examples of this material.[73] As a property of clay, swelling occurs when water enters the layers of clay, pushing them apart.[74] Furthermore, clay possesses a negative charge owing to the isomorphous substitution of structural cations of higher valence by others with lower

valence, resulting in exchangeable cations.[75,76] By using the electrostatic interaction between the negative charges in the layers of clay and the positive charges of metal ions and cationic molecules, metal–clay and organic–inorganic (clay) hybrids can be fabricated by exchanging cations and intercalating cationic molecules and polymers.[77–79]

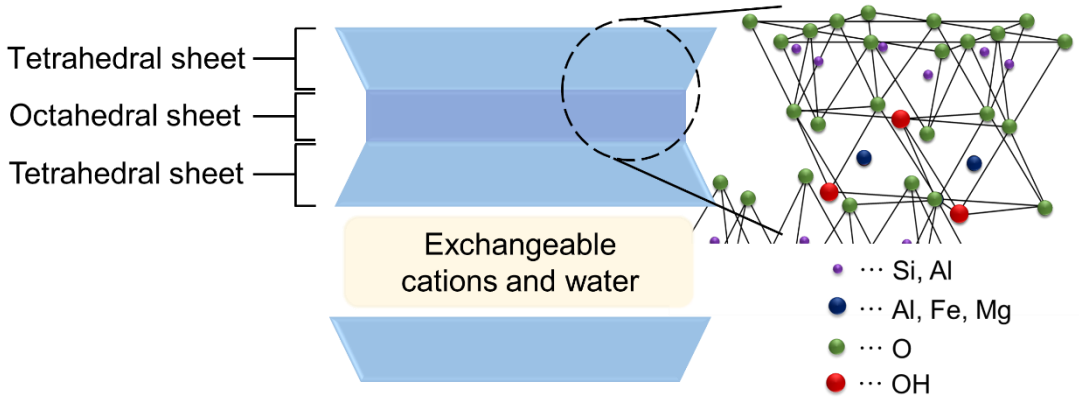

Figure 1-6. Pattern diagram of clay (montmorillonite). Created using the information of reference 80.

Activation such as chemical treatments with acids [e.g., hydrochloric acid (HCl) and sulfuric acid (H_2SO_4)][81] and bases [e.g., sodium hydroxide (NaOH) and potassium hydroxide (KOH)][82] have been performed for a long time to improve the specific surface area and adsorption characteristics of clay. Materials with different structures were formed by selecting activators. When metakaolin, prepared by calcining kaolin in which kaolinite is the major mineral component, is treated with acid (HCl), octahedral Al^{3+} cations are removed, and an amorphous silica phase is formed. In contrast, when treated with a base (KOH), metakaolin dissolves, leading to the formation of K-F zeolite.[83]

1-2-3. Graphitic carbon nitride (g-C_3N_4)

g-C_3N_4, which can be obtained via polymerization by calcining N-rich precursors, such as melamine and urea, possesses a graphite-like layered structure consisting of C and N.[84] g-C_3N_4 has several advantages, including abundant elemental resources, high chemical and thermal

stability, and a band structure suitable for photocatalysis.[85] Therefore, g-C_3N_4 has been applied in different fields, such as photocatalysts,[86,87] sensors,[88] and CO_2 adsorbents.[89,90]

g-C_3N_4 materials are classified into triazine-based g-C_3N_4, heptazine-based g-C_3N_4, melon-based g-C_3N_4, poly(triazine imide), and poly(heptazine imide) (Figure 1-7).[91] Since Kroke et al. reported that heptazine-based g-C_3N_4 is energetically more favorable than triazine-based g-C_3N_4,[92] heptazine-based g-C_3N_4 has been used in schematic diagrams in many studies. However, Irvine et al. revealed that melon-based g-C_3N_4 is the main structure of g-C_3N_4, which was obtained experimentally using XRD and neutron diffraction in 2015.[93] Further, NMR and Fourier-transform infrared spectroscopy (FTIR) have been used to differentiate between triazine-based and heptazine-based g-C_3N_4;[91] the research on synthesis methods that control framework structures of g-C_3N_4 and analysis of products has been conducted.[91] Controlling the morphology of g-C_3N_4 have also been actively conducted to improve the specific surface area and separate charge carriers effectively.[92] So far, various structures such as nanorod,[93] nanofiber,[94] hollow sphere,[95] and nanostructured flower[96] have been synthesized.

The synthesis reaction of g-C_3N_4 and its mechanism have been studied using experimental methods, such as X-ray analysis and differential scanning calorimetry,[97] and calculations including DFT.[98] Samanta and Srivastava et al. reported a synthesis scheme in semi-closed systems under oxygen-lean conditions to synthesize g-C_3N_4 (Scheme 1-1).[99] Moreover, in precursors such as urea, guanidine hydrochloride, and propargyl amine, g-C_3N_4 is constructed via the formation of melamine at lower temperatures (<350 °C), polymeric melem at approximately 400 °C, and carbon nitride network at around 520 °C.[99,100]

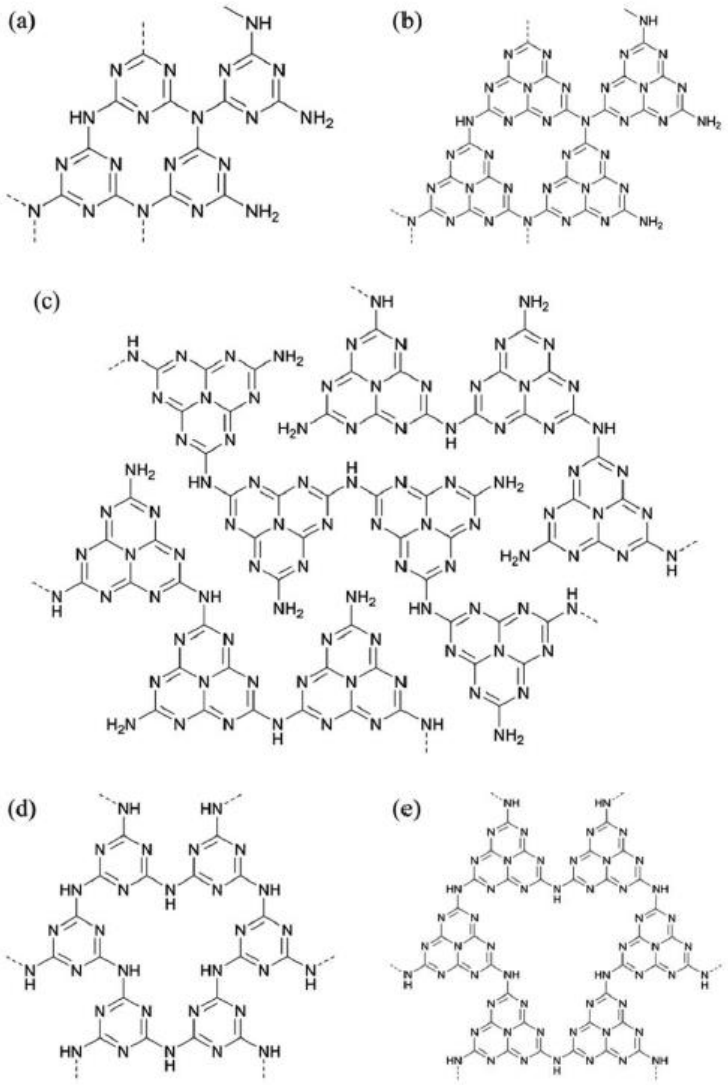

Figure 1-7. Types of g-C_3N_4 and its derivatives: a) triazine-based g-C_3N_4, b) heptazine-based g-C_3N_4, c) melon-based g-C_3N_4, d) poly(triazine imide), and e) poly(heptazine imide). Reproduced with permission from reference 91 (© 2022 The Authors, published by The Royal Society of Chemistry).

Scheme 1-1. Synthesis of g-C_3N_4 via the melem unit using different precursors in semi-closed systems under oxygen-lean conditions to synthesize g-C_3N_4, reproduced with permission from reference 99 (© 2020 The Royal Society of Chemistry).

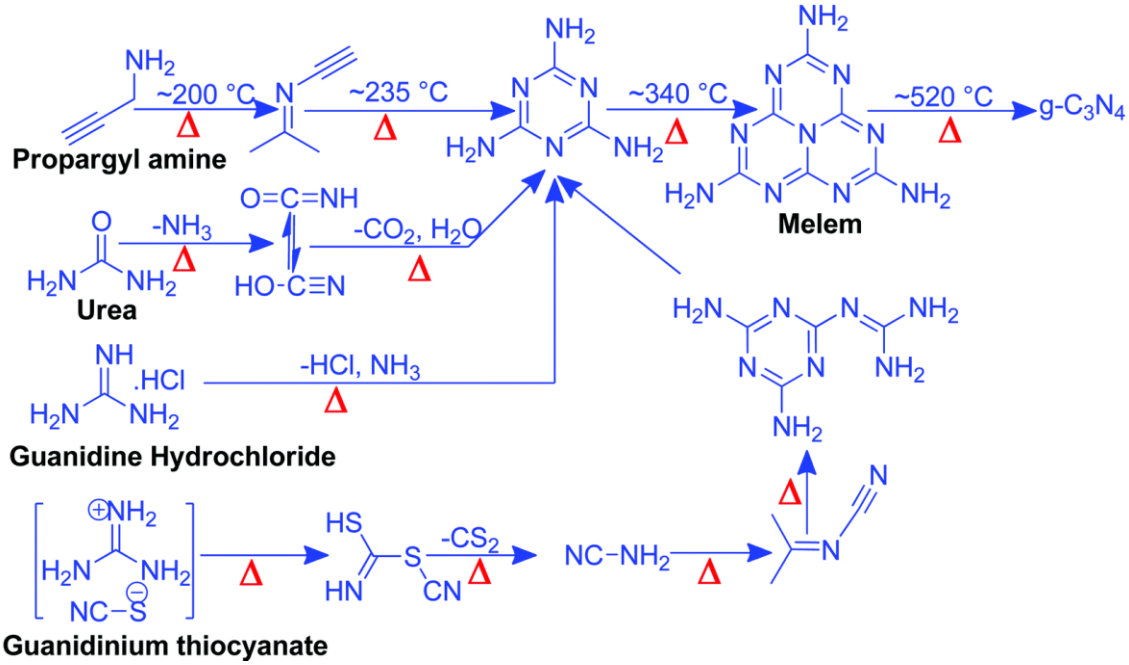

1-3. Templated synthesis

Templated synthesis is a method of constructing a target material in the space surrounding the template and subsequently removing the template to transfer the shape and pore structure derived from the template structure, thus creating a unique and ordered structure (Figure 1-8). Templated synthesis research has been conducted since approximately the 1980s.[101]

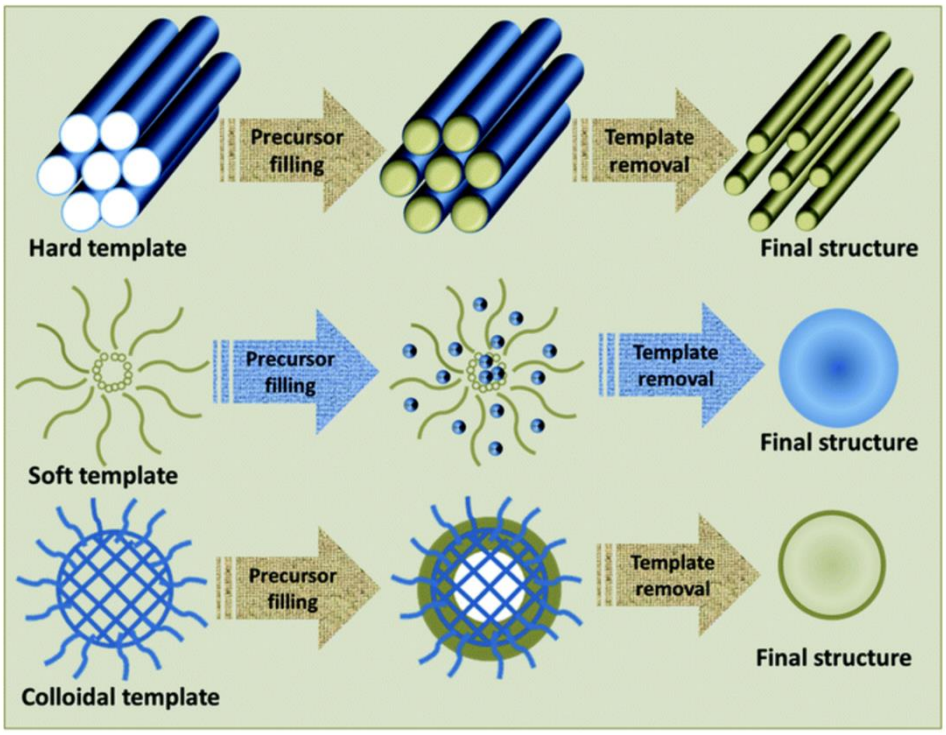

Figure 1-8. Pattern diagram of templated synthesis, reproduced with permission from reference 102 (© 2020 The Royal Society of Chemistry).

Templated synthesis can be categorized into two main types: the soft template method and the hard template method. The soft template method uses surfactant and polymer micelles as templates. Mesoporous silica is a typical example of a nanoporous material in which the pore structure can be controlled using the soft template method. Mesoporous silica is the nanoporous silica consisting of mesopores constructed using the templated synthesis.[103,104] In general, micelles of surfactants and block polymers are used as templates. Mesoporous silica was first obtained using alkyltrimethylammonium chloride and layered polysilicate kanemite; the mesoporous silica had a pore size of 2–4 nm and a high specific surface area of approximately 900 m^2 g^{-1}.[105] However, its mesoporous silica did not have such a high degree of regularity in the pore structure. Subsequently, MCM-41 was developed with uniform pore structures, in which the size can be tuned from 1.6 nm to 10 nm or more with the selection of surfactants using a liquid crystal template mechanism.[106] Tuning the precursor of silica, type of templates (surfactants), and the conditions of the synthesis solution, such as solvent and pH, can produce various types of

mesoporous silicas, including SBA-15,[107] Hiroshima Mesoporous Material-33 (HMM-33),[108] and Technische Universiteit Delft-1 (TUD-1).[109] Furthermore, silica morphology can be controlled with various processes and templates into diverse forms, such as spherical,[110,111] microcapsule,[112] film,[113] fibrous structure,[114] and nanosheet,[115,116] which can enhance the performance of drug delivery, adsorbents, and catalysts.

Conversely, the hard template method is frequently used to synthesize carbon materials. Noncarbon-based materials, including zeolite, mesoporous silica, and metal oxide particles, are used as templates in synthesizing carbon materials. Zeolite-templated carbon,[117–119] which features ordered micropore structure, high surface area, and single-layer graphene framework, and mesoporous carbon,[120–122] with mesopores, can be constructed by forming carbon around the templates, such as zeolite, silica particles, and mesoporous silica, and subsequently treating with acids to remove templates.

Furthermore, studies have been conducted on the use of MOFs as sacrificial templates for metals, metal oxides, porous carbon, and multicomponent composites.[123–125] Various materials, such as surfactants,[126–128] a polycarbonate membrane,[129] porous anodic alumina films,[130] carbon nanotubes,[131] carbon spheres,[132] ice,[133] and solvent phases,[134] have been used as structure-directing agents and templates to synthesize diverse nanostructured materials.

In addition to zero-, one-, and three-dimensional materials, two-dimensional materials and nanospaces have been actively investigated as templates for various materials. The synthesis of silica,[135–137] silicon,[138] metal,[139] metal oxide [even in cupric oxide (CuO)],[140–144] TMD,[145] zeolite,[146] boron nitride,[147] and carbon[148] nanosheets with controlled nanosheet size and thickness, unique structure, and superior porosity has been proposed using graphene, GO, and g-C_3N_4 as templates (Figure 1-9a). In addition, the construction of zeolites with nanopores resulting from the removal of polymer-functionalized GO has been reported (Figure 1-9b).[149] The construction of ultrathin amorphous metal oxide nanosheets has also been demonstrated using a lamellar Cu_2O–oleate complex as a two-dimensional confined template.[150] Nanosheets consisting of polymers, such as vinyl polymers and polyelectrolytes, have also been synthesized using two-dimensional nanospaces of the MOF as reaction templates.[151,152]

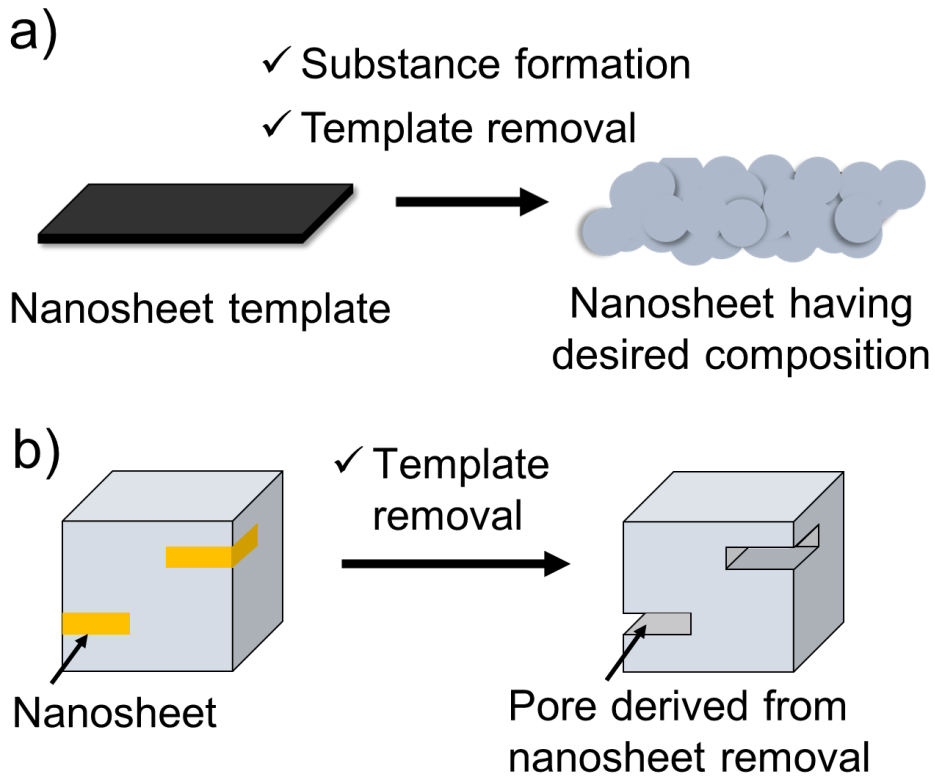

Figure 1-9. a) Synthesis of nanosheets using two-dimensional materials as templates and b) porosity improvement of materials using nanosheets as the pore sources (created using the information of reference 149).

In addition to the synthesis of porous (nanoporous) materials and nanosheets, templated synthesis has also been used to fabricate various materials (e.g., precise structural control of metal nanoparticles and clusters). Studies have focused on the structure control of synthesized nanoparticles, metal clusters, and multimetallic subnanoclusters in which numerous metal elements (2–30 atoms) are alloyed with no phase-segregated state at the atomic level, using dendrimers—polymer materials characterized by a nearly spherical shape, a three-dimensionally crowded exterior, and somewhat hollow interior.[153–157] In addition, other macromolecules (e.g., co-poly-*N,N*-dimethylacrylamide/methacrylic acid/*N,N'*-methylenebisacrylamide[158] and hyperbranched polyethyleneimine[159]) have also been studied.

1-4. Objective and scope of this thesis

As described above, substance formation on two-dimensional materials (e.g., nanosheets) enables the creation of materials with unique structures and high-performance features, such as sheet shapes and high porosity. Studies have been conducted on substance formation on two-dimensional materials across all gas, liquid, and solid phase processes. In terms of the gas phase process, Ye et al. (2021) reported the synthesis of nanosized ultrathin molybdenum disulfide (MoS_2) on montmorillonite nanosheets using the CVD method.[160] Furthermore, substance formation has been carried out for the liquid phase process using different methods, such as the sol–gel method[135,138] and the solvothermal (hydrothermal) method.[141,145] The diffusivity of substances in the gas and liquid phases is higher than that in the solid phase;[161] therefore, collisions and reactions among reactants are easier to occur. The solid-phase process may reduce precursor movement in the reaction system and suppress reactant aggregation. It does not require separation and washing processes when no impurities are generated. Substance formation on two-dimensional materials using a calcination process in the solid phase has been investigated, including the preparation of graphite film, graphene sheet, N-doped graphene-like carbon materials using clay,[162–164] the construction of two-dimensional ordered mesoporous carbon thin layers within the interlayer spaces of MXenes,[165] and the formation of metal oxides on clay.[166] Recently, $NiCo_2O_4$ nanosheets were constructed with the calcination of MOF-modified GO.[167] Even during the author's doctoral program, relevant studies have been conducted on the synthesis of CuO nanosheets by calcining Cu^{2+}-modified GO.[168] However, studies about substance formation on two-dimensional materials using calcination have not explored the underdeveloped areas, such as several unformed substances and the combinations of templates (e.g., nanosheets and polymers) and substances to be formed. The development of this research area can enable the synthesis of nanosheets and nanoporous materials with the desired composition and excellent structures, such as unique morphology (e.g., ultrathin thickness) and textural properties (e.g., high specific surface area).

This dissertation summarizes the achievements of developing and controlling the pore and surface structure of nanoporous materials using substance formation on two-dimensional

materials via calcination. Three types of two-dimensional materials were used: carbon (GO), oxide (clay), and polymer (carbon nitride). Each two-dimensional material possesses unique characteristics. GO exhibits modification properties due to its abundant oxygen functional groups and can be removed by calcination under an air atmosphere. Clay has high chemical and thermal stability. In addition, carbon nitride features bottom-up synthesis. Leveraging the unique characteristics of each two-dimensional material, the author designed a nanoporous material characterized by an excellent structure, such as high porosity and controlled structures. This study was divided into two approaches: the synthesis of nanosheets and the modification of substances on nanosheets (Figure 1-10). In addition, the formation process of the phenomena and material formation mechanisms induced on two-dimensional materials were examined by investigating comparative conditions, preparing comparative samples, and using various measurement techniques.

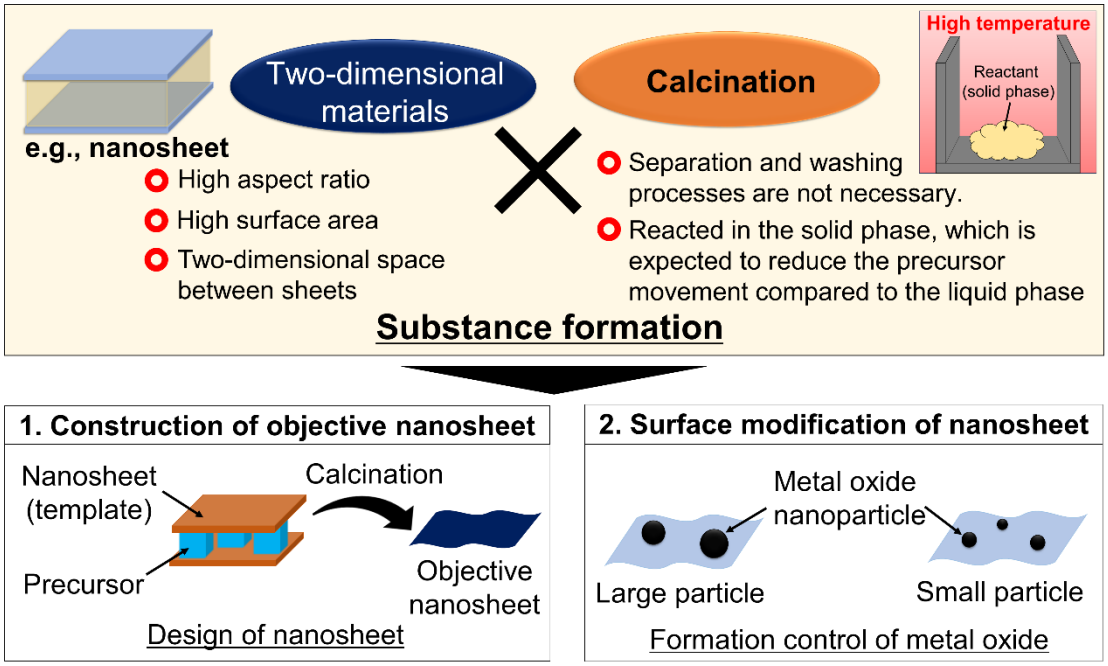

Figure 1-10. Research policy in this thesis.

In Chapter 2, GO was used as a template to control silica formation. Silica nanosheets were synthesized by modifying a silica monomer on the GO surface and then calcining to

simultaneously induce the *in situ* formation of silica on the GO surface and the removal of the template GO.

A polymer template was used in Chapter 3 to control the formation of CuO_x on clay. After the cationic polymer–Cu^{2+} complex was introduced into the clay, the formation of CuO_x and the removal of the polymer templates were induced by calcination to develop CuO_x/clay nanocomposites.

Furthermore, carbon nitride was used as a structural directing agent in Chapter 4 to control the formation of CuO and SiO_2 simultaneously. By calcining a mixture of carbon nitride, CuO sources, and SiO_2 precursors, the formation of CuO and SiO_2 and the removal of carbon nitride by Cu species were induced, and nanoporous CuO–SiO_2 nanocomposites were synthesized.

Some content in this chapter has been adapted with permission from the following papers:

a) Takeuchi, Y.; Obata, S.; Ohkura, K.; Nishina, Y. In Situ Synthesis of Ultrathin Amorphous Silica Nanosheet with Large Specific Surface Area on Graphene Oxide. *ACS Materials Lett.* **2022**, *4*, 2590–2596. (© 2022 American Chemical Society)

https://doi.org/10.1021/acsmaterialslett.2c00805

A direct link to the Published Work: https://pubs.acs.org/articlesonrequest/AOR-MRFPEHMAAXFPKAPVPJS4?_gl=1*a344dq*_ga*MTAzNjE4MTAyNS4xNzE3MzQ2Njg5*_ga_XP5JV6H8Q6*MTczMzA1NDU4Ni4xOS4wLjE3MzMwNTQ1ODYuNjAuMC4w

b) Takeuchi, Y.; Toyoda, Y.; Gotoh, K.; Ohkubo, T. Structure-Directing Synthesis of Porous CuO–SiO_2 Nanocomposites Using Carbon Nitride. *CrystEngComm* **2024**, *26*, 3044-3053. (© 2024 The Royal Society of Chemistry)

https://doi.org/10.1039/D4CE00183D

1-5. References

(1) Chen, L.; Msigwa, G.; Yang, M.; Osman, A. I.; Fawzy, S.; Rooney, D. W.; Yap, P.-S. Strategies to Achieve a Carbon Neutral Society: A Review. *Environ. Chem. Lett.* **2022**, *20*, 2277–2310.

(2) Yu, K. M. K.; Curcic, I.; Gabriel, J.; Tsang, S. C. E. Recent Advances in CO_2 Capture and Utilization. *ChemSusChem* **2008**, *1*, 893–899.

(3) Rosenboom, J.-G.; Langer, R.; Traverso, G. Bioplastics for a Circular Economy. *Nat. Rev. Mater.* **2022**, *7*, 117–137.

(4) Wang, S.; Lu, A.; Zhong, C.-J. Hydrogen Production from Water Electrolysis: Role of Catalysts. *Nano Converg.* **2021**, *8*, 4.

(5) Parlett, C. M. A.; Wilson, K.; Lee, A. F. Hierarchical Porous Materials: Catalytic Applications. *Chem. Soc. Rev.* **2013**, *42*, 3876–3893.

(6) Vu, A.; Qian, Y.; Stein, A. Porous Electrode Materials for Lithium-Ion Batteries – How to Prepare Them and What Makes Them Special. *Adv. Energy Mater.* **2012**, *2*, 1056–1085.

(7) Caro, J.; Noack, M.; Kölsch, P.; Schäfer, R. Zeolite Membranes – State of Their Development and Perspective. *Microporous Mesoporous Mater.* **2000**, *38*, 3–24.

(8) Siegelman, R. L.; Kim, E. J.; Long, J. R. Porous Materials for Carbon Dioxide Separations. *Nat. Mater.* **2021**, *20*, 1060–1072.

(9) Ozin, G. A.; Kuperman, A.; Stein, A. Advanced Zeolite, Materials Science. *Angew. Chem. Int. Ed.* **1989,** *28*, 359–376.

(10) Vivo-Vilches, J. F.; Bailón-García, E.; Pérez-Cadenas, A. F.; Carrasco-Marín, F.; Maldonado-Hódar, F. J. Tailoring the Surface Chemistry and Porosity of Activated Carbons: Evidence of Reorganization and Mobility of Oxygenated Surface Groups. *Carbon* **2014**, *68*, 520–530.

(11) Zhou, H.-C. J.; Kitagawa, S. Metal–Organic Frameworks (MOFs). *Chem. Soc. Rev.* **2014**, *43*, 5415–5418.

(12) Zdravkov, B.; Čermák, J.; Šefara, M.; Janků, J. Pore Classification in the Characterization of Porous Materials: A Perspective. *Open Chem.* **2007**, *5*, 385–395.

(13) McEnaney, B. Adsorption and Structure in Microporous Carbons. *Carbon* **1988**, *26*,

267–274.

(14) Hoang, V.-T.; Huang, Q.; Eić, M.; Do, T.-O.; Kaliaguine, S. Structure and Diffusion Characterization of SBA-15 Materials. *Langmuir* **2005**, *21*, 2051–2057.

(15) Zhao, L.; Qin, H.; Wu, R.; Zou, H. Recent Advances of Mesoporous Materials in Sample Preparation. *J. Chromatogr. A* **2012**, *1228*, 193–204.

(16) Gu, H.; Liu, Y.; Yin, D.; Cai, L.; Zhang, B.; Zhang, Q. Heparin-Immobilized Polymeric Monolithic Column with Submicron Skeletons and Well-Defined Macropores for Highly Efficient Purification of Enterovirus 71. *Macromol. Mater. Eng.* **2018**, *303,* 1800411.

(17) Bolton, J.; Bailey, T. S.; Rzayev, J. Large Pore Size Nanoporous Materials from the Self-Assembly of Asymmetric Bottlebrush Block Copolymers. *Nano Lett.* **2011**, *11*, 998–1001.

(18) Song, N.; Kakuta, T.; Yamagishi, T.; Yang, Y.-W.; Ogoshi, T. Molecular-Scale Porous Materials Based on Pillar[n]Arenes. *Chem* **2018**, *4*, 2029–2053.

(19) Fu, Z.; Wang, X.; Gardner, A. M.; Wang, X.; Chong, S. Y.; Neri, G.; Cowan, A. J.; Liu, L.; Li, X.; Vogel, A.; Clowes, R.; Bilton, M.; Chen, L.; Sprick, R. S.; Cooper, A. I. A Stable Covalent Organic Framework for Photocatalytic Carbon Dioxide Reduction. *Chem. Sci.* **2020**, *11*, 543–550.

(20) Wang, C.; Kim, J.; Tang, J.; Kim, M.; Lim, H.; Malgras, V.; You, J.; Xu, Q.; Li, J.; Yamauchi, Y. New Strategies for Novel MOF-Derived Carbon Materials Based on Nanoarchitectures. *Chem* **2020**, *6*, 19–40.

(21) Nishihara, H.; Hirota, T.; Matsuura, K.; Ohwada, M.; Hoshino, N.; Akutagawa, T.; Higuchi, T.; Jinnai, H.; Koseki, Y.; Kasai, H.; Matsuo, Y.; Maruyama, J.; Hayasaka, Y.; Konaka, H.; Yamada, Y.; Yamaguchi, S.; Kamiya, K.; Kamimura, T.; Nobukuni, H.; Tani, F. Synthesis of Ordered Carbonaceous Frameworks from Organic Crystals. *Nat. Commun.* **2017**, *8*, 109.

(22) Sano, Y.; Toyoda, R.; Chida, K.; Yoshii, T.; Nishihara, H.; Nishina, Y.; Asanoma, D.; Takaishi, S.; Sugimoto, K.; Sakamoto, R. Ordered Carbonaceous Framework Synthesized from Hexaazatrinaphthylene with Enediyne Groups via Solid-State Bergman Cyclization Reaction. *ACS Appl. Mater. Interfaces* **2024**, *16*, 42615–42622.

(23) Mallette, A. J.; Espindola, G.; Varghese, N.; Rimer, J. D. Highly Efficient Synthesis of Zeolite Chabazite Using Cooperative Hydration-Mismatched Inorganic Structure-Directing Agents. *Chem. Sci.* **2024**, *15*, 573–583.

(24) Rabani, I.; Lee, J.-W.; Lim, T.; Truong, H. B.; Nisar, S.; Afzal, S.; Seo, Y.-S. Construction of a Uniform Zeolitic Imidazole Framework (ZIF-8) Nanocrystal through a Wet Chemical Route towards Supercapacitor Application. *RSC Adv.* **2024**, *14*, 118–130.

(25) Schlumberger, C.; Thommes, M. Characterization of Hierarchically Ordered Porous Materials by Physisorption and Mercury Porosimetry—A Tutorial Review. *Adv. Mater. Interfaces* **2021**, *8*, 2002181.

(26) Thommes, M.; Kaneko, K.; Neimark, A. V.; Olivier, J. P.; Rodriguez-Reinoso, F.; Rouquerol, J.; Sing, K. S. W. Physisorption of Gases, with Special Reference to the Evaluation of Surface Area and Pore Size Distribution (IUPAC Technical Report). *Pure Appl. Chem.* **2015**, *87*, 1051–1069.

(27) Liu, S.; Sun, H.; Zhang, D.; Yang, K.; Wang, D.; Li, X.; Long, K.; Li, Y. Nuclear Magnetic Resonance Study on the Influence of Liquid Nitrogen Cold Soaking on the Pore Structure of Different Coals. *Phys. Fluids* **2023**, *35*, 012009.

(28) Mikhail, R. S.; Brunauer, S.; Bodor, E. E. Investigations of a Complete Pore Structure Analysis: I. Analysis of micropores. *J. Colloid Interface Sci.* **1968**, *26*, 45–53.

(29) Horvath, G.; Kawazoe, K. Method for the Calculation of Effective Pore Size Distribution in Molecular Sieve Carbon. *J. Chem. Eng. Jpn.* **1983**, *16*, 470–475.

(30) Saito, A.; Foley, H. C. Curvature and Parametric Sensitivity in Models for Adsorption in Micropores. *AIChE J.* **1991**, *37*, 429–436.

(31) Cheng, L. S.; Ralph T, Y. Improved Horvath—Kawazoe Equations Including Spherical Pore Models for Calculating Micropore Size Distribution. *Chem. Eng. Sci.* **1994**, *49*, 2599–2609.

(32) Landers, J.; Gor, G. Y.; Neimark, A. V. Density Functional Theory Methods for Characterization of Porous Materials. *Colloids Surf. A Physicochem. Eng. Asp.* **2013**, *437*, 3–32.

(33) Suzuki, T.; Kaneko, K.; Setoyama, N.; Maddox, M.; Gubbins, K. Grand Canonical Monte Carlo Simulation for Nitrogen Adsorption in Graphitic Slit Micropores: Effect of Interlayer Distance. *Carbon* **1996**, *34*, 909–912.

(34) Takei, T.; Chikazawa, M.; Kanazawa, T. Validity of the Kelvin Equation in Estimation of Small Pore Size by Nitrogen Adsorption. *Colloid Polym. Sci.* **1997,** *275*, 1156–1161.

(35) Barrett, E. P.; Joyner, L. G.; Halenda, P. P. The Determination of Pore Volume and Area Distributions in Porous Substances. I. Computations from Nitrogen Isotherms. *J. Am. Chem. Soc.* **1951**, *73*, 373–380.

(36) Dollimore, D.; Heal, G. R. An Improved Method for the Calculation of Pore Size Distribution from Adsorption Data. *J. Appl. Chem.* **1964**, *14*, 109–114.

(37) Cranston, R. W.; Inkley, F. A. 17 The Determination of Pore Structures from Nitrogen Adsorption Isotherms. *Adv. Catal.* **1957**, *9*, 143–154.

(38) Aurbach, D.; Markovsky, B.; Weissman, I.; Levi, E.; Ein-Eli, Y. On the Correlation between Surface Chemistry and Performance of Graphite Negative Electrodes for Li Ion Batteries. *Electrochim. Acta* **1999**, *45*, 67–86.

(39) Bostick, B. C.; Vairavamurthy, M. A.; Karthikeyan, K. G.; Chorover, J. Cesium Adsorption on Clay Minerals: An EXAFS Spectroscopic Investigation. *Environ. Sci. Technol.* **2002**, *36*, 2670–2676.

(40) Novoselov, K. S.; Geim, A. K.; Morozov, S. V.; Jiang, D.; Zhang, Y.; Dubonos, S. V.; Grigorieva, I. V.; Firsov, A. A. Electric Field Effect in Atomically Thin Carbon Films. *Science* **2004**, *306*, 666–669.

(41) Wang, Q.; O'Hare, D. Recent Advances in the Synthesis and Application of Layered Double Hydroxide (LDH) Nanosheets. *Chem. Rev.* **2012**, *112*, 4124–4155.

(42) Manzeli, S.; Ovchinnikov, D.; Pasquier, D.; Yazyev, O. V.; Kis, A. 2D Transition Metal Dichalcogenides. *Nat. Rev. Mater.* **2017**, *2*, 17033.

(43) Coleman, J. N.; Lotya, M.; O'Neill, A.; Bergin, S. D.; King, P. J.; Khan, U.; Young, K.; Gaucher, A.; De, S.; Smith, R. J.; Shvets, I. V.; Arora, S. K.; Stanton, G.; Kim, H.-Y.; Lee, K.; Kim, G. T.; Duesberg, G. S.; Hallam, T.; Boland, J. J.; Wang, J. J.; Donegan, J. F.; Grunlan, J.

C.; Moriarty, G.; Shmeliov, A.; Nicholls, R. J.; Perkins, J. M.; Grieveson, E. M.; Theuwissen, K.; McComb, D. W.; Nellist, P. D.; Nicolosi, V. Two-Dimensional Nanosheets Produced by Liquid Exfoliation of Layered Materials. *Science* **2011**, *331*, 568–571.

(44) Li, F.-L.; Wang, P.; Huang, X.; Young, D. J.; Wang, H.-F.; Braunstein, P.; Lang, J.-P. Large-Scale, Bottom-Up Synthesis of Binary Metal–Organic Framework Nanosheets for Efficient Water Oxidation. *Angew. Chem*. **2019**, *131*, 7125–7130.

(45) Kumar, P.; Jasra, R. V.; Bhat, T. S. G. Evolution of Porosity and Surface Acidity in Montmorillonite Clay on Acid Activation. *Ind. Eng. Chem. Res.* **1995**, *34*, 1440–1448.

(46) Dong, F.; Li, Y.; Wang, Z.; Ho, W.-K. Enhanced Visible Light Photocatalytic Activity and Oxidation Ability of Porous Graphene-like g-C_3N_4 Nanosheets via Thermal Exfoliation. *Appl. Surf. Sci.* **2015**, *358*, 393–403.

(47) Gil, A.; Gandía, L. M.; Vicente, M. A. Recent Advances in the Synthesis and Catalytic Applications of Pillared Clays. *Catal. Rev.: Sci. Eng.* **2000**, *42*, 145–212.

(48) Matsuo, Y.; Sakai, Y.; Fukutsuka, T.; Sugie, Y. Preparation and Characterization of Pillared Carbons Obtained by Pyrolysis of Silylated Graphite Oxides. *Carbon* **2009**, *47*, 804–811.

(49) Kim, J.-E.; Oh, J.-H.; Kotal, M.; Koratkar, N.; Oh, I.-K. Self-Assembly and Morphological Control of Three-Dimensional Macroporous Architectures Built of Two-Dimensional Materials. *Nano Today* **2017**, *14*, 100–123.

(50) Li, X.; Cai, W.; An, J.; Kim, S.; Nah, J.; Yang, D.; Piner, R.; Velamakanni, A.; Jung, I.; Tutuc, E.; Banerjee, S. K.; Colombo, L.; Ruoff, R. S. Large-Area Synthesis of High-Quality and Uniform Graphene Films on Copper Foils. *Science* **2009**, *324*, 1312–1314.

(51) Zhu, Y.; Murali, S.; Cai, W.; Li, X.; Suk, J. W.; Potts, J. R.; Ruoff, R. S. Graphene and Graphene Oxide: Synthesis, Properties, and Applications. *Adv. Mater.* **2010**, *22*, 3906–3924.

(52) Hummers, W. S.; Offeman, R. E. Preparation of Graphitic Oxide. *J. Am. Chem. Soc.* **1958**, *80*, 1339.

(53) Brodie, B. C. Sur le Poids Atomique du Graphite. *Ann. Chim. Phys.* **1860**, *59*, 466−472.

(54) Botas, C.; Álvarez, P.; Blanco, P.; Granda, M.; Blanco, C.; Santamaría, R.; Romasanta,

L. J.; Verdejo, R.; López-Manchado, M. A.; Menéndez, R. Graphene Materials with Different Structures Prepared from the Same Graphite by the Hummers and Brodie Methods. *Carbon* **2013**, *65*, 156–164.

(55) Chen, D.; Feng, H.; Li, J. Graphene Oxide: Preparation, Functionalization, and Electrochemical Applications. *Chem. Rev.* **2012**, *112*, 6027–6053.

(56) Boulanger, N.; Kuzenkova, A. S.; Iakunkov, A.; Nordenström, A.; Romanchuk, A. Y.; Trigub, A. L.; Zasimov, P. V.; Prodana, M.; Enachescu, M.; Bauters, S.; Amidani, L.; Kvashnina, K. O.; Kalmykov, S. N.; Talyzin, A. V. High Surface Area "3D Graphene Oxide" for Enhanced Sorption of Radionuclides. *Adv. Mater. Interfaces* **2022**, *9*, 2200510.

(57) Thomou, E.; Diamanti, E. K.; Enotiadis, A.; Spyrou, K.; Mitsari, E.; Boutsika, L. G.; Sapalidis, A.; Moretón Alfonsín, E.; De Luca, O.; Gournis, D.; Rudolf, P. New Porous Heterostructures Based on Organo-Modified Graphene Oxide for CO_2 Capture. *Front. Chem.* **2020**, *8*, 564838.

(58) Gao, C.; Dong, Z.; Hao, X.; Yao, Y.; Guo, S. Preparation of Reduced Graphene Oxide Aerogel and Its Adsorption for Pb(II). *ACS Omega* **2020**, *5*, 9903–9911.

(59) Xu, Y.; Sheng, K.; Li, C.; Shi, G. Self-Assembled Graphene Hydrogel via a One-Step Hydrothermal Process. *ACS Nano* **2010**, *4*, 4324–4330.

(60) Liu, F.; Chung, S.; Oh, G.; Seo, T. S. Three-Dimensional Graphene Oxide Nanostructure for Fast and Efficient Water-Soluble Dye Removal. *ACS Appl. Mater. Interfaces* **2012**, *4*, 922–927.

(61) Li, Y.; Gao, W.; Ci, L.; Wang, C.; Ajayan, P. M. Catalytic Performance of Pt Nanoparticles on Reduced Graphene Oxide for Methanol Electro-Oxidation. *Carbon* **2010**, *48*, 1124–1130.

(62) Lightcap, I. V.; Kosel, T. H.; Kamat, P. V. Anchoring Semiconductor and Metal Nanoparticles on a Two-Dimensional Catalyst Mat. Storing and Shuttling Electrons with Reduced Graphene Oxide. *Nano Lett.* **2010,** *10*, 577–583.

(63) Cho, S.; Lee, J. S.; Jang, J. Poly(vinylidene fluoride)/NH_2-Treated Graphene Nanodot/Reduced Graphene Oxide Nanocomposites with Enhanced Dielectric Performance

for Ultrahigh Energy Density Capacitor. *ACS Appl. Mater. Interfaces.* **2015**, *7*, 9668–9681.

(64) Lee, K. K.; Deng, S.; Fan, H. M.; Mhaisalkar, S.; Tan, H. R.; Tok, E. S.; Loh, K. P.; Chin, W. S.; Sow, C. H. α-Fe_2O_3 Nanotubes-Reduced Graphene Oxide Composites as Synergistic Electrochemical Capacitor Materials. *Nanoscale* **2012**, *4*, 2958–2961.

(65) Toda, K.; Furue, R.; Hayami, S. Recent Progress in Applications of Graphene Oxide for Gas Sensing: A Review. *Anal. Chim. Acta* **2015**, *878*, 43–53.

(66) Hashemi, S. A.; Bahrani, S.; Mousavi, S. M.; Omidifar, N.; Arjmand, M.; Behbahan, N. G. G.; Ramakrishna, S.; Lankarani, K. B.; Moghadami, M.; Firoozsani, M. Ultrasensitive Biomolecule-Less Nanosensor Based on β-Cyclodextrin/Quinoline Decorated Graphene Oxide toward Prompt and Differentiable Detection of Corona and Influenza Viruses. *Adv. Mater. Technol. 2021*, **6**, 2100341.

(67) Srinivas, G.; Burress, J.; Yildirim, T. Graphene Oxide Derived Carbons (GODCs): Synthesis and Gas Adsorption Properties. *Energy Environ. Sci.* **2012**, *5*, 6453–6459.

(68) Song, Z.; Wang, X.; Zhu, G.; Nian, Q.; Zhou, H.; Yang, D.; Qin, C.; Tang, R. Virus Capture and Destruction by Label-Free Graphene Oxide for Detection and Disinfection Applications. *Small* **2014**, *11*, 1171–1176.

(69) Yu, W.; Sisi, L.; Haiyan, Y.; Jie, L. Progress in the Functional Modification of Graphene/Graphene Oxide: A Review. *RSC Adv.* **2020**, *10*, 15328–15345.

(70) Zhang, T.; Wang, W.; Zhao, Y.; Bai, H.; Wen, T.; Kang, S.; Song, G.; Song, S.; Komarneni, S. Removal of Heavy Metals and Dyes by Clay-Based Adsorbents: From Natural Clays to 1D and 2D Nano-Composites. *Chem. Eng. J.* **2021**, *420*, 127574.

(71) Uddin, M. K. A Review on the Adsorption of Heavy Metals by Clay Minerals, with Special Focus on the Past Decade. *Chem. Eng. J.* **2017**, *308*, 438–462.

(72) Villaluenga, J. P. G.; Khayet, M.; López-Manchado, M. A.; Valentin, J. L.; Seoane, B.; Mengual, J. I. Gas Transport Properties of Polypropylene/Clay Composite Membranes. *Eur. Polym. J.* **2007**, *43*, 1132–1143.

(73) Gu, S.; Kang, X.; Wang, L.; Lichtfouse, E.; Wang, C. Clay Mineral Adsorbents for Heavy Metal Removal from Wastewater: A Review. *Environ. Chem. Lett.* **2019**, *17*, 629–654.

(74) Norrish, K. The Swelling of Montmorillonite. *Discuss. Faraday Soc.* **1954**, 18, 120–134.

(75) Bleam, W. F.; Hoffmann, R. Isomorphous Substitution in Phyllosilicates as an Electronegativity Perturbation: Its Effect on Bonding and Charge Distribution. *Inorg. Chem.* **1988**, *27*, 3180–3186.

(76) Gupta, S. S.; Bhattacharyya, K. G. Adsorption of Heavy Metals on Kaolinite and Montmorillonite: A Review. *Phys. Chem. Chem. Phys.* **2012**, *14*, 6698–6723.

(77) Hu, C.-H.; Xia, M.-S. Adsorption and Antibacterial Effect of Copper-Exchanged Montmorillonite on *Escherichia Coli* K88. *Appl. Clay Sci.* **2006**, *31*, 180–184.

(78) Barrer, R. M.; MacLeod, D. M. Activation of Montmorillonite by Ion Exchange and Sorption Complexes of Tetra-Alkyl Ammonium Montmorillonites. *Trans. Faraday Soc.* **1955**, *51*, 1290–1300.

(79) Goncharuk, V. V.; Puzyrnaya, L. N.; Pshinko, G. N.; Bogolepov, A. A.; Demchenko, V. Y. The Removal of Heavy Metals from Aqueous Solutions by Montmorillonite Modified with Polyethylenimine. *J. Water Chem. and Technol.* **2010**, *32*, 67–72.

(80) Mitchell, J. K.; Soga, K. *Fundamentals of Soil Behavior*, 3rd ed.; John Wiley & Sons: Hoboken, NJ, USA, 2005.

(81) Komadel, P. Acid Activated Clays: Materials in Continuous Demand. *Appl. Clay Sci.* **2016**, *131*, 84–99.

(82) Khalifa, A. Z.; Cizer, Ö.; Pontikes, Y.; Heath, A.; Patureau, P.; Bernal, S. A.; Marsh, A. T. M. Advances in Alkali-Activation of Clay Minerals. *Cem. Concr. Res.* **2020**, *132*, 106050.

(83) Belver, C.; Bañares Muñoz, M. A.; Vicente, M. A. Chemical Activation of a Kaolinite under Acid and Alkaline Conditions. *Chem. Mater.* **2002**, *14*, 2033–2043.

(84) Cao, S.; Low, J.; Yu, J.; Jaroniec, M. Polymeric Photocatalysts Based on Graphitic Carbon Nitride. *Adv. Mater.* **2015**, *27*, 2150–2176.

(85) Zhang, J.-H.; Wei, M.-J.; Wei, Z.-W.; Pan, M.; Su, C.-Y. Ultrathin Graphitic Carbon Nitride Nanosheets for Photocatalytic Hydrogen Evolution. *ACS Appl. Nano Mater.* **2020**, *3*, 1010–1018.

(86) Shiraishi, Y.; Kanazawa, S.; Sugano, Y.; Tsukamoto, D.; Sakamoto, H.; Ichikawa, S.; Hirai, T. Highly Selective Production of Hydrogen Peroxide on Graphitic Carbon Nitride (g-C_3N_4) Photocatalyst Activated by Visible Light. *ACS Catal.* **2014**, *4*, 774–780.

(87) Ong, W.-J.; Tan, L.-L.; Ng, Y. H.; Yong, S.-T.; Chai, S.-P. Graphitic Carbon Nitride (g-C_3N_4)-Based Photocatalysts for Artificial Photosynthesis and Environmental Remediation: Are We a Step Closer To Achieving Sustainability? *Chem. Rev.* **2016,** *116*, 7159–7329.

(88) Zhang, X.-L.; Zheng, C.; Guo, S.-S.; Li, J.; Yang, H.-H.; Chen, G. Turn-On Fluorescence Sensor for Intracellular Imaging of Glutathione Using g-C_3N_4 Nanosheet–MnO_2 Sandwich Nanocomposite. *Anal. Chem.* **2014**, *86*, 3426–3434.

(89) Burrow, J. N.; Ciufo, R. A.; Smith, L. A.; Wang, Y.; Calabro, D. C.; Henkelman, G.; Mullins, C. B. Calcium Poly(Heptazine Imide): A Covalent Heptazine Framework for Selective CO_2 Adsorption. *ACS Nano* **2022**, *16*, 5393–5403.

(90) Talapaneni, S. N.; Singh, G.; Kim, I. Y.; AlBahily, K.; Al-Muhtaseb, A. H.; Karakoti, A. S.; Tavakkoli, E.; Vinu, A. Nanostructured Carbon Nitrides for CO_2 Capture and Conversion. *Adv. Mater.* **2019**, *32*, 1904635.

(91) Yi, Y.; Wang, J.; Niu, Y.; Yu, Y.; Wu, S.; Ding, K. Exploring the Evolution Patterns of Melem from Thermal Synthesis of Melamine to Graphitic Carbon Nitride. *RSC Adv.* **2022**, *12*, 24311–24318.

(92) Wen, J.; Xie, J.; Chen, X.; Li, X. A Review on g-C_3N_4-Based Photocatalysts. *Appl. Surf. Sci.* **2017**, *391*, 72–123.

(93) Bai, X.; Wang, L.; Zong, R.; Zhu, Y. Photocatalytic Activity Enhanced via g-C_3N_4 Nanoplates to Nanorods. *J. Phys. Chem. C* **2013**, *117*, 9952–9961.

(94) Tahir, M.; Cao, C.; Mahmood, N.; Butt, F. K.; Mahmood, A.; Idrees, F.; Hussain, S.; Tanveer, M.; Ali, Z.; Aslam, I. Multifunctional g-C_3N_4 Nanofibers: A Template-Free Fabrication and Enhanced Optical, Electrochemical, and Photocatalyst Properties. *ACS Appl. Mater. Interfaces* **2014**, *6*, 1258–1265.

(95) Zhao, S.; Zhang, Y.; Zhou, Y.; Wang, Y.; Qiu, K.; Zhang, C.; Fang, J.; Sheng, X. Facile One-Step Synthesis of Hollow Mesoporous g-C_3N_4 Spheres with Ultrathin Nanosheets for

Photoredox Water Splitting. *Carbon* **2018**, *126*, 247–256.

(96) Zhu, Y.-P.; Ren, T.-Z.; Yuan, Z.-Y. Mesoporous Phosphorus-Doped g-C_3N_4 Nanostructured Flowers with Superior Photocatalytic Hydrogen Evolution Performance. *ACS Appl. Mater. Interfaces* **2015**, *7*, 16850–16856.

(97) Groenewolt, M.; Antonietti, M. Synthesis of g-C_3N_4 Nanoparticles in Mesoporous Silica Host Matrices. *Adv. Mater.* **2005**, *17*, 1789–1792.

(98) Botari, T.; Huhn, W. P.; Lau, V. W.-h.; Lotsch, B. V.; Blum, V. Thermodynamic Equilibria in Carbon Nitride Photocatalyst Materials and Conditions for the Existence of Graphitic Carbon Nitride g-C_3N_4. *Chem. Mater.* **2017**, *29*, 4445–4453.

(99) Samanta, S.; Srivastava, R. Catalytic Conversion of CO_2 to Chemicals and Fuels: The Collective Thermocatalytic/Photocatalytic/Electrocatalytic Approach with Graphitic Carbon Nitride. *Mater. Adv.* **2020**, *1*, 1506–1545.

(100) Wang, X.; Maeda, K.; Thomas, A.; Takanabe, K.; Xin, G.; Carlsson, J. M.; Domen, K.; Antonietti, M. A Metal-Free Polymeric Photocatalyst for Hydrogen Production from Water under Visible Light. *Nat. Mater.* **2009**, *8*, 76–80.

(101) Malgras, V.; Ji, Q.; Kamachi, Y.; Mori, T.; Shieh, F.-K.; Wu, K. C.-W.; Ariga, K.; Yamauchi, Y. Templated Synthesis for Nanoarchitectured Porous Materials. *Bull. Chem. Soc. Jpn.* **2015**, *88*, 1171–1200.

(102) Poolakkandy, R. R.; Menamparambath, M. M. Soft-Template-Assisted Synthesis: A Promising Approach for the Fabrication of Transition Metal Oxides. *Nanoscale Adv.* **2020**, *2*, 5015–5045.

(103) Trewyn, B. G.; Slowing, I. I.; Giri, S.; Chen, H.-T.; Lin, V. S.-Y. Synthesis and Functionalization of a Mesoporous Silica Nanoparticle Based on the Sol–Gel Process and Applications in Controlled Release. *Acc. Chem. Res.* **2007**, *40*, 846–853.

(104) Olivieri, F.; Castaldo, R.; Cocca, M.; Gentile, G.; Lavorgna, M. Mesoporous Silica Nanoparticles as Carriers of Active Agents for Smart Anticorrosive Organic Coatings: A Critical Review. *Nanoscale* **2021**,*13*, 9091–9111.

(105) Yanagisawa, T.; Shimizu, T.; Kuroda, K.; Kato, C. The Preparation of

Alkyltrimethylammonium–Kanemite Complexes and Their Conversion to Microporous Materials. *Bull. Chem. Soc. Jpn.* **1990**, *63*, 988–992.

(106) Kresge, C. T.; Leonowicz, M. E.; Roth, W. J.; Vartuli, J. C.; Beck, J. S. Ordered Mesoporous Molecular Sieves Synthesized by a Liquid-Crystal Template Mechanism. *Nature* **1992**, *359*, 710–712.

(107) Zhao, D.; Huo, Q.; Feng, J.; Chmelka, B. F.; Stucky, G. D. Nonionic Triblock and Star Diblock Copolymer and Oligomeric Surfactant Syntheses of Highly Ordered, Hydrothermally Stable, Mesoporous Silica Structures. *J. Am. Chem. Soc.* **1998,** *120*, 6024–6036.

(108) Nandiyanto, A. B. D.; Kim, S.-G.; Iskandar, F.; Okuyama, K. Synthesis of Spherical Mesoporous Silica Nanoparticles with Nanometer-Size Controllable Pores and Outer Diameters. *Microporous Mesoporous Mater.* **2009**, *120*, 447–453.

(109) Jansen, J. C.; Shan, Z.; Marchese, L.; Zhou, W.; Puil, N. v. d.; Maschmeyer, T. A New Templating Method for Three-Dimensional Mesopore Networks. *Chem. Commun.* **2001**, 713–714.

(110) Khan, S. A.; Günther, A.; Schmidt, M. A.; Jensen, K. F. Microfluidic Synthesis of Colloidal Silica. *Langmuir* **2004**, *20*, 8604–8611.

(111) Iskandar, F.; Mikrajuddin; Okuyama, K. In Situ Production of Spherical Silica Particles Containing Self-Organized Mesopores. *Nano Lett.* **2001**, *1*, 231–234.

(112) Fujiwara, M.; Shiokawa, K.; Tanaka, Y.; Nakahara, Y. Preparation and Formation Mechanism of Silica Microcapsules (Hollow Sphere) by Water/Oil/Water Interfacial Reaction. *Chem. Mater.* **2004**, *16*, 5420–5426.

(113) Shopsowitz, K. E.; Qi, H.; Hamad, W. Y.; MacLachlan, M. J. Free-Standing Mesoporous Silica Films with Tunable Chiral Nematic Structures. *Nature* **2010**, *468*, 422–425.

(114) Polshettiwar, V.; Cha, D.; Zhang, X.; Basset, J. M. High-Surface-Area Silica Nanospheres (KCC-1) with a Fibrous Morphology. *Angew. Chem. Int. Ed.* **2010**, *49*, 9652–9656.

(115) Lutz, H.; Jaeger, V.; Berger, R.; Bonn, M.; Pfaendtner, J.; Weidner, T. Biomimetic

Growth of Ultrathin Silica Sheets Using Artificial Amphiphilic Peptides. *Adv. Mater. Interfaces* **2015**, *2*, 1500282.

(116) Singh, B.; Polshettiwar, V. Solution-Phase Synthesis of Two-Dimensional Silica Nanosheets Using Soft Templates and Their Applications in CO_2 Capture. *Nanoscale* **2019**, *11*, 5365–5376.

(117) Kyotani, T.; Nagai, T.; Inoue, S.; Tomita, A. Formation of New Type of Porous Carbon by Carbonization in Zeolite Nanochannels. *Chem. Mater.* **1997**, *9*, 609–615.

(118) Nishihara, H.; Yang, Q.-H.; Hou, P.-X.; Unno, M.; Yamauchi, S.; Saito, R.; Paredes, J. I.; Martínez-Alonso, A.; Tascón, J. M. D.; Sato, Y.; Terauchi, M.; Kyotani, T. A Possible Buckybowl-like Structure of Zeolite Templated Carbon. *Carbon* **2009**, *47*, 1220–1230.

(119) Nishihara, H.; Kyotani, T. Zeolite-Templated Carbons – Three-Dimensional Microporous Graphene Frameworks. *Chem. Commun.* **2018**, *54*, 5648–5673.

(120) Han, S.; Hyeon, T. Simple Silica-Particle Template Synthesis of Mesoporous Carbons. *Chem. Commun.* **1999**, 1955–1956.

(121) Kruk, M.; Jaroniec, M.; Ryoo, R.; Joo, S. H. Characterization of Ordered Mesoporous Carbons Synthesized Using MCM-48 Silicas as Templates. *J. Phys. Chem. B* **2000**, *104*, 7960–7968.

(122) Ryoo, R.; Joo, S. H.; Kruk, M.; Jaroniec, M. Ordered Mesoporous Carbons. *Adv. Mater.* **2001**, *13*, 677–681.

(123) Hu, M.-L.; Masoomi, M. Y.; Morsali, A. Template Strategies with MOFs. *Coord. Chem. Rev.* **2019**, *387*, 415–435.

(124) Salunkhe, R. R.; Kaneti, Y. V.; Yamauchi, Y. Metal–Organic Framework-Derived Nanoporous Metal Oxides toward Supercapacitor Applications: Progress and Prospects. *ACS Nano* **2017**, *11*, 5293–5308.

(125) Das, R.; Pachfule, P.; Banerjee, R.; Poddar, P. Metal and Metal Oxide Nanoparticle Synthesis from Metal Organic Frameworks (MOFs): Finding the Border of Metal and Metal Oxides. *Nanoscale* **2012**, *4*, 591–599.

(126) Dong, C.; Xiao, X.; Chen, G.; Guan, H.; Wang, Y. Morphology Control of Porous CuO

by Surfactant Using Combustion Method. *Appl. Surf. Sci.* **2015**, *349*, 844–848.

(127) Gund, G. S.; Dubal, D. P.; Dhawale, D. S.; Shinde, S. S.; Lokhande, C. D. Porous CuO Nanosheet Clusters Prepared by a Surfactant Assisted Hydrothermal Method for High Performance Supercapacitors. *RSC Adv.* **2013**, *3*, 24099–24107.

(128) Antonelli, D. M.; Ying, J. Y. Synthesis of Hexagonally Packed Mesoporous TiO_2 by a Modified Sol–Gel Method. *Angew. Chem. Int. Ed.* **1995**, *34*, 2014–2017.

(129) Li, X.; Wang, Y.; Lei, Y.; Gu, Z. Highly Sensitive H_2S Sensor Based on Template-Synthesized CuO Nanowires. *RSC Adv.* **2012**, *2*, 2302–2307.

(130) Zhu, Y. F.; Zhou, G. H.; Lin, Y. B.; Liu, L. Controllable Synthesis of Well-Aligned CuO Nanotube Arrays Using Porous Alumina Templates. *Cryst. Res. Technol.* **2012**, *47*, 658–662.

(131) Wu, H.-Q.; Wei, X.-W.; Shao, M.-W.; Gu, J.-S.; Qu, M.-Z. Synthesis of Copper Oxide Nanoparticles Using Carbon Nanotubes as Templates. *Chem. Phys. Lett.* **2002**, *364*, 152–156.

(132) Shao, Q.; Wang, X.; Liu, Q.; Wang, L.; Kang, C.; Wang, Q.; Ge, S. Preparation and Photocatalytic Property of Porous CuO Hollow Microspheres via Carbon Sphere Templates. *J. Nanosci. Nanotechnol.* **2011**, *11*, 10271–10277.

(133) Zhang, H.; Cooper, A. I. Aligned Porous Structures by Directional Freezing. *Adv. Mater.* **2007**, *19*, 1529–1533.

(134) Nakanishi, K. Sol–Gel Process of Oxides Accompanied by Phase Separation. *Bull. Chem. Soc. Jpn.* **2006**, *79*, 673–691.

(135) Kou, L.; Gao, C. Making Silicananoparticle-Covered Graphene Oxide Nanohybrids as General Building Blocks for Large-Area Superhydrophilic Coatings. *Nanoscale* **2011**, *3*, 519–528.

(136) Birdsong, B. K.; Hoogendoorn, B. W.; Nilsson, F.; Andersson, R. L.; Capezza, A. J.; Hedenqvist, M. S.; Farris, S.; Guerrero, A.; Olsson, R. T. Large-Scale Synthesis of 2D-Silica (SiO_x) Nanosheets Using Graphene Oxide (GO) as a Template Material. *Nanoscale* **2023**, *15*, 13037–13048.

(137) Shen, Z.; Cai, Q.; Yin, C.; Xia, Q.; Cheng, J.; Li, X.; Wang, Y. Facile Synthesis of Silica Nanosheets with Hierarchical Pore Structure and Their Amine-Functionalized Composite for

Enhanced CO_2 Capture. *Chem. Eng. Sci.* **2020**, *217*, 115528.

(138) Lu, Z.; Zhu, J.; Sim, D.; Zhou, W.; Shi, W.; Hng, H. H.; Yan, Q. Synthesis of Ultrathin Silicon Nanosheets by Using Graphene Oxide as Template. *Chem. Mater.* **2011**, *23*, 5293–5295.

(139) Takenaka, S.; Arita, H.; Sugiyama, K.; Nakatani, K. Preparation of Pt Nanosheets Using Graphene Oxide. *Chem. Lett.* **2018**, *47*, 975–978.

(140) Boston, R.; Bell, A.; Ting, V. P.; Rhead, A. T.; Nakayama, T.; Faul, C. F. J.; Hall, S. R. Graphene Oxide as a Template for a Complex Functional Oxide. *CrystEngComm* **2015**, *17*, 6094–6097.

(141) Takenaka, S.; Uwai, S.; Ida, S.; Matsune, H.; Kishida, M. Bottom-up Synthesis of Titania and Zirconia Nanosheets and Their Composites with Graphene. *Chem. Lett.* **2013**, *42*, 1188–1190.

(142) Luo, Y.; Xu, X.; Zhang, Y.; Chen, C.-Y.; Zhou, L.; Yan, M.; Wei, Q.; Tian, X.; Mai, L. Graphene Oxide Templated Growth and Superior Lithium Storage Performance of Novel Hierarchical $Co_2V_2O_7$ Nanosheets. *ACS Appl. Mater. Interfaces* **2016**, *8*, 2812–2818.

(143) Wu, J.; Huang, X.; Berglund, K.; Lu, X.; Feng, X.; Larsson, R.; Shi, Y. CuO Nanosheets Produced in Graphene Oxide Solution: An Excellent Anti-Wear Additive for Self-Lubricating Polymer Composites. *Compos. Sci. Technol.* **2018**, *162*, 86–92.

(144) Liang, S.; Zhou, Y.; Wu, W.; Zhang, Y.; Cai, Z.; Pan, J. Preparation of Porous CuO Nanosheet-Liked Structure (CuO-NS) Using C_3N_4 Template with Enhanced Visible-Light Photoactivity in Degradation of Chlortetracycline. *J. Photochem. Photobiol. A* **2017**, *346*, 168–176.

(145) Wang, J.; Tang, J.; Guo, T.; Zhang, S.; Xia, W.; Tan, H.; Bando, Y.; Wang, X.; Yamauchi, Y. C_3N_4-Digested 3D Construction of Hierarchical Metallic Phase MoS_2 Nanostructures. *J. Mater. Chem. A* **2019**, *7*, 18388–18396.

(146) Shen, J.; Sun, Q.; Cao, J.; Wang, P.; Jia, W.; Wang, S.; Zhao, P.; Wang, Z. A Lamellar Structure Zeolite LTA for CO_2 Capture. *New J. Chem.* **2022**, *46*, 6720–6728.

(147) Li, S.; Zeng, X.; Chen, H.; Fang, W.; He, X.; Li, W.; Huang, Z. h.; Zhao, L. Porous

Hexagonal Boron Nitride Nanosheets from g-C_3N_4 Templates with a High Specific Surface Area for CO_2 Adsorption. *Ceram. Int.* **2020**, *46*, 27627–27633.

(148) Yu, H.; Shang, L.; Bian, T.; Shi, R.; Waterhouse, G. I. N.; Zhao, Y.; Zhou, C.; Wu, L.-Z.; Tung, C.-H.; Zhang, T. Nitrogen-Doped Porous Carbon Nanosheets Templated from g-C_3N_4 as Metal-Free Electrocatalysts for Efficient Oxygen Reduction Reaction. *Adv. Mater.* **2016**, *28*, 5080–5086.

(149) Dabbawala, A. A.; Tzitzios, V.; Sunny, K.; Polychronopoulou, K.; Basina, G.; Ismail, I.; Pillai, V.; Tharalekshmy, A.; Stephen, S.; Alhassan, S. M. Synthesis of Nanoporous Zeolite-Y and Zeolite-Y/GO Nanocomposite Using Polyelectrolyte Functionalized Graphene Oxide. *Surf. Coat. Technol.* **2018**, *350*, 369–375.

(150) Jia, B.; Yang, J.; Hao, R.; Li, L.; Guo, L. Confined Synthesis of Ultrathin Amorphous Metal-Oxide Nanosheets. *ACS Materials Lett.* **2020**, *2*, 610–615.

(151) Hosono, N.; Mochizuki, S.; Hayashi, Y.; Uemura, T. Unimolecularly Thick Monosheets of Vinyl Polymers Fabricated in Metal–Organic Frameworks. *Nat. Commun.* **2020**, *11*, 3573.

(152) Nishijima, A.; Hayashi, Y.; Mayumi, K.; Hosono, N.; Uemura, T. Fabrication of Polyelectrolyte Sheets of Unimolecular Thickness via MOF-Templated Polymerization. *Macromolecules* **2023**, *56*, 3141–3148.

(153) Zhao, M.; Sun, L.; Crooks, R. M. Preparation of Cu Nanoclusters within Dendrimer Templates. *J. Am. Chem. Soc.* **1998**, *120*, 4877–4878.

(154) Crooks, R. M.; Zhao, M. Dendrimer-Encapsulated Pt Nanoparticles: Synthesis, Characterization, and Applications to Catalysis. *Adv. Mater.* **1999**, *11*, 217–220.

(155) Garcia-Martinez, J. C.; Crooks, R. M. Extraction of Au Nanoparticles Having Narrow Size Distributions from within Dendrimer Templates. *J. Am. Chem. Soc.* **2004**, *126*, 16170–16178.

(156) Imaoka, T.; Yamamoto, K. Wet-Chemical Strategy for Atom-Precise Metal Cluster Catalysts. *Bull. Chem. Soc. Jpn.* **2019**, *92*, 941–948.

(157) Tsukamoto, T.; Kambe, T.; Nakao, A.; Imaoka, T.; Yamamoto, K. Atom-Hybridization for Synthesis of Polymetallic Clusters. *Nat. Commun.* **2018**, *9*, 3873.

(158) Artuso, F.; D'Archivio, A. A.; Lora, S.; Jerabek, K.; Králik, M.; Corain, B. Nanomorphology of Polymer Frameworks and Their Role as Templates for Generating Size-Controlled Metal Nanoclusters. *Chem. Eur. J.* **2003**, *9*, 5292–5296.

(159) Qu, F.; Zhang, Q.; You, J. Recognition and Determination of Multi-Metal Ions Based on Silver Nanoclusters Capped by Polyethyleneimine with Different Molecular Weights. *New J. Chem.* **2015**, *39*, 9293–9298.

(160) Zhang, J.; Liu, T.; Fu, L.; Ye, G. Synthesis of Nanosized Ultrathin MoS_2 on Montmorillonite Nanosheets by CVD Method. *Chem. Phys. Lett.* **2021**, *781*, 138972.

(161) Heitjans, P.; Indris, S.; Wilkening, M. Solid-State Diffusion and NMR. *Diffus. Fundam.* **2005**, *2*, 45.1–45.20.

(162) Kyotani, T.; Sonobe, N.; Tomita, A. Formation of Highly Orientated Graphite from Polyacrylonitrile by Using a Two-Dimensional Space between Montmorillonite Lamellae. *Nature* **1988**, *331*, 331–333.

(163) Xu, C.; Ning, G.; Zhu, X.; Wang, G.; Liu, X.; Gao, J.; Zhang, Q.; Qian, W.; Wei, F. Synthesis of Graphene from Asphaltene Molecules Adsorbed on Vermiculite Layers. *Carbon* **2013**, *62*, 213–221.

(164) Zhu, R.; Chen, Q.; Wang, X.; Wang, S.; Zhu, J.; He, H. Templated Synthesis of Nitrogen-Doped Graphene-like Carbon Materials Using Spent Montmorillonite. *RSC Adv.* **2015**, *5*, 7522–7528.

(165) Wang, J.; Tang, J.; Ding, B.; Malgras, V.; Chang, Z.; Hao, X.; Wang, Y.; Dou, H.; Zhang, X.; Yamauchi, Y. Hierarchical Porous Carbons with Layer-by-Layer Motif Architectures from Confined Soft-Template Self-Assembly in Layered Materials. *Nat. Commun.* **2017**, *8*, 15717.

(166) Sohrabnezhad, S.; Takas, M. E. Synthesis and Characterization of Porous Clay Heterostructure Intercalated with CuO Nanoparticles as a Visible Light-Driven Photocatalyst. *J. Iran. Chem. Soc.* **2019**, *16*, 45–55.

(167) Babulal, S. M.; Chen, S.-M.; Palani, R.; Venkatesh, K.; Haidyrah, A. S.; Ramaraj, S. K.; Yang, C.-C.; Karuppiah, C. Graphene Oxide Template Based Synthesis of $NiCo_2O_4$ Nanosheets for High Performance Non-Enzymatic Glucose Sensor. *Colloids Surf. A*

Physicochem. Eng. Asp. **2021**, *621*, 126600.

(168) Wang, F.; Zhong, H.; Chen, Z.; Wang, D.; Lai, Z.; Deng, Y.; Wang, X. Porous 2D CuO Nanosheets for Efficient Triethylamine Detection at Low Temperature. *Chin. Chem. Lett.* **2023**, *34*, 107392.

Chapter 2. Material synthesis using GO

ABSTRACT: GO has properties such as modification properties using oxygen functional groups and removable with calcination in an air atmosphere. Further, two-dimensional materials, such as GO, were used as the template to fabricate silica nanosheets. In chapter 2, I synthesized materials by utilizing GO properties and inducing substance formation on GO surfaces and template removal with calcination. Previously, silica nanosheets with lamellar structure and unique properties have been synthesized using surfactant and two-dimensional materials (even in GO) as the template. However, silica nanosheets with ultrathin thicknesses below 2 nm and large specific surface areas had not been achieved at the time of the publication of this research. Therefore, I developed the *in situ* synthesis of ultrathin silica nanosheets using GO functionalized with alkoxysilanes having amino groups. The synthesized silica nanosheets were about 1 nm thick and had an amorphous structure and high specific surface areas (e.g., 904 m^2 g^{-1}).

2-1. Synthesis of silica nanosheets using GO

2-1-1. Introduction

Inorganic nanomaterials with beneficial properties, such as heat resistance, wear resistance, and corrosion resistance, have attracted attention because of rapid developments in advanced materials technologies. Silica, commonly known as silicon dioxide (SiO_2), is a typical example of an inorganic material used in a wide range of applications because of its chemical stability, biocompatibility, and tunability of morphology and internal structure. For example, silica materials with a high concentration of pores and a large specific surface area have been applied in catalyst support,[1,2] drug delivery,[3,4] gas separation membranes,[5,6] and separators for batteries.[7]

One widely used preparation method for silica is the sol–gel method.[8,9] In this process, the siloxane network is constructed through a hydrolysis/polycondensation reaction. Because the preparation process is carried out in a liquid at a low temperature, the sol–gel method allows organic template substances to be introduced into the siloxane network, which makes it possible to design organic–inorganic hybrid precursors to fabricate functional silica systems.[10]

So far, surfactants,[11–14] block copolymers,[13] and solvent phases generated by phase separation[15]

have been utilized as templates for fabricating porous (nanoporous) silica. In recent years, two-dimensional materials, such as g-C_3N_4[16,17] and GO,[18,19] have been attracting attention as template materials for functional silica synthesis. Particularly, GO is a two-dimensional nanocarbon obtained by oxidizing and exfoliating graphite, showing high specific surface area, high strength, and modifiable properties using the oxygen functional groups.[20] Previously, silica nanosheets have been prepared by growing SiO_2 on the surface of GO.[18,19] Despite the demand for applications such as gas adsorption and catalyst support, amorphous silica nanosheets with ultrathin thickness (less than 2 nm) and large specific surface area had not been prepared before the publication of this research. Therefore, synthesis of ultrathin 1-nm-thick silica nanosheets with large specific surface areas was conducted utilizing GO and molecular modification.

Several hybrid materials consisting of 3-aminopropyltriethoxysilane (APTES) and GO have been reported.[21–24] However, no studies had reported the synthesis of silica nanosheets using APTES in the GO/APTES hybrid as a silica source and then removing the GO template during silica formation. In the current study, APTES was used as the silica source to create ultrathin layers of silica between GO interlayers. After modifying the GO surfaces with APTES molecules (Scheme 2-1a), the *in situ* synthesis of silica on GO was promoted while the GO template was removed in the calcination process to prepare ultrathin silica nanosheets (SN) (Scheme 2-1b). The precursors and SN were characterized by elemental analysis with SEM-energy dispersive spectroscopy (EDX) and combustion methods, identifying the functional groups and chemical bonds with FTIR, Raman, and X-ray photoelectron spectroscopy (XPS) spectra, observing morphology with SEM and atomic force microscopy (AFM), determining the crystallinity with powder XRD, and measuring the pore structure with N_2 adsorption–desorption tests at each fabrication stage.

Scheme 2-1. Construction of silica nanosheet. a) Preparation of precursor (APTES-GO), and b) synthesis of silica nanosheet (SN).

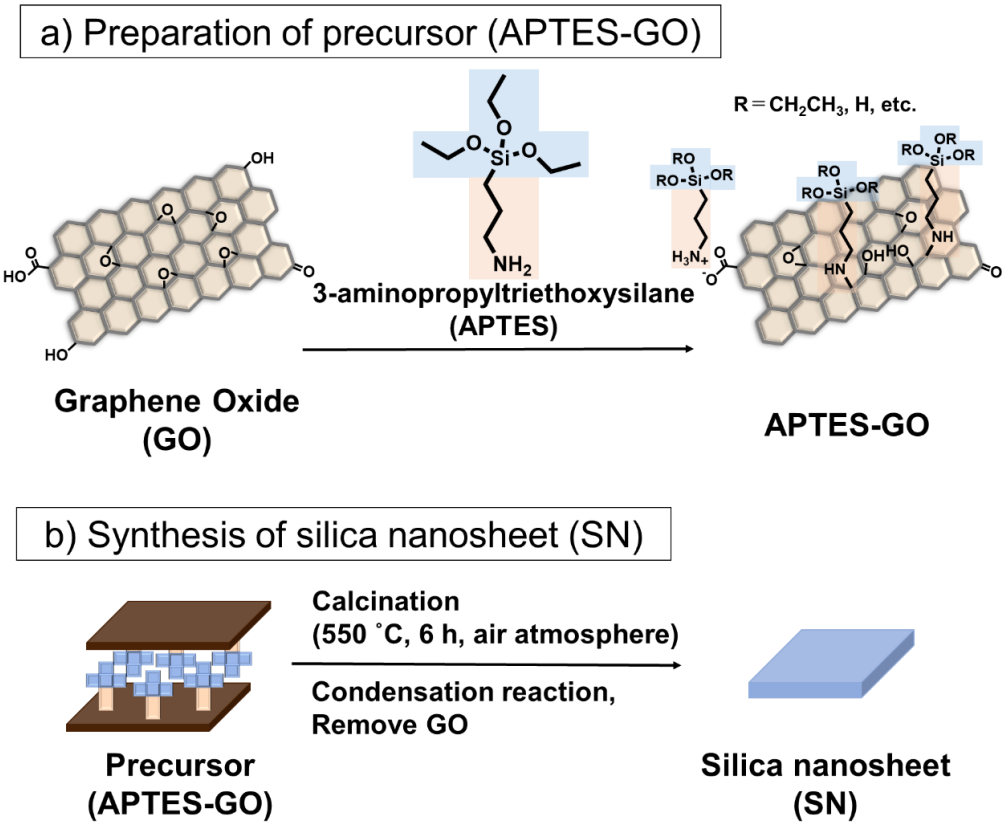

2-1-2. Experimental section

2-1-2-1. Chemicals

Graphite was purchased from Bay Carbon Inc, United States of America. APTES and sodium hydrogen carbonate ($NaHCO_3$) were purchased from Nacalai Tesque, Inc, Japan. Hydrogen peroxide (H_2O_2) was obtained from Kanto Chemical Co., Inc, Japan. Triethoxy(propyl)silane ($^nPrSi(OEt)_3$) was obtained from Tokyo Chemical Industry Co., Ltd, Japan. H_2SO_4, potassium permanganate ($KMnO_4$), ethylene glycol, and ethanol (99.5%) were supplied by FUJIFILM Wako Pure Chemical Corporation, Japan. Solmix (ethanol: 85.5%, n-propyl alcohol: 9.6%, methanol: 4.9%, water: less than 0.2%) was purchased from Japan Alcohol Trading Co., Ltd, Japan. Deionized water was produced with the pure water production machine made by Millipore.

2-1-2-2. Preparation of silica nanosheet precursors

First, GO, which is a template of silica nanosheet, was prepared with the modified Hummers method.[25] 100 g of graphite was added to 2.5 L of concentrated H_2SO_4. 300 g of $KMnO_4$ was added slowly to the solution in the ice bath with stirring so that the temperature of the mixture did not exceed 55 °C. Next, the oxidation reaction of graphite was proceeded by stirring at 35 °C for 2 h. Next, 5 L of water was added slowly so that the temperature of the mixture did not exceed 50 °C, followed by 250 mL of H_2O_2 (30% aqueous solution, 250 mL) added to the mixture. Subsequently, the obtained product was washed with water 10 times by centrifugation, and then freeze-dried to obtain GO as a powder.

In next step, GO was modified with APTES and heating treatment was conducted to construct silica and remove GO. After adding 0.2 g of GO and 1 g of APTES to 100 mL of ethylene glycol, ultrasonic treatment was performed for 60 min to uniformly disperse each compound. After reacting at room temperature for 24 h, centrifuging, washing with alcohol (Solmix) and water to remove APTES which was not introduced to GO, and freeze-drying were performed to obtain APTES-GO, which is the precursor of the silica nanosheet.

To understand the interaction between APTES and GO, a comparative investigation was conducted using $^{n}PrSi(OEt)_3$, which does not have an amino group. In the case of using $^{n}PrSi(OEt)_3$, APTES in the above method was replaced with $^{n}PrSi(OEt)_3$, and $NaHCO_3$ was added to make the solution basic as well as the condition of APTES-GO synthesis. After adding 0.2 g of GO to 100 mL of ethylene glycol, 1 g of $^{n}PrSi(OEt)_3$, and 1 g of $NaHCO_3$ were added to the mixture. Subsequently, sonication was performed for 60 min to disperse each compound uniformly. After reacting at room temperature for 24 h, the product [$^{n}PrSi(OEt)_3$-GO] was obtained by centrifugation, washing with alcohol (Solmix) and water, and freeze-drying.

2-1-2-3. Synthesis of silica nanosheets

The prepared APTES-GO was heated at 550 °C (ramping rate: 5 °C min^{-1}), for 6 h, in an air atmosphere to obtain the silica nanosheets (SN).

2-1-2-4. Scale study of silica nanosheet synthesis

After adding 5 g of APTES and 1 g or 5 g of GO to 500 mL of ethylene glycol, sonication was performed for 60 min to disperse each compound uniformly. After reacting at 25 °C or 40 °C for 24 h, centrifugation, washing with Solmix and water, and freeze-drying were performed. Prepared each APTES-GO was heated at 550 °C (ramping rate: 5 °C min^{-1}), for 6 h, in an air atmosphere to obtain SN at each scale.

2-1-2-5. Characterization

Carbon, hydrogen, nitrogen (CHN) elemental analysis (PerkinElmer 2400II, USA) was performed to measure the elemental proportions of each material. The value is the average of the two measurements. The element ratio (C, O, Si) of the material was determined by SEM (JEOL JSM-IT100LA, Japan) equipped with EDX spectroscopy. The value is the average of the three measurements. Functional groups and chemical species in the material were determined by attenuated total reflection (ATR)-FTIR (SHIMADZU IR Tracer 100, Japan). Diamond was used as a prism. The measurement range was 500–4000 cm^{-1}. The surface chemical states of the materials were determined through XPS (JEOL JPS-9030, Japan). The path energy was set to 10 eV. The measured sample was coated over the Cu substrate. The binding energy of the Cu $2p_{3/2}$ peak at 932.7 eV was used as a reference to calibrate the binding energy scale. Thermogravimetric analysis (TGA) was conducted with thermo gravimetry analyzer (SHIMADZU DTG-60/60H, Japan). After keeping at 80 °C to remove water attached to materials, the temperature was raised from 80 to 800 °C (ramping rate: 10 °C/min), and weight loss was calculated from the result of weight fluctuations. The surface morphology of the sample was observed with SEM (Hitachi SU9000, Japan). The thickness of the sample was measured with AFM (SHIMADZU SPM-9700HT, Japan). The samples of GO and APTES-attached GO for AFM measurements were prepared as follows. The GO solution was coated onto an ozone-treated Si substrate via spin coating. The substrate was immersed in a solution containing 10 mL of ethylene glycol and 100 mg of APTES at room temperature for 24 h. Subsequently, the Si substrate was washed with Solmix and dried under vacuum conditions. The sample is called APTES-attached GO. The

sample of SN for AFM measurement was also prepared with the spin coating method. SN dispersed in ethanol was coated on an ozone-treated Si substrate. Powder XRD was measured by X-ray analyzer (Malvern Panalytical, Netherlands) with Cu Kα rays (λ = 0.154 nm). The tube voltage, the current, the 2θ range, and the scan speed were 40 kV, 15 mA, 5–40°, and 0.0005°/s, respectively. Porosity was evaluated using BELSORP-max II (MicrotracBEL Corp. Japan). Adsorption–desorption test was performed using N_2 as the adsorbate at 77 K to obtain the adsorption–desorption isotherm. The isotherm was analyzed by BET equation to determine the specific surface area (S_{BET}), and the pore volume (V_{total}) was estimated from the amount of adsorbed at relative pressure p/p_0 = 0.99. The pore size distribution of SN was obtained by analyzing the adsorption isotherm with HK method.

2-1-3. Results and discussion

2-1-3-1. Evaluation of silica nanosheet precursors

The GO surfaces were modified using APTES, and the interaction between APTES and GO was investigated by comparative examination using $^{n}PrSi(OEt)_3$, which has no amino groups. Table 2-1 shows the results of the CHN elemental analysis. In pristine GO, C and H were confirmed, but N was not observed. However, in APTES-GO, 3.6 wt% of N derived from APTES was confirmed. The surface density of APTES was 2.4 molecules nm^{-2} (Scheme 2-2, Table 2-2). Further, distance between silanol groups was calculated with two models; i.e., a single-layer model (Figure 2-1a) and double-layer model (Figure 2-1b). In the single-layer model, the distance between silanol groups was 0.5–0.6 nm, which was too far apart to react and on-sheet formation of silica was expected. In contrast, the distance between silanol groups in the double-layer model was 0.1–0.3 nm, where a polycondensation reaction may occur between layers.

Table 2-1. Elemental ratios of each material obtained from CHN elemental analysis.

	GO	APTES-GO
C wt%	47.2	45.2
H wt%	2.3	3.7
N wt%	0.0	3.6

Scheme 2-2. Calculation of modification density.

1. Conversion of elemental ratio from wt% to atom ratio

2. Calculation of carbon ratio derived from GO (C_{GO} [atom ratio]) following equations below, assuming that all alkoxy groups of APTES were hydrolyzed.

APTES-GO: $C_{APTES\text{-}GO}$ [atom ratio] = C [atom ratio] – N [atom ratio]×3

3. Calculation of N/C_{GO} [-], which represents the modification degrees of amines, by dividing N [atom ratio] by each C_{GO} [atom ratio]

4. Calculation of amine-modification density per unit area

(D_{amine} [molecules nm^{-2}])

a) Calculated the amounts of N per 54 carbons (N_{C54})

b) Calculated the surface areas of 19 benzene rings for 54 carbons (1.93 nm^2) with the area on both sides of the benzene ring (0.102 nm^2)

a) D_{amine} was calculated by dividing N_{C54} by 1.93 nm^2.

Table 2-2. Element ratios and calculation result of modification degree (N/C_{GO}) and modification density (D_{amine}).

	APTES-GO
C [wt%]	45.2
H [wt%]	3.7
N [wt%]	3.6
C [atom ratio]	48.9
H [atom ratio]	47.7
N [atom ratio]	3.3
C_{GO} [atom ratio]	39.0
N/C_{GO} [-]	0.085
D_{amine} [molecules nm^{-2}]	2.4

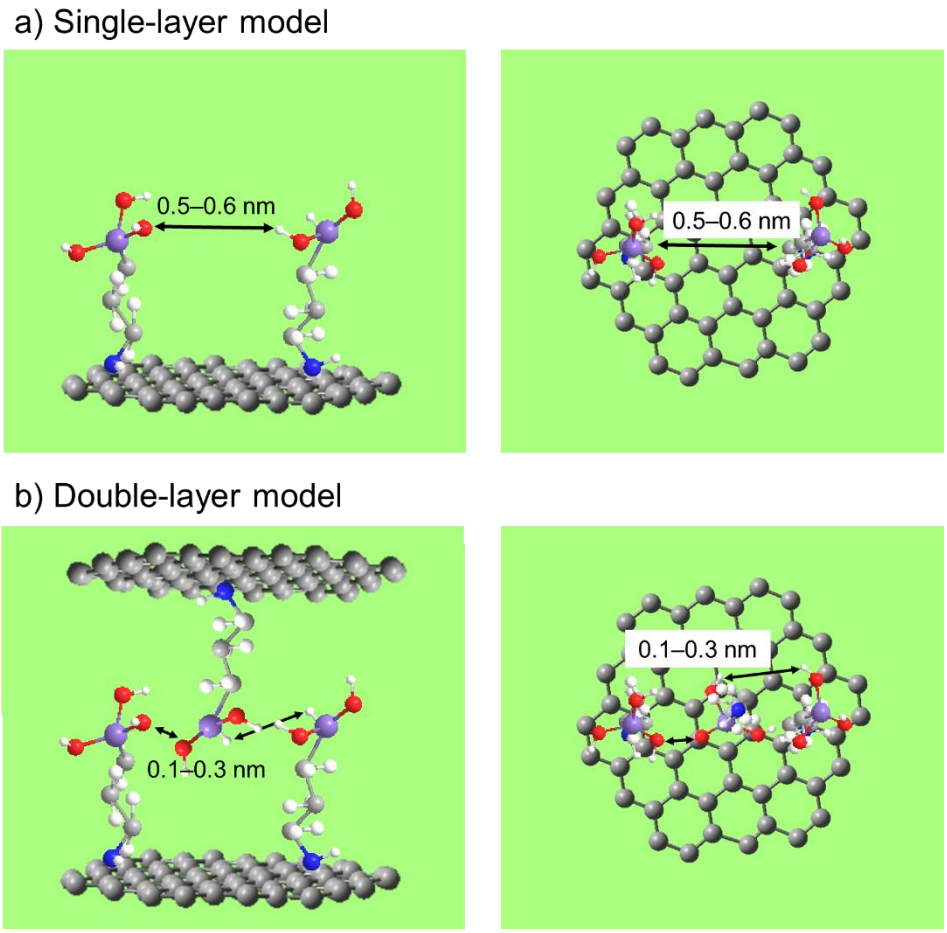

Figure 2-1. Pattern diagrams of APTES-GO; a) single-layer model, b) double-layer model.

Next, how APTES bonded to GO were investigated by comparing it with an NH_2-free silica source, $^{n}PrSi(OEt)_3$. EDX measurements were performed to confirm the elemental ratio of Si in GO, APTES-GO, and $^{n}PrSi(OEt)_3$-GO (Table 2-3). Accordingly, 2.8 at% of Si derived from APTES was confirmed in APTES-GO, whereas $^{n}PrSi(OEt)_3$ did not attach onto GO. Figure 2-2a shows the results of FTIR, measured to confirm the functional groups in each material. In pristine GO, the sp^2 domain (C=C bond, 1620 cm^{-1}), epoxy (C–O–C, 1221 cm^{-1}), hydroxy (O–H, 3194, 1044 cm^{-1}), and carboxy (C=O, 1722 cm^{-1}) groups were confirmed.[26,27] In addition to the above peaks, APTES-GO showed the alkyl-derived C–H stretching (2900–3000 cm^{-1}) peak, amine-derived N–H stretching (3186 cm^{-1}), N–H bending (1522 cm^{-1}), and N–H wagging vibration (687 cm^{-1}) peaks[28] and Si-related bonds such as Si–O–C (1100 cm^{-1}), Si–OH (903 cm^{-1}), and Si–C (746 cm^{-1}).[29–31] These results suggest that an ethoxy group of APTES is partially hydrolyzed and

Si–OH and Si–O–C coexist. In ^{n}PrSi(OEt)$_3$-GO, any peaks related to alkyl, Si–O–C, Si–OH, or Si–C were not observed, indicating that ^{n}PrSi(OEt)$_3$ was not attached to GO. Figure 2-2b shows the high resolution XPS spectrum of APTES-GO in the Si 2p region. The Si–O (Si–OR; R= Et, H, or Si, 102.0 eV) and Si–C (100.5 eV) were confirmed.[32–34] However, the peak derived from SiO_2 (e.g., 103.5, 103.7 eV)[32,35] was not observed, suggesting that SiO_2 (silica) was not formed.

Table 2-3. Elemental ratios obtained by SEM-EDX of GO, APTES-GO, and ^{n}PrSi(OEt)$_3$-GO,

	GO	**APTES-GO**	**^{n}PrSi(OEt)$_3$-GO**
C at%	60.1	63.7	64.7
O at%	39.9	33.4	35.2
Si at%	—	2.8	0.0

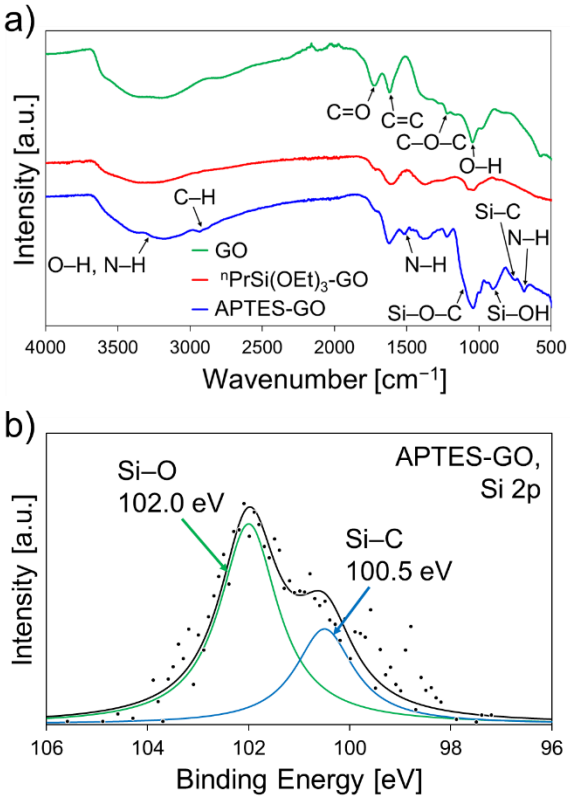

Figure 2-2. a) FTIR spectra of GO, APTES-GO, and ^{n}PrSi(OEt)$_3$-GO and b) high resolution XPS spectrum of APTES-GO at Si 2p region.

The crystalline structure of each material was analyzed by powder XRD (Figure 2-3). In pristine GO, the peak corresponding to the interlayer of GO (001) was confirmed at 2θ = 10.4°, indicating the interlayer distance of 0.85 nm. The XRD pattern of APTES-GO showed the peak at 2θ = 7.1°, and thus, the interlayer distance of APTES-GO increased to 1.2 nm. The increased interlayer distance suggested that APTES was introduced between the GO layers. Moreover, AFM images and height profiles (Figure 2-4) suggested successful GO surface modification. The thickness of the pristine GO was ~1.4 nm and that of APTES-attached GO increased to ~2.1 nm, suggesting that APTES was grafted on the basal plane of GO. Overall, the results suggested that the GO surface was successfully modified with an APTES layer, which provided the precursor for silica in the following experiments.

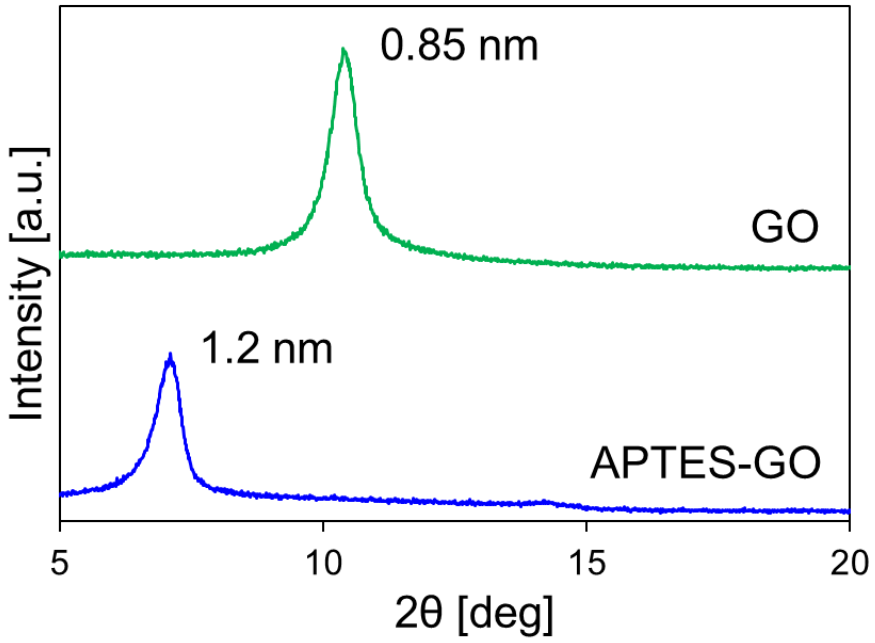

Figure 2-3. XRD patterns and layer distances of GO and APTES-GO.

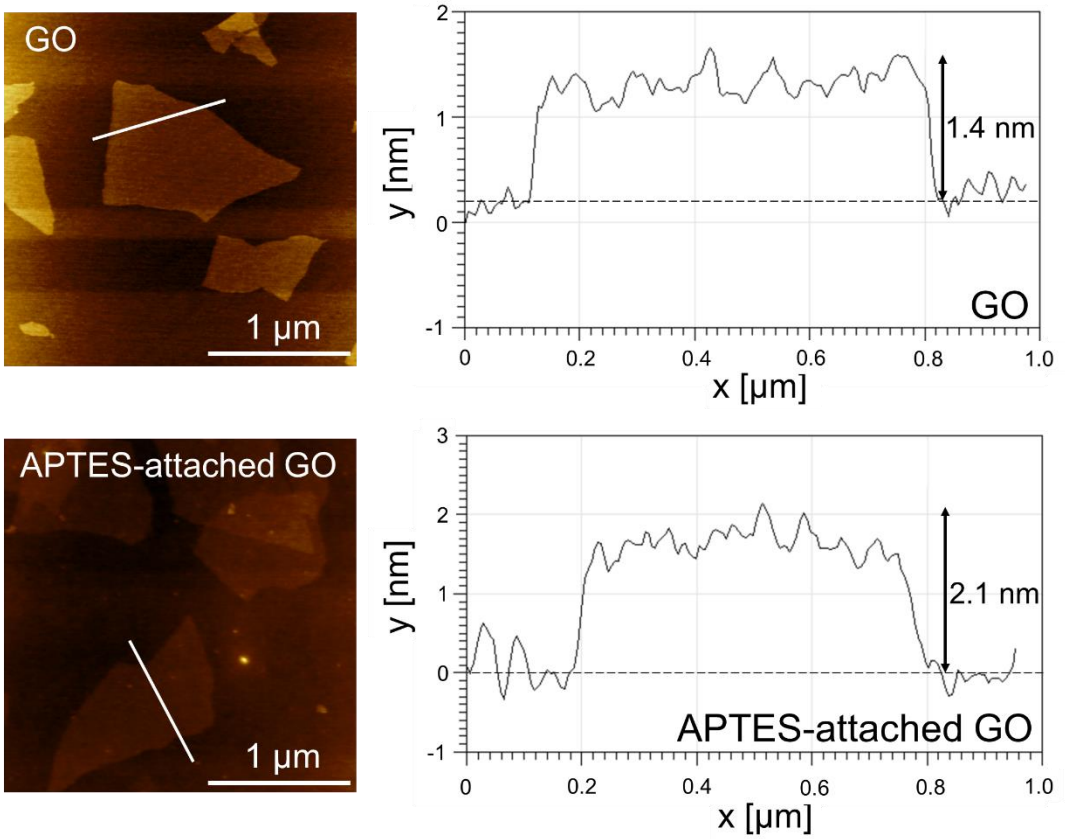

Figure 2-4. AFM images and height profiles of GO and APTES-attached GO.

2-1-3-2. Characterization of silica nanosheets

The synthesis of SN was conducted by inducing the conversion of APTES to silica on GO and then incinerating GO by heating in an air atmosphere. TGA was conducted to determine the calcination temperature of GO. According to the TGA curve of APTES-GO (Figure 2-5a), the weight decrease derived from the combustion of carbon was confirmed to be >500 °C.[36] According to the TGA result and a previous report,[14] the heating temperature and time were set to 550 °C and 6 h, respectively. The change of chemical structure from APTES-GO to SN was confirmed using FTIR, XPS, and Raman spectra. In the FTIR spectrum of SN (Figure 2-5b), the GO- and APTES-derived peaks disappeared, while peaks for the Si–O–Si asymmetric stretching vibration (1051 cm^{-1}), Si–O–Si symmetric stretching vibration (795 cm^{-1}), and silanol group (Si–OH, 3242, 961 cm^{-1}) were observed.[37] The peaks around 1640 cm^{-1} and 3380 cm^{-1} were attributed

to the bending vibration and stretching vibration of physisorbed water, respectively.[37] Figure 2-5c shows the high resolution XPS spectrum of SN in the Si 2p region. The spectrum was deconvoluted to SiO_2 (105.5 eV), Si–O (104.3 eV), and Si–Si–O or Si–C (101.2 eV),[32,38,39] indicating that the formation of silica was successful. The binding energies of the SiO_2 and Si-O peaks may have been higher than their generally accepted positions because of the charging effect of silica.[39,40] The Raman spectra of APTES-GO and SN are shown in Figure 2-5d. The G-band (1580 cm^{-1}) and D-band (1350 cm^{-1}) derived from GO were observed in APTES-GO. After the fabrication of SN by calcination at 550 °C, no peaks derived from GO were observed, confirming the removal of GO. All of these results indicate the synthesis of SiO_2 and removal of GO.

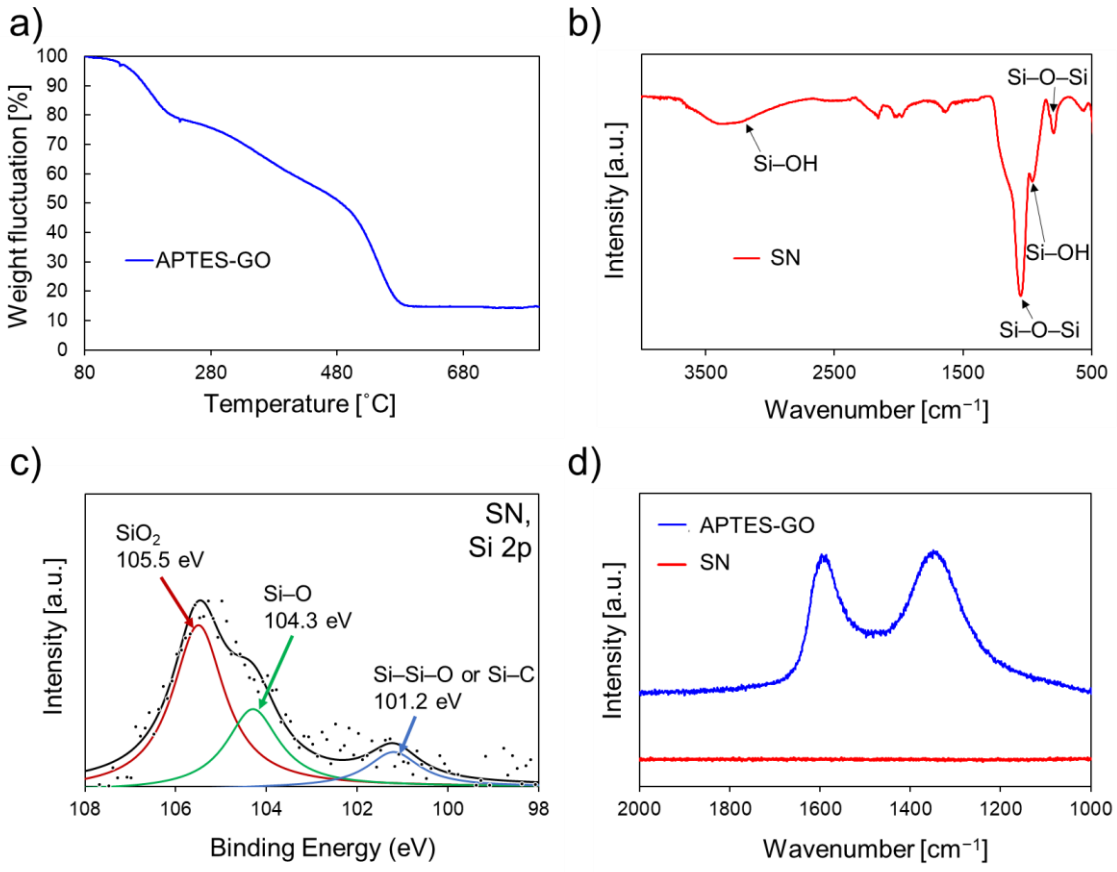

Figure 2-5. a) TGA curve of APTES-GO in air, b) FTIR spectrum of SN, c) high resolution XPS spectrum of SN at Si 2p region, and d) Raman spectra of APTES-GO and SN.

SEM analysis confirmed that the SN structure was formed predominantly (Figure 2-6), although portions of the SN were wrinkled and agglomerated (Figure 2-7) due to the partial agglomeration of APTES-GO (Figure 2-8). AFM measurements of SN (Figure 2-9) revealed that the sheet thicknesses were 0.8–1.3 nm (n = 10, avg.= 1.1 nm), almost corresponding to the interlayer distances of GO in APTES-GO (1.2 nm).

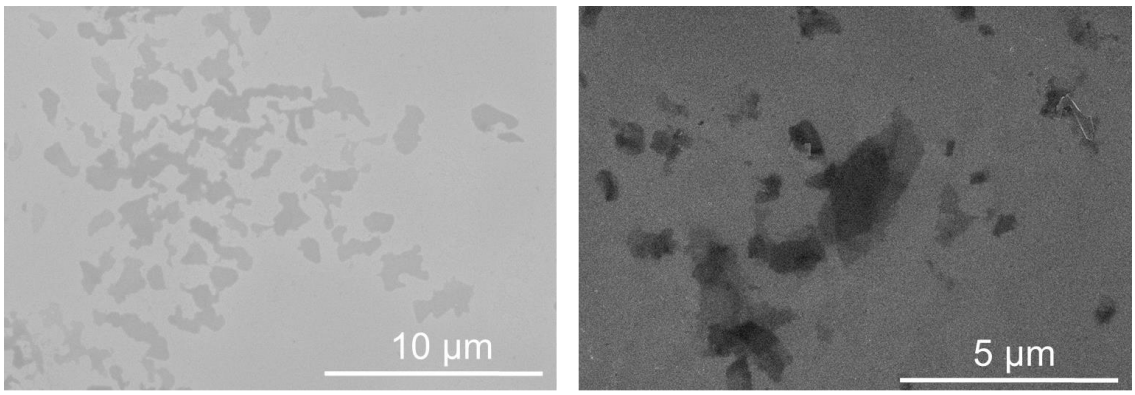

Figure 2-6. SEM image of SN.

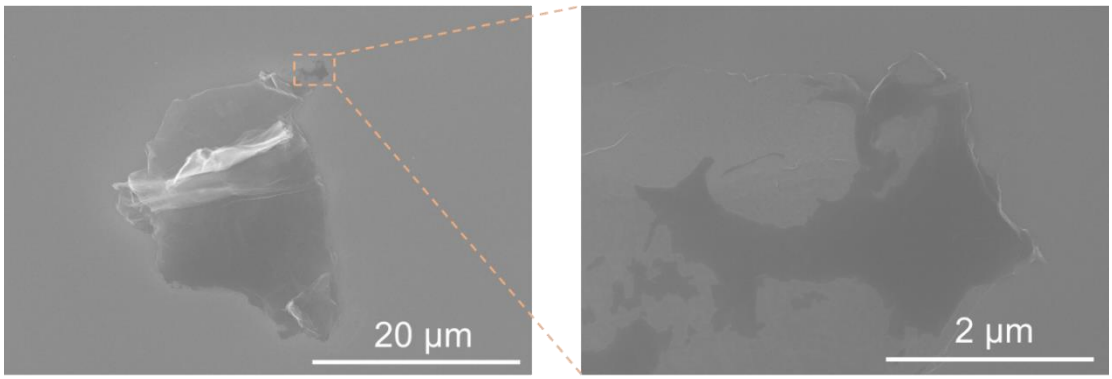

Figure 2-7. SEM images of a large particle in SN.

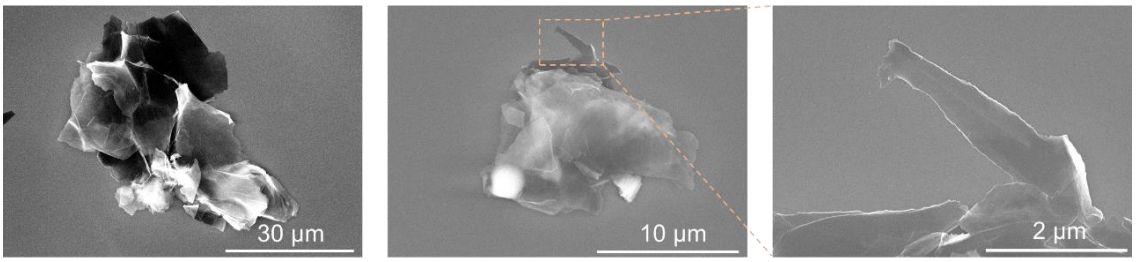

Figure 2-8. SEM images of agglomerated APTES-GO.

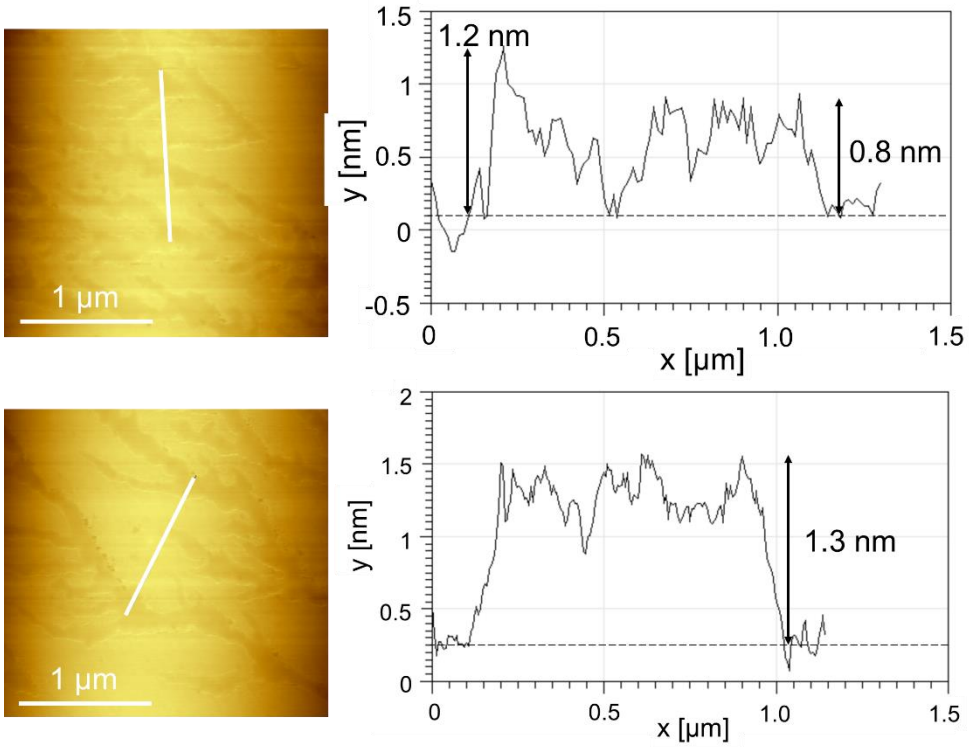

Figure 2-9. AFM images and height profiles of SN.

The representative XRD pattern of SN is shown in Figure 2-10. No sharp peak was observed, suggesting that SN had an amorphous structure.

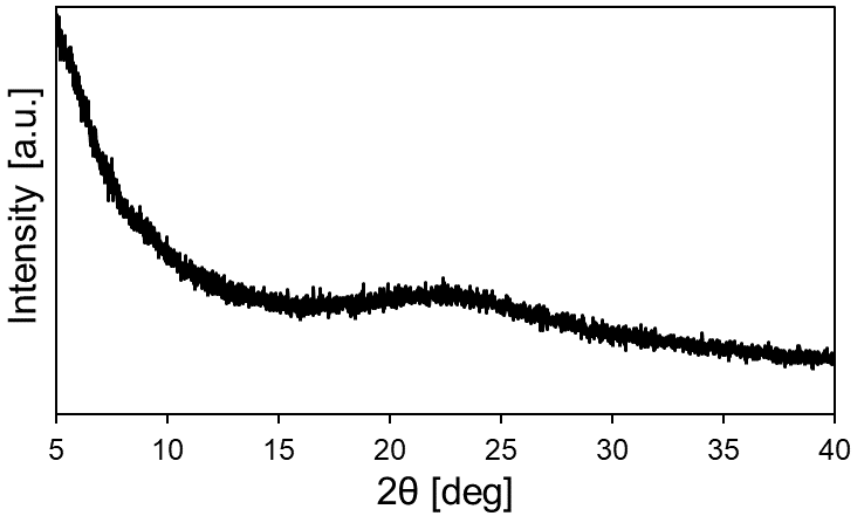

Figure 2-10. XRD pattern of SN.

N_2 adsorption–desorption tests were performed to measure the surface areas and pore structures. The S_{BET} of SN was 904 m^2 g^{-1}, dramatically increasing from APTES-GO (15 m^2 g^{-1}). This result may be due to the amorphous and porous structure of SN. The N_2 adsorption isotherm (Figure 2-11a) revealed the presence of micropores in SN. The pore size distribution obtained using the HK method (Figure 2-11b) contained several peaks associated with different pore sizes, suggesting that the silica nanosheets assembled randomly because of the processing and inherent amorphous structure (Figure 2-10).

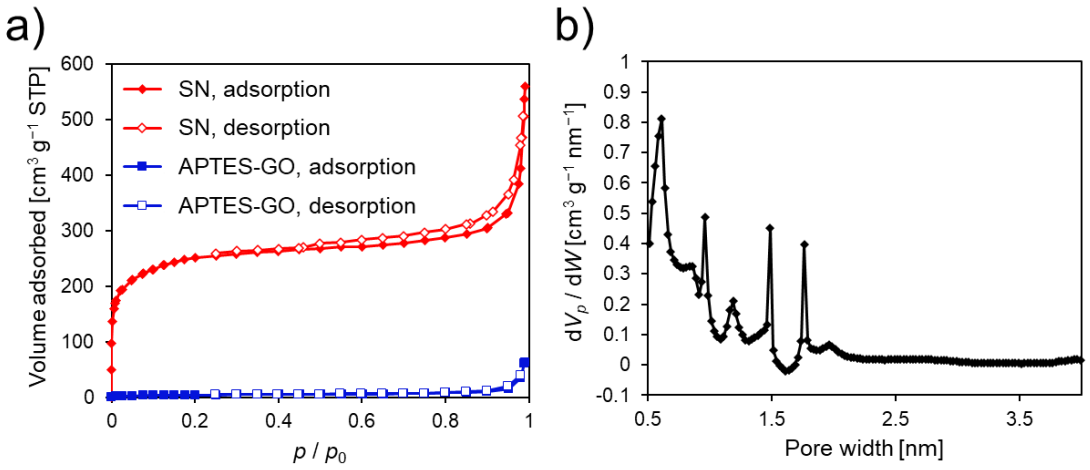

Figure 2-11. a) N_2 adsorption–desorption isotherms, and b) pore size distribution of SN by analyzing the N_2 adsorption isotherm with the HK method.

Table 2-4 compares SN obtained in this study with those developed in previous reports.[14,16–19,41–48] The thickness of 1 nm is the thinnest among the silica nanosheets synthesized using a bottom-up method with silica precursors at the time of the publication. After the publication of this research contents, the synthesis of ultrathin silica nanosheets at the 1 nm level has been reported.[49,50] Compared with them, the synthesized silica nanosheets in this study possessed both the excellent specific surface area (ca. 900 m^2 g^{-1}) and the ultrathin thickness (ca. 1 nm).

Table 2-4. Comparative table from the literature of other silica nanosheets.

Template used, precursors	**Thickness [nm]**	**Specific surface area [m^2 g^{-1}]**	**Ref.**
GO (APTES-GO)	0.8–1.3 (avg.= 1.1)	904	This study
GO	8	N.D.	18
GO	3.7	N.D.	41 (GO coated with a silica layer)
GO, CTAB	28	N.D.	42 (graphene oxide based mesoporous silica sheets)
GO, CTAB	28	930	19 (graphene-based mesoporous silica sheets)
g-C_3N_4	6–9, 12–15, 17–20	1071, 1061, 1123	16
g-C_3N_4, P123	N.D.	464	17
CTAB	3.7	1420	14
Leucine-lysine peptide	2.1	N.D.	43
PEG-*b*-PLL	30	N.D.	44
Dendrimer polyamidoamine	N.D.	779	45
C_{16}-L-Ala, P123	50	190	46
PDMAEMA-*b*-PS	35	71	47
Layered silicate RUB-18 (preparation with delamination)	1.3–1.7	53	48
GO	1.6, 1.5	87, 248	49 (published after this content publication)
Brij52	0.9	N.D.	50 (published after this content publication)

Abbreviations of Table 2-4

*CTAB: Cetyltrimethylammonium bromide

**P123: Symmetric triblock copolymer comprising poly(ethylene oxide) (PEO) and poly(propylene oxide) (PPO) (PEO-PPO-PEO)

***PEG-*b*-PLL: Diblock copolymer comprising poly(ethylene glycol) and poly-L-lysine

**** C_{16}-L-Ala: *N*-palmitoyl-L-alanine

*****PDMAEMA-*b*-PS: Diblock copolymer comprising poly[2-(dimethylamino)ethyl methacrylate] and polystyrene

****** Brij52: Polyethylene glycol hexadecyl ether

*******N.D.: No data

2-1-3-3. Evaluation of scale study of silica nanosheet synthesis

The potential for scaling-up the synthesis was investigated using 1 and 5 g of GO. Table 2-5 shows the yield of SN from APTES-GO at each scale. The yields at 0.2 g, 1 g, and 5 g of GO were almost the same: 21%, 20%, and 21%, respectively.

Table 2-5. Yields of SN from APTES-GO at each scale (GO amount).

Scale [g]	**Amounts of APTES-GO** [mg]	**Amounts of obtained SN** [mg]	**Yield** [%]
0.2	41.8	8.9	21
1	123.7	25.2	20
5	238.2	48.9	21

Additionally, the N_2 adsorption–desorption isotherms, S_{BET} and V_{total} of the materials at each scale are shown in Figure 2-12 and Table 2-6, and the specific surface areas of SN were >700 m^2 g^{-1} under all conditions. The lower S_{BET} obtained at the 5 g scale compared with other scales may be due to the agglomeration of GO or APTES-GO during the preparation process. AFM images

and height profiles of SN produced at the 5 g scale (Figure 2-13) revealed that sheets were mainly formed with thicknesses around 1 nm, similar to the 0.2 g scale. The results indicate that this SN synthesis method can be scaled up to 5 g batches without reductions in yield or material quality.

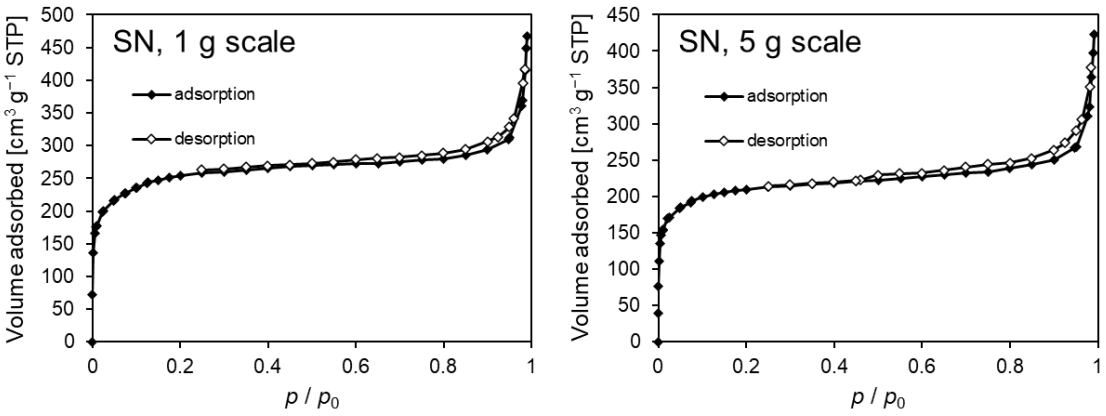

Figure 2-12. N_2 adsorption–desorption isotherms of SN at 1g scale and 5 g scale.

Table 2-6. S_{BET} and V_{total} of SN at each scale.

Scale [g]	S_{BET} [$m^2\ g^{-1}$]	V_{total} [$cm^3\ g^{-1}$]
0.2	904	0.850
1	922	0.719
5	778	0.644

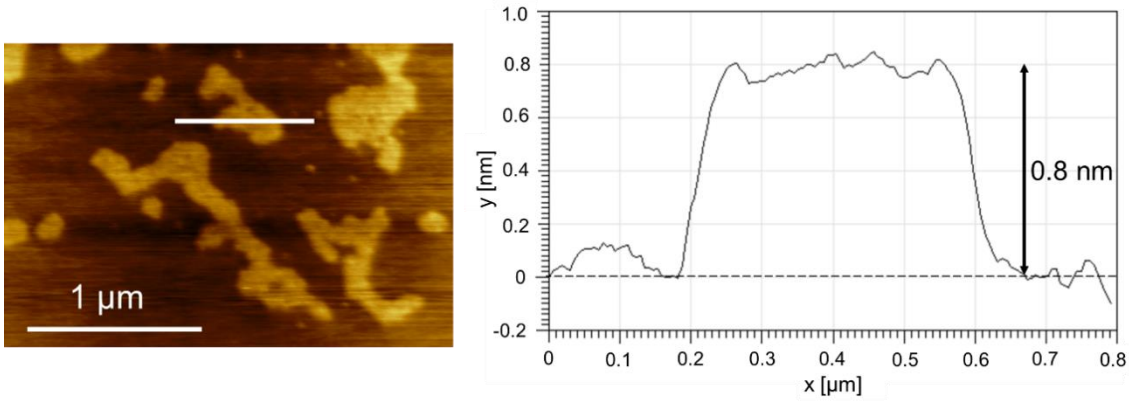

Figure 2-13. AFM image and the height profile of SN at 5 g scale.

2-1-4. Conclusion

In summary, ultrathin silica materials, i.e., SN, were synthesized using GO as a template. After converting APTES between the GO interlayers into silica and removing the GO by combusting the carbon, the amorphous silica was produced. The SN exhibited thicknesses around 1 nm, which is the lowest thickness reported for silica nanosheets synthesized using a bottom-up method from a silica precursor. Furthermore, the synthesized SN had relatively high specific surface areas (904 m^2 g^{-1}). By conducting further evaluation (e.g., thermal and chemical stabilities, dispersibility, and strength) tests to understand the performance of the material, the synthesized silica nanosheets can be used as building blocks for the solid electrolyte of batteries, catalyst supports, and gas adsorbents. Moreover, the key technology of ultrathin silica synthesis, namely surface functionalization of the GO template, will lead to new fields in two-dimensional material science by fine-tuning the thickness and agglomeration-free SN.

The content of this section was adapted with permission from the following paper:
Takeuchi, Y.; Obata, S.; Ohkura, K.; Nishina, Y. In Situ Synthesis of Ultrathin Amorphous Silica Nanosheet with Large Specific Surface Area on Graphene Oxide. *ACS Materials Lett.* **2022**, *4*, 2590–2596. (© 2022 American Chemical Society)

https://doi.org/10.1021/acsmaterialslett.2c00805

A direct link to the Published Work: https://pubs.acs.org/articlesonrequest/AOR-MRFPEHMAAXFPKAPVPJS4?_gl=1*a344dq*_ga*MTAzNjE4MTAyNS4xNzE3MzQ2Njg5*_ga_XP5JV6H8Q6*MTczMzA1NDU4Ni4xOS4wLjE3MzMwNTQ1ODYuNjAuMC4w

2-1-5. References

(1) Miao, Z.; Tao, S.; Wang, Y.; Yu, Y.; Meng, C.; An, Y. Hierarchically Porous Silica as an Efficient Catalyst Carrier for High Performance Vis-Light Assisted Fenton Degradation. *Microporous Mesoporous Mater*. **2013**, *176*, 178–185.

(2) Tang, R.; Zhu, Z.; Li, C.; Xiao, M.; Wu, Z.; Zhang, D.; Zhang, C.; Xiao, Y.; Chu, M.; Genest, A.; Rupprechter, G.; Zhang, L.; Zhang, X.; He, L. Ru-Catalyzed Reverse Water Gas Shift Reaction with Near-Unity Selectivity and Superior Stability. *ACS Mater. Lett.* **2021**, *3*, 1652–1659.

(3) Florek, J.; Caillard, R.; Kleitz, F. Evaluation of Mesoporous Silica Nanoparticles for Oral Drug Delivery – Current Status and Perspective of MSNs Drug Carriers. *Nanoscale* **2017**, *9*, 15252–15277.

(4) Chen, J.-F.; Ding, H.-M.; Wang, J.-X.; Shao, L. Preparation and Characterization of Porous Hollow Silica Nanoparticles for Drug Delivery Application. *Biomaterials* **2004**, *25*, 723–727.

(5) Sakamoto, Y.; Nagata, K.; Yogo, K.; Yamada, K. Preparation and CO_2 Separation Properties of Amine-Modified Mesoporous Silica Membranes. *Microporous Mesoporous Mater.* **2007**, *101*, 303–311.

(6) Kanezashi, M.; Yada, K.; Yoshioka, T.; Tsuru, T. Design of Silica Networks for Development of Highly Permeable Hydrogen Separation Membranes with Hydrothermal Stability. *J. Am. Chem. Soc.* **2009**, *131*, 414–415.

(7) Wang, J.; Liu, Y.; Cai, Q.; Dong, A.; Yang, D.; Zhao, D. Hierarchically Porous Silica Membrane as Separator for High-Performance Lithium-Ion Batteries. *Adv. Mater.* **2022**, *34*, 2107957.

(8) Graham, T. XXXV.—On the Properties of Silicic Acid and other Analogous Colloidal Substances. *J. Chem. Soc.* **1864**, *17*, 318–327.

(9) Lei, Q.; Guo, J.; Noureddine, A.; Wang, A.; Wuttke, S.; Brinker, C. J.; Zhu, W. Sol–Gel-Based Advanced Porous Silica Materials for Biomedical Applications. *Adv. Funct. Mater.* **2020**, *30*, 1909539.

(10) Wen, J.; Wilkes, G. L. Organic/Inorganic Hybrid Network Materials by the Sol−Gel

Approach. *Chem. Mater.* **1996**, *8*, 1667–1681.

(11) Yanagisawa, T.; Shimizu, T.; Kuroda, K.; Kato, C. The Preparation of Alkyltrimethylammonium–Kanemite Complexes and Their Conversion to Microporous Materials. *Bull. Chem. Soc. Jpn.* **1990**, *63*, 988–992.

(12) Kresge, C. T.; Leonowicz, M. E.; Roth, W. J.; Vartuli, J. C.; Beck, J. S. Ordered Mesoporous Molecular Sieves Synthesized by a Liquid-Crystal Template Mechanism. *Nature* **1992**, *359*, 710–712.

(13) Zhao, D.; Huo, Q.; Feng, J.; Chmelka, B. F.; Stucky, G. D. Nonionic Triblock and Star Diblock Copolymer and Oligomeric Surfactant Syntheses of Highly Ordered, Hydrothermally Stable, Mesoporous Silica Structures. *J. Am. Chem. Soc.* **1998,** *120*, 6024–6036.

(14) Singh, B.; Polshettiwar, V. Solution-Phase Synthesis of Two-Dimensional Silica Nanosheets Using Soft Templates and Their Applications in CO_2 Capture. *Nanoscale* **2019**, *11*, 5365–5376.

(15) Nakanishi, K. Sol–Gel Process of Oxides Accompanied by Phase Separation. *Bull. Chem. Soc. Jpn.* **2006**, *79*, 673–691.

(16) Du, X.; Zou, G.; Wang, X. Controllable and Scalable Synthesis of Ordered Mesoporous Silica Nanosheets by Using Acidified g-C_3N_4 as a Lamellar Surfactant. *Nanotechnology* **2017**, *28*, 29LT01.

(17) Shen, Z.; Cai, Q.; Yin, C.; Xia, Q.; Cheng, J.; Li, X.; Wang, Y. Facile Synthesis of Silica Nanosheets with Hierarchical Pore Structure and Their Amine-Functionalized Composite for Enhanced CO_2 Capture. *Chem. Eng. Sci.* **2020**, *217*, 115528.

(18) Kou, L.; Gao, C. Making Silicananoparticle-Covered Graphene Oxide Nanohybrids as General Building Blocks for Large-Area Superhydrophilic Coatings. *Nanoscale* **2011**, *3*, 519–528.

(19) Yang, S.; Zhan, L.; Xu, X.; Wang, Y.; Ling, L.; Feng, X. Graphene-Based Porous Silica Sheets Impregnated with Polyethyleneimine for Superior CO_2 Capture. *Adv. Mater.* **2013**, *25*, 2130–2134.

(20) Zhu, Y.; Murali, S.; Cai, W.; Li, X.; Suk, J. W.; Potts, J. R.; Ruoff, R. S. Graphene and Graphene Oxide: Synthesis, Properties, and Applications. *Adv. Mater.* **2010**, *22*, 3906–3924.

(21) Zhi, X.; Mao, Y.; Yu, Z.; Wen, S.; Li, Y.; Zhang, L.; Chan, T. W.; Liu, L. γ-Aminopropyl Triethoxysilane Functionalized Graphene Oxide for Composites with High Dielectric Constant and Low Dielectric Loss. *Compos. Part A Appl. Sci. Manuf.* **2015**, *76,* 194–202.

(22) Zhang, F.; Jiang, H.; Li, X.; Wu, X.; Li, H. Amine-Functionalized GO as an Active and Reusable Acid–Base Bifunctional Catalyst for One-Pot Cascade Reactions. *ACS Catal.* **2014**, *4*, 394–401.

(23) Serodre, T.; Oliveira, N. A. P.; Miquita, D. R.; Ferreira, M. P.; Santos, A. P.; Resende, V. G.; Furtado, C. A. Surface Silanization of Graphene Oxide Under Mild Reaction Conditions. *J. Braz. Chem. Soc.* **2019**, *30*, 2488–2499.

(24) Matsuo, Y.; Nishino, Y.; Fukutsuka, T.; Sugie, Y. Introduction of Amino Groups into the Interlayer Space of Graphite Oxide Using 3-Aminopropylethoxysilanes. *Carbon* **2007**, *45*, 1384–1390.

(25) Hummers, W. S.; Offeman, R. E. Preparation of Graphitic Oxide. *J. Am. Chem. Soc.* **1958**, *80*, 1339.

(26) Zhang, T.-Y.; Zhang, D. Aqueous Colloids of Graphene Oxide Nanosheets by Exfoliation of Graphite Oxide without Ultrasonication. *Bull. Mater. Sci.* **2011**, *34*, 25–28.

(27) Nekahi, A.; Marashi, S. P. H.; Fatmesari, D. H. Modified Structure of Graphene Oxide by Investigation of Structure Evolution. *Bull. Mater. Sci.* **2015**, *38*, 1717–1722.

(28) Pytlakowska, K.; Kozik, V.; Matussek, M.; Pilch, M.; Hachuła, B.; Kocot, K. Glycine Modified Graphene Oxide as a Novel Sorbent for Preconcentration of Chromium, Copper, and Zinc Ions from Water Samples Prior to Energy Dispersive X-Ray Fluorescence Spectrometric Determination. *RSC Adv.* **2016**, *6*, 42836–42844.

(29) Saha, J.; Bhowmik, K.; Das, I.; De, G. Pd–Ni Alloy Nanoparticle Doped Mesoporous SiO_2 Film: The Sacrificial Role of Ni to Resist Pd-Oxidation in the C–C Coupling Reaction. *Dalton Trans.* **2014**, *43*, 13325–13332.

(30) Pantoja, M.; Abenojar, J.; Martínez, M. A.; Velasco, F. Silane Pretreatment of

Electrogalvanized Steels: Effect on Adhesive Properties. *Int. J. Adhes. Adhes.* **2016**, *65*, 54–62.

(31) Pu, X.; Zhang, H.-B.; Li, X.; Gui, C.; Yu, Z.-Z. Thermally Conductive and Electrically Insulating Epoxy Nanocomposites with Silica-Coated Graphene. *RSC Adv.* **2014**, *4*, 15297–15303.

(32) Kaur, A.; Chahal, P.; Hogan, T. Selective Fabrication of SiC/Si Diodes by Excimer Laser Under Ambient Conditions. *IEEE Electron Device Lett.* **2016**, *37*, 142–145.

(33) Avila, A.; Montero, I.; Galán, L.; Ripalda, J. M.; Levy, R. Behavior of Oxygen Doped SiC Thin Films: An x-Ray Photoelectron Spectroscopy Study. *J. Appl. Phys.* **2001**, *89*, 212–216.

(34) Peng, Y.; Pan, N.; Wang, D.; Yang, J.; Guo, Z.; Yuan, W. A Si–O–Si Bridge Assembled from 3-Mercaptopropyltrimethoxysilane and Silicon Carbide for Effective Charge Transfer in Photocatalysis. *J. Mater. Sci.* **2018**, *53*, 12432–12440.

(35) Alfonsetti, R.; Lozzi, L.; Passacantando, M.; Picozzi, P.; Santucci, S. XPS Studies on SiO_x Thin Films. *Appl. Surf. Sci.* **1993**, *70–71*, 222–225.

(36) Bourlinos, A. B.; Gournis, D.; Petridis, D.; Szabó, T.; Szeri, A.; Dékány, I. Graphite Oxide: Chemical Reduction to Graphite and Surface Modification with Primary Aliphatic Amines and Amino Acids. *Langmuir* **2003**, *19*, 6050–6055.

(37) Musić, S.; Filipović-Vinceković, N.; Sekovanić, L. Precipitation of Amorphous SiO_2 Particles and Their Properties. *Braz. J. Chem. Eng.* **2011**, *28*, 89–94.

(38) Gustus, R.; Gruber, W.; Wegewitz, L.; Geckle, U.; Prang, R.; Kübel, C.; Schmidt, H.; Maus-Friedrichs, W. Decomposition of Amorphous Si_2C by Thermal Annealing. *Thin Solid Films* **2014**, *552*, 232–240.

(39) Post, P.; Wurlitzer, L.; Maus-Friedrichs, W.; Weber, A. P. Characterization and Applications of Nanoparticles Modified in-Flight with Silica or Silica-Organic Coatings. *Nanomaterials* **2018**, *8*, 530.

(40) Barr, T. L. An XPS Study of Si as It Occurs in Adsorbents, Catalysts, and Thin Films. *Appl. Surf. Sci.* **1983**, *15*, 1–35.

(41) Lu, Z.; Zhu, J.; Sim, D.; Zhou, W.; Shi, W.; Hng, H. H.; Yan, Q. Synthesis of Ultrathin Silicon Nanosheets by Using Graphene Oxide as Template. *Chem. Mater.* **2011**, *23*, 5293–5295.

(42) Yang, S.; Feng, X.; Wang, L.; Tang, K.; Maier, J.; Müllen, K. Graphene-Based Nanosheets with a Sandwich Structure. *Angew. Chem. Int. Ed.* **2010**, *49*, 4795–4799.

(43) Lutz, H.; Jaeger, V.; Berger, R.; Bonn, M.; Pfaendtner, J.; Weidner, T. Biomimetic Growth of Ultrathin Silica Sheets Using Artificial Amphiphilic Peptides. *Adv. Mater. Interfaces* **2015**, *2*, 1500282.

(44) Chen, H.; Xia, L.; Fu, W.; Yang, Z.; Li, Z. One-Step Synthesis of Water Dispersible Silica Nanoplates. *Chem. Commun.* **2013**, *49*, 1300–1302.

(45) Shen, J.; Wu, Y.-n.; Zhang, B.; Li, F. Preparation of Mesoporous Silica Nanosheets through Electrospinning: A Novel Scroll Mechanism. *RSC Adv.* **2014**, *4*, 12805–12808.

(46) Nakanishi, K.; Tomita, M.; Kato, K. Synthesis of Amino-Functionalized Mesoporous Silica Sheets and Their Application for Metal Ion Capture. *J. Asian Ceram. Soc.* **2015**, *3*, 70–76.

(47) Yao, D.; Chen, Y.; Jin, R. Different Dimensional Silica Materials Prepared Using Shaped Block Copolymer Nanoobjects as Catalytic Templates. *J. Mater. Chem. B* **2015**, *3*, 5786–5794.

(48) Awaya, K.; Sekiguchi, K.; Kitagawa, H.; Yamada, S.; Ida, S. Preparation of Silicate Nanosheets by Delaminating RUB-18 for Transparent, Proton Conducting Membranes. *Chem. Commun.* **2021**, *57*, 6304–6307.

(49) Birdsong, B. K.; Hoogendoorn, B. W.; Nilsson, F.; Andersson, R. L.; Capezza, A. J.; Hedenqvist, M. S.; Farris, S.; Guerrero, A.; Olsson, R. T. Large-Scale Synthesis of 2D-Silica (SiO_x) Nanosheets Using Graphene Oxide (GO) as a Template Material. *Nanoscale* **2023**, *15*, 13037–13048.

(50) Yamamoto, E.; Fujihara, K.; Takezaki, Y.; Ito, K.; Shi, Y.; Kobayashi, M.; Osada, M. Free-Standing Molecularly Thin Amorphous Silica Nanosheets. *Small* **2023**, *19*, 2300022.

Chapter 3. Material synthesis using clay

ABSTRACT: Clay has high thermal stability. Therefore, I conceived that clay could be used as a carrier to support the formed materials on the surface during calcination. In addition to this property, I also utilized the functionality of clay using electrostatic interactions between negatively charged clay surface and cationic materials, and worked on the formation of metal oxides on the surface of clay. Metal oxides have the excellent functions including high thermal stability, electrical properties, catalytic performance, and adsorption properties of acid gases such as CO_2 via the acid–base interactions. However, they suffer from low reserves, porosity control, and low adsorption efficiency per weight compared with lightweight materials including carbon and silica. To solve these issues, various methods for supporting metal oxides on porous carriers, such as decomposition–precipitation and impregnation, have been investigated, but controlling the formation of metal oxide on clay nanosheets remains as a challenge. Herein, a soft-template method for supporting metal oxide (CuO_x) nanoparticles on activated clay nanosheets were developed. The intercalation of polyethyleneimine (PEI)–Cu^{2+} complexes between the layers of clay nanosheets followed by calcination to construct CuO_x and remove the PEI templates afforded CuO_x/clay nanocomposites. The constructed CuO_x/clay nanocomposites had the close porosity to that of clay. Tuning the Cu^{2+}/PEI ratio in PEI–Cu^{2+} complex allowed to control CuO_x states (loadings, particle sizes, etc.). Tuning of the supporting conditions allowed constructing a structure suitable for CO_2 uptake.

3-1. Synthesis of CuO_x nanoparticles on clay using a polymer template

3-1-1. Introduction

Metal oxides have excellent durability (thermal stability) compared to organic materials, electrical properties, catalytic performance, and acid gases (e.g., CO_2) adsorption sites based on the acid–base (e.g., Lewis acid–base) interactions, which form stronger bonds with CO_2 (e.g., a metal–carbonate bond) than those of physical adsorption.[1] In addition, metal oxides have the different properties by changing the metal species (e.g., Ti, Mn, Co, Cu, and Zr).[2–5] Utilizing these functions, metal oxides have applied in a wide variety of fields including battery,[6] catalyst,[7,8] and

adsorption.[9] However, metal oxides have several issues and drawbacks, including low reserves of metal elements in transition metal except for Fe, porosity control, and lower adsorption efficiency per weight than lightweight materials such as carbon and silica. Recently, the research to solve these issues and drawbacks has focused on supporting metal oxides on porous carriers, which is expected to alleviate weight issues by reducing the proportion of heavy metals in the adsorbent, contributing to the construction of metal oxide/porous carrier hybrids with excellent pore structures.[10,11] Metal oxides have been previously supported on nanoporous materials like activated carbon and mesoporous materials, achieving enhanced performance such as CO_2 adsorption property compared to the bare carriers.[1,12,13]

CuO is a p-type semiconductor with lower toxicity compared to Ni and Co species, a band gap of 1.2–2.1 eV and catalytic properties,[14–16] moderate enthalpy in CO_2 adsorption ($\Delta H = -45.5$ kJ mol^{-1}) which contributes to decrease of the regeneration temperature (energy) compared to amine and MgO,[17] and it has been employed in diverse applications, such as catalysts for H_2 evolution[15] and NO reduction with CO,[18] sensors,[19,20] adsorbents for CO_2,[17] and batteries (e.g., anode material for Li-ion batteries).[21] CuO_x (and Cu^{2+}) species have been also supported on clay, which has abundant resources, low cost, and high thermal stability, using various methods, such as ion exchange,[22] deposition-precipitation,[23] precursor reduction,[24,25] and impregnation methods.[26] Recently, organic polymers have been used to support metals on clay. Utilizing the electrostatic interaction between the negative charges between the layers of clay and the positive charges of cationic molecules, organic polymer–inorganic (clay) hybrids can be fabricated by intercalating cationic monomers or polymers such as aniline,[27] chitosan,[28] poly(1-methyl-4-vinylpyridinium),[29] and PEI.[30] Amine groups can interact with the metal ions; previously, utilizing the chitosan or chitosan-derived carbon, Pd or Co/clay/chitosan or chitosan-derived carbon composites were developed.[31–33] PEI, which has a higher proportion of N atoms in the polymer framework than chitosan, has been also used for developing the metal/clay composites. Cu/PEI/clay and Au/PEI/clay composites were fabricated by introducing PEI-capped Cu nanoparticles between clay nanosheets and reducing the gold ions on PEI-intercalated clay, respectively.[34,35] Furthermore, Wang et al. reported a templated synthesis for supporting metal nanoparticles on a carrier;

specifically, they fabricated mesoporous alumina functionalized with uniformly dispersed Pt nanoparticles using a dendrimer template.[36] However, studies to support CuO_x on clay by intercalating a cationic polymer and a soft-template method, which is expected to enable the precise control of the loading and size of CuO_x as well as the porosity of the resulting CuO_x/clay architectures, had not progressed.

Herein, the soft-template method for supporting CuO_x nanoparticles on activated clay was developed. PEI–Cu^{2+} complexes were introduced onto the surface and between the layers of clay nanosheets. Subsequently, the calcination under an air atmosphere was conducted to produce CuO_x and remove the PEI template simultaneously. As a result, nanocomposites consisting of CuO_x and clay nanosheets (hereinafter referred to as CuO_x/clay nanocomposites) were developed. Furthermore, the effects of the PEI-template method and Cu^{2+}/PEI ratio in PEI–Cu^{2+} complexes on the composite structure (i.e., porosity, CuO_x loading and particle size) were investigated. Finally, the CuO_x/clay nanocomposites were applied to CO_2 capture, and the impact of using the soft-template method for constructing the nanocomposites on the adsorption performance was investigated.

3-1-2. Experimental section

3-1-2-1. Chemicals

Montmorillonite K10 (activated clay, MT), PEI (average molecular weight: 600), and 0.1 mol L^{-1} NaOH solution were supplied by FUJIFILM Wako Pure Chemical Corporation, Japan. Copper(II) acetate monohydrate [$Cu(OAc)_2 \cdot H_2O$] used as copper source was purchased from Nacalai Tesque Inc., Japan. Distilled water purified using a purification system (RFD240NA, ADVANTEC) was used as water.

3-1-2-2. Synthesis

CuO_x/clay nanocomposites were synthesized with soft (PEI)-template method (Scheme 3-1). PEI (100, 200, 300, and 500 mg) and 1000 mg L^{-1} Cu^{2+} solution (100 mL) were mixed, and the solution was sonicated for 30 min to make the solution homogeneous and prepare PEI–Cu^{2+}

complexes. Subsequently, MT (500 mg) was added to the solution. The mixture was stirred at 500 rpm, 40 °C for 2 h, and filtered with polytetrafluoroethylene (PTFE) membrane (pore size: 0.2 μm). The residue was dried at 80 °C for 18 h (the sample name until this process: MT/PEIx-Cu, x: PEI amount). The dried sample was calcined at 500 °C for 5 h (ramping rate: 5 °C min^{-1}) under an air atmosphere to convert Cu^{2+} ions to CuO_x, remove PEI, and obtain the product (MT/PEIx-Cu 500 °C).

Scheme 3-1. Schematic illustration of the synthesis concept for CuO_x/clay nanocomposites using a soft-template method.

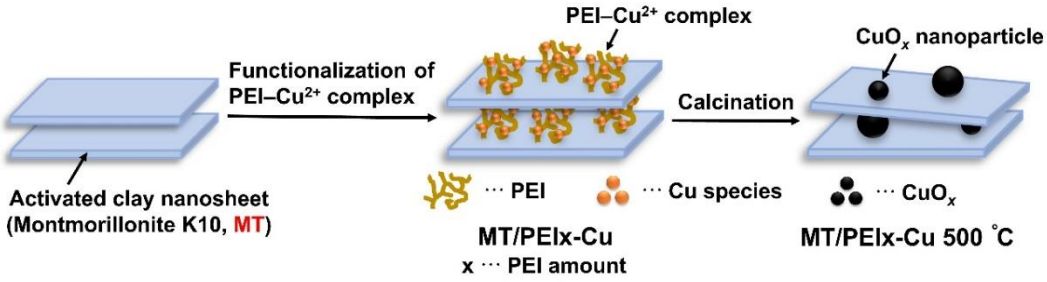

The comparative sample was prepared without adding PEI. MT (500 mg) was added to 1000 mg L^{-1} Cu^{2+} solution (100 mL). Subsequently, pH of the mixture was adjusted to 5 with 0.1 mol L^{-1} NaOH solution. pH was determined by referring to the paper about Cu^{2+} adsorption of clay.[37] The mixture was stirred at 500 rpm, 40 °C for 2 h, and filtered with PTFE membrane (pore size: 0.2 μm). The residue was dried at 80 °C for 18 h (the sample name until this process: MT/Cu). The dried sample was calcined at 500 °C for 5 h (ramping rate: 5 °C min^{-1}) under an air atmosphere to obtain the product (MT/Cu 500 °C).

3-1-2-3. Characterization

Powder XRD was measured using MiniFlex II (Rigaku Corporation, Japan) with monochromatic X-rays of Cu Kα (λ = 0.154 nm) at room temperature. The tube voltage, the current, 2θ range, and step size were 30 kV, 15 mA, 3–45°, and 0.02°, respectively. The chemical structures were analyzed with FTIR (DegiLab Japan Ltd., Japan, FTS4000MXK). The sample

was measured with KBr pressed disc method under atmospheric pressure at room temperature, and the measurement range was 500–4000 cm^{-1}. TGA was conducted with thermogravimetric-differential thermal analyzer (Rigaku Corporation, Japan, Thermo plus EVO2 TG-DTA8122). After keeping at 95 °C to remove water attached to materials, the temperature was raised to 800 °C (ramping rate: 10 °C min^{-1}), and the weight loss was calculated from the result of weight fluctuations. The overall morphology and element ratio were measured with SEM (KEYENCE CORPORATION, Japan, VE-9800)-EDX (KEYENCE CORPORATION, Japan, 971863SP). The SEM images were obtained at an accelerating voltage of 10 kV. The value of element ratio was the average of ten experiments. The Cu states in the materials were determined through XPS (JEOL JPS-9030, Japan). The X-ray source was Mg Kα (1253.6 eV). The path energies were 50 eV for wide scans and 10 eV for narrow scans, respectively. The measured sample was coated over the carbon tape on the substrate. (There is the possibility of the carbon and silicone contamination.) The charge compensation was achieved using a flood gun. The binding energy of the C 1s peak at 284.8 eV was used as a reference to calibrate the binding energy scale. The morphology of CuO_x on MT was observed with TEM (H-7650, Hitachi, Japan). The TEM observation was performed at 100 kV. The TEM images of the samples were analyzed using ImageJ software (1.52v; National Institutes of Health, Bethesda, MD, USA) to obtain the average particle sizes of CuO_x. The porosity was evaluated using BELSORP-mini (MicrotracBEL Corp., Japan). The adsorption–desorption tests were performed using N_2 as the adsorbate at 77 K to obtain the adsorption–desorption isotherms. All samples were evacuated at 110 °C for 6 h before the measurement. The isotherms were analyzed with the BET equation to determine the S_{BET}, and the V_{total} was estimated from the amount of adsorbed at relative pressure p/p_0 = 0.99. The pore size distribution was obtained by analyzing the adsorption isotherm with the BJH method.

3-1-2-4. CO_2 adsorption test

CO_2 uptake was measured using BELSORP-max (MicrotracBEL Corp., Japan). The adsorption test was performed at 303 K. The sample was evacuated at 110 °C for 12 h before the measurement.

3-1-3. Results and discussion

3-1-3-1. Synthesis and characterization of CuO_x/clay nanocomposites

The CuO_x/clay nanocomposites (MT/PEIx-Cu 500 °C) were constructed by intercalating a PEI–Cu^{2+} complex using a soft-template method as shown in Scheme 3-1. First, the PEI–Cu^{2+} complex was introduced into MT using the electric interactions between the negative charges of the clay layers and the positive charges of PEI and Cu^{2+}. Representative results obtained using 500 mg of PEI (MT/PEI500-Cu) are presented, and a sample without PEI (MT/Cu) was prepared for comparative purposes. The successful integration of the components was confirmed using FTIR, XRD, and TGA. The functional groups were detected with FTIR spectroscopy (Figure 3-1). In the spectrum of MT, bands derived from MT or adsorbed H_2O were observed at 3620 cm^{-1} (Al–OH), 3443 cm^{-1} (OH or H_2O), 1636 cm^{-1} (H_2O), 1053 cm^{-1} (Si–O), 935 cm^{-1} (OH), 797 cm^{-1} (Si–O stretching of quartz and silica), and 537 cm^{-1} (Al–O–Si deformation).[38–40] In addition to these bands, a C–H band attributable to acetic acid appeared at around 2900 cm^{-1} in the spectrum of MT/Cu (Figure 3-2).[41] Meanwhile, the spectrum of MT/PEI500-Cu showed a band due to N–H or $–CH_2–$ at 1462 cm^{-1}, which was not detected in the spectra of MT and MT/Cu, suggesting that PEI was successfully intercalated.[42,43]

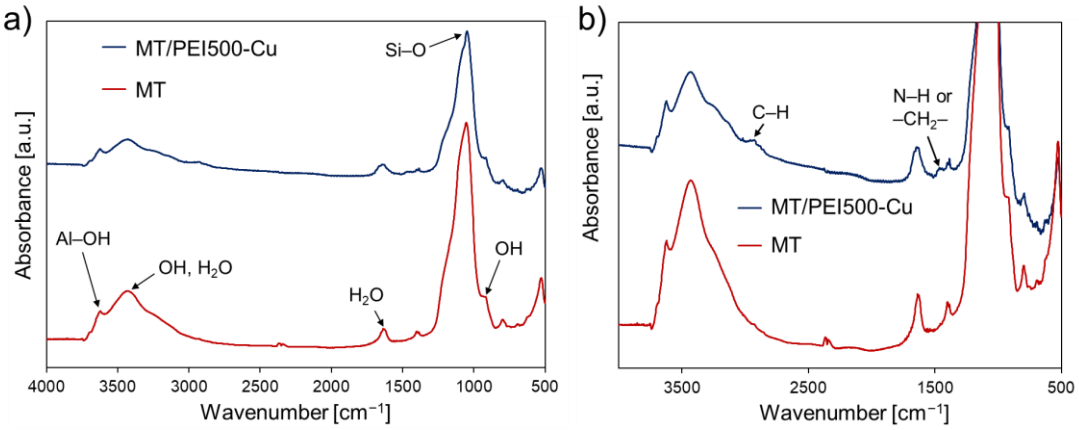

Figure 3-1. a) Wide and b) narrow FTIR spectra of MT and MT/PEI500-Cu.

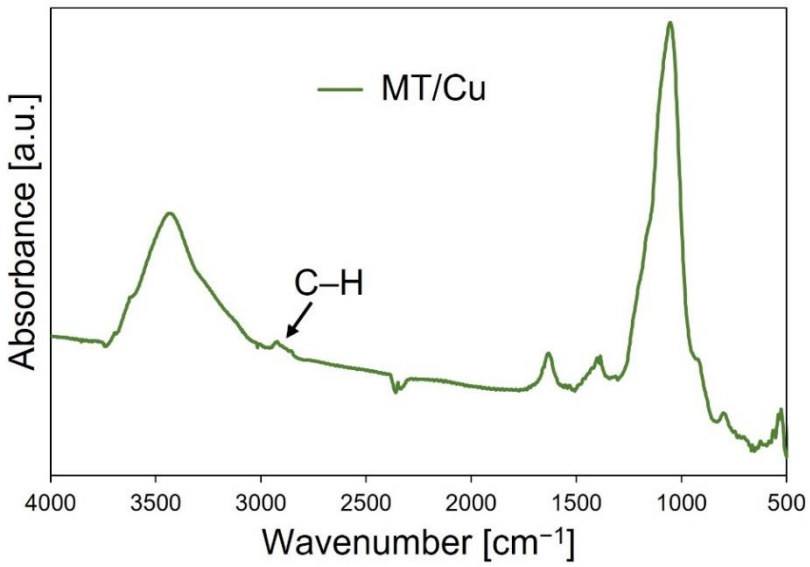

Figure 3-2. FTIR spectrum of MT/Cu.

The structural change upon intercalation was confirmed via powder XRD analysis (Figure 3-3). In the XRD pattern of MT, a profile corresponding to a basal spacing of 1.0 nm appeared at 8.9°. After introducing Cu^{2+} ions (MT/Cu) and the PEI–Cu^{2+} complex (MT/PEI500-Cu), the basal spacing (001) profiles were detected at 6.9° (1.3 nm) and 5.5° (1.6 nm), respectively. These increases in the basal spacing are in accord with the introduction of Cu^{2+} and the PEI–Cu^{2+} complex. The present of multiple peaks derived from the basal spacing was previously reported for cetyltrimethylammonium cation–adsorbed activated clay.[44]

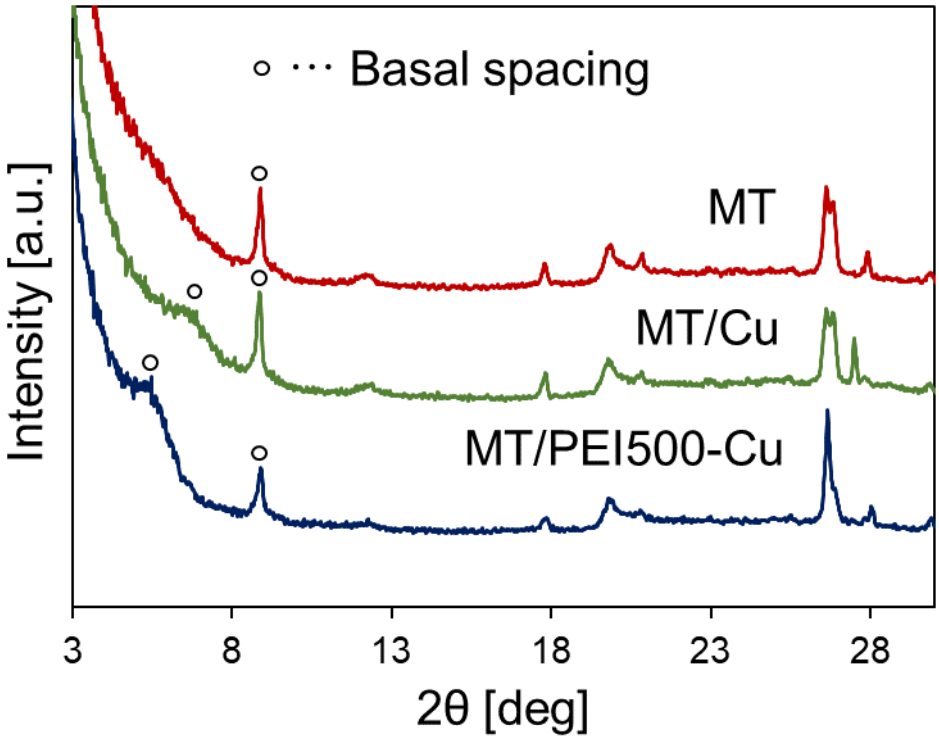

Figure 3-3. XRD patterns of MT, MT/Cu and MT/PEI500-Cu.

The PEI content in MT/PEIx-Cu was determined via TGA measurements (Figure 3-4). MT and MT/PEI500-Cu underwent a weight loss of 5.0 and 14.4 wt%, respectively, between 100 °C and 800 °C; accordingly, the PEI content in MT/PEI500-Cu was estimated to be 9.4 wt%. This value was close to that previously reported for a PEI/bentonite clay composite.[30,45] Upon decreasing the added amount of PEI and increasing the Cu^{2+}/PEI ratio (0.2 wt/wt in MT/PEI500-Cu, 0.3 wt/wt in MT/PEI300-Cu, 0.5 wt/wt in MT/PEI200-Cu, and 1 wt/wt in MT/PEI100-Cu), the PEI content in MT/PEIx-Cu tended to decrease (9.4 wt% in MT/PEI500-Cu, 6.5 wt% in MT/PEI300-Cu, 5.6 wt% in MT/PEI200-Cu, and 5.8 wt% in MT/PEI100-Cu; Figure 3-5). In the absence of Cu^{2+} (PEI only), the PEI contents in MT/PEIx (Figure 3-6) were relatively similar for added amounts of PEI of 100 mg (MT/PEI100, 8.4 wt%) and 500 mg (MT/PEI500, 9.9 wt%). The decreases of the PEI contents compared to MT/PEIx were 2.6 wt% in MT/PEI100-Cu and 0.5 wt% in MT/PEI500-Cu, respectively. Several studies reported that charge neutralization plays a major role in PEI adsorption.[35,46] Here, the change in the PEI content in MT/PEIx-Cu may be due to the positive

charge strength of the PEI–Cu^{2+} complex. Upon increasing the Cu^{2+}/PEI ratio, the PEI–Cu^{2+} complex has more cations (Cu^{2+}) per PEI chain, achieving charge neutralization with less amount of PEI–Cu^{2+} complex (Figure 3-7). The FTIR, XRD, and TGA results of MT and MT/PEIx-Cu suggest the introduction of PEI–Cu^{2+} complex.

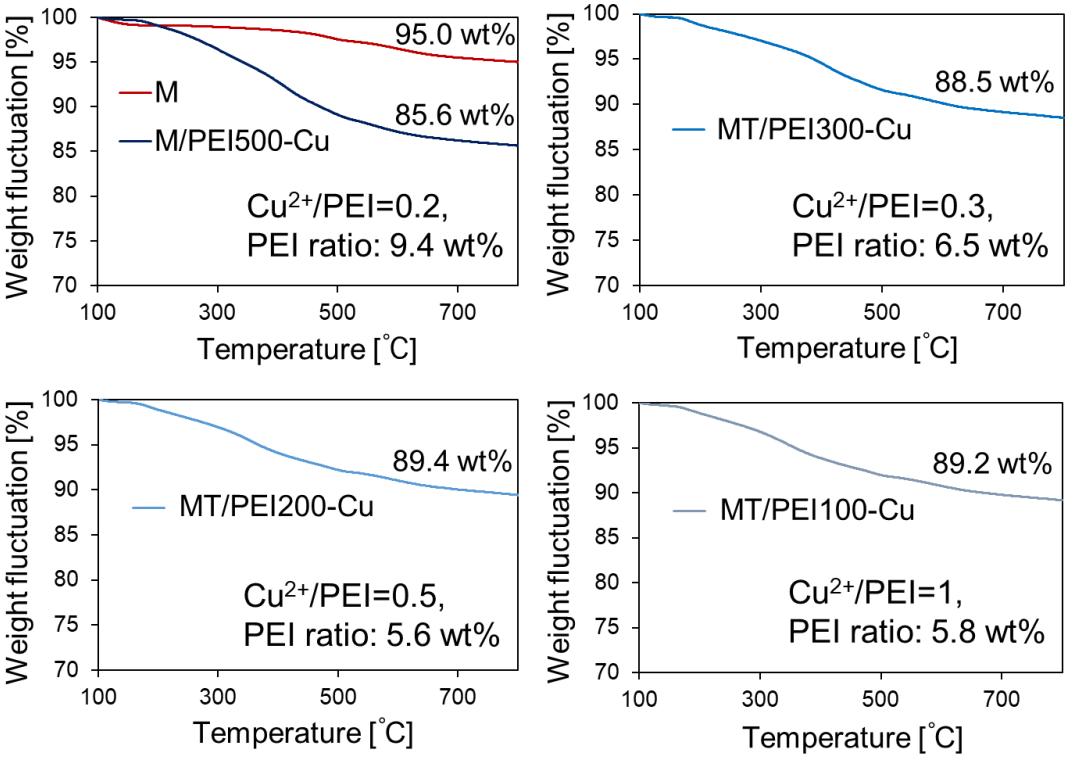

Figure 3-4. TGA curves of MT and each MT/PEIx-Cu.

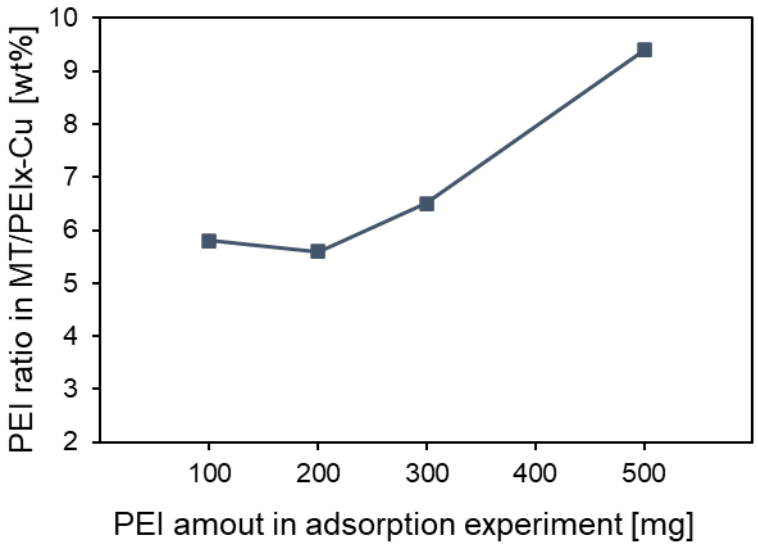

Figure 3-5. Relationship between PEI ratio in MT/PEIx-Cu and PEI amount in adsorption experiment.

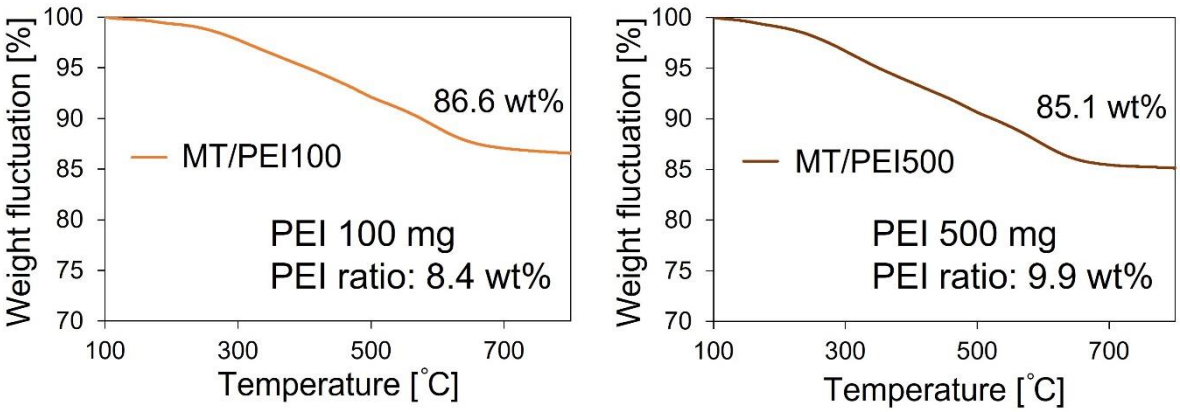

Figure 3-6. TGA curves of the sample without adding Cu^{2+} (only PEI 100 mg (MT/PEI100) and 500 mg (MT/PEI500) conditions).

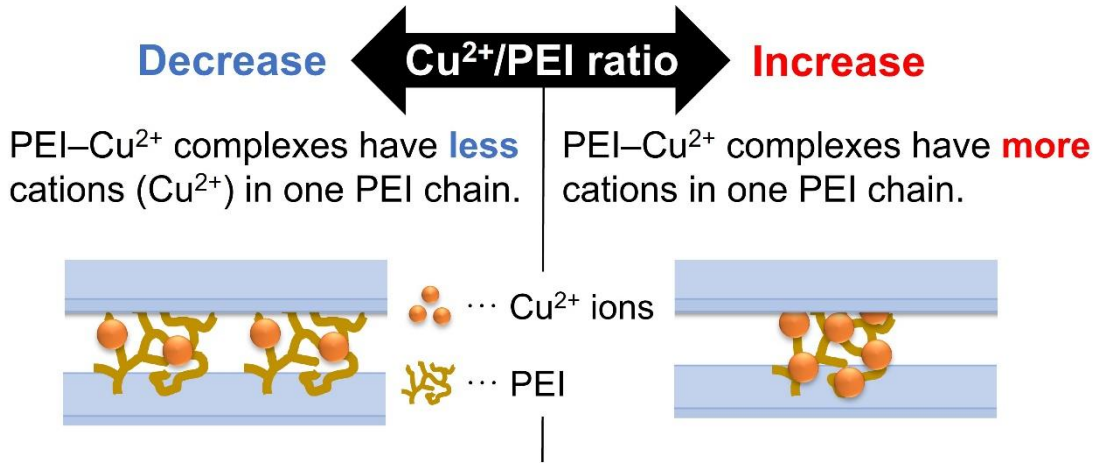

Figure 3-7. Schematic mechanism of the PEI–Cu^{2+} complex adsorption on MT.

Next, MT/PEIx-Cu and the reference compounds were subjected to calcination at 500 °C to convert the Cu^{2+} ions to CuO_x and remove PEI. The crystalline structure of the obtained products (MT/PEIx-Cu 500 °C, MT/Cu 500 °C, and MT 500 °C) was analyzed using powder XRD (Figure 3-8). After heating at 500 °C, the basal spacing profiles that appeared at lower angles before calcination (6.9° in M/Cu and 5.5° in MT/PEI500-Cu; Figure 3-3) disappeared in the XRD patterns of the calcined samples, whereas that at 8.8° was still observed.

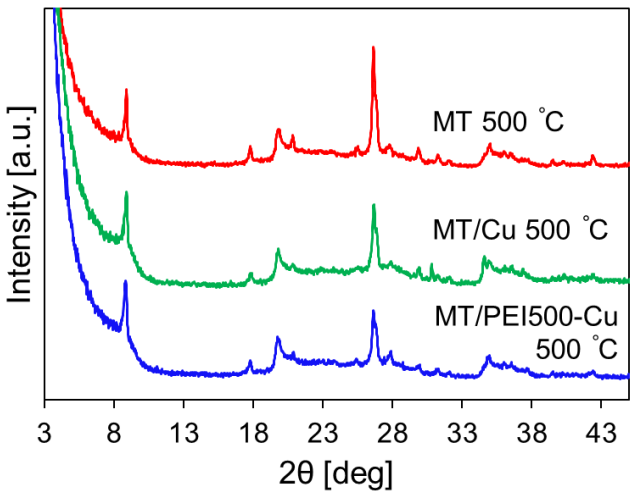

Figure 3-8. XRD patterns of MT 500 °C, MT/Cu 500 °C, and MT/PEI500-Cu 500 °C.

In the FTIR spectrum of MT/PEI500-Cu 500 °C (Figure 3-9), the band derived from PEI (1462 cm^{-1}) disappeared. Further, from survey scans of XPS (Figure 3-10), the peak around N 1s in MT/PEI500-Cu was disappeared after calcination. These changes suggest that the conversion of Cu species and the PEI removal successfully proceeded. However, the band around 2900 cm^{-1} was remained after calcination; this remained peak might be due to the formation of the carbonate minerals.[47,48] Furthermore, while the intensity of Al–OH band (3620 cm^{-1}) in MT/PEI500-Cu 500 °C was decreased compared to that in MT/PEI500-Cu, that intensity in MT 500 °C was relatively close to that in MT (Figure 3-1, 3-9, and 3-11). This difference suggests that the CuO_x supporting process decreased the Al–OH sites and changed the clay structure.

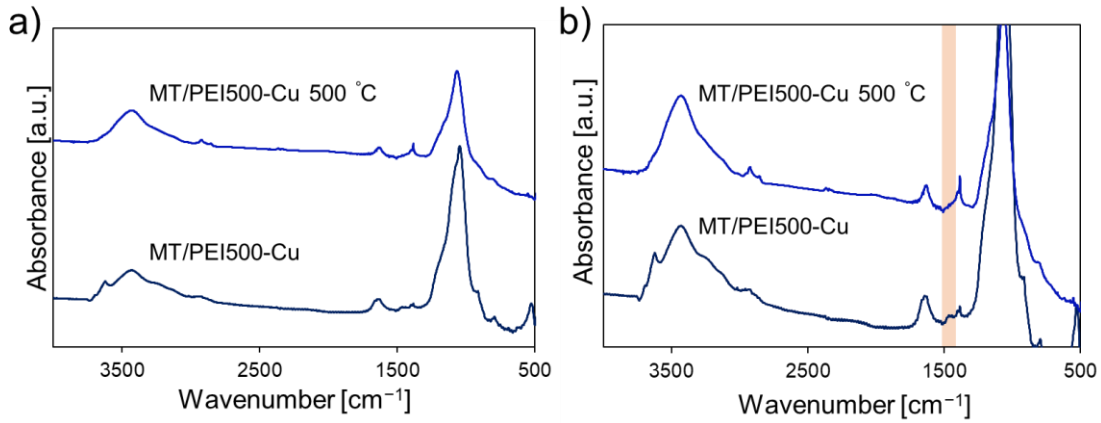

Figure 3-9. a) Wide and b) narrow FTIR spectra of MT/PEI500-Cu and MT/PEI500-Cu 500 °C.

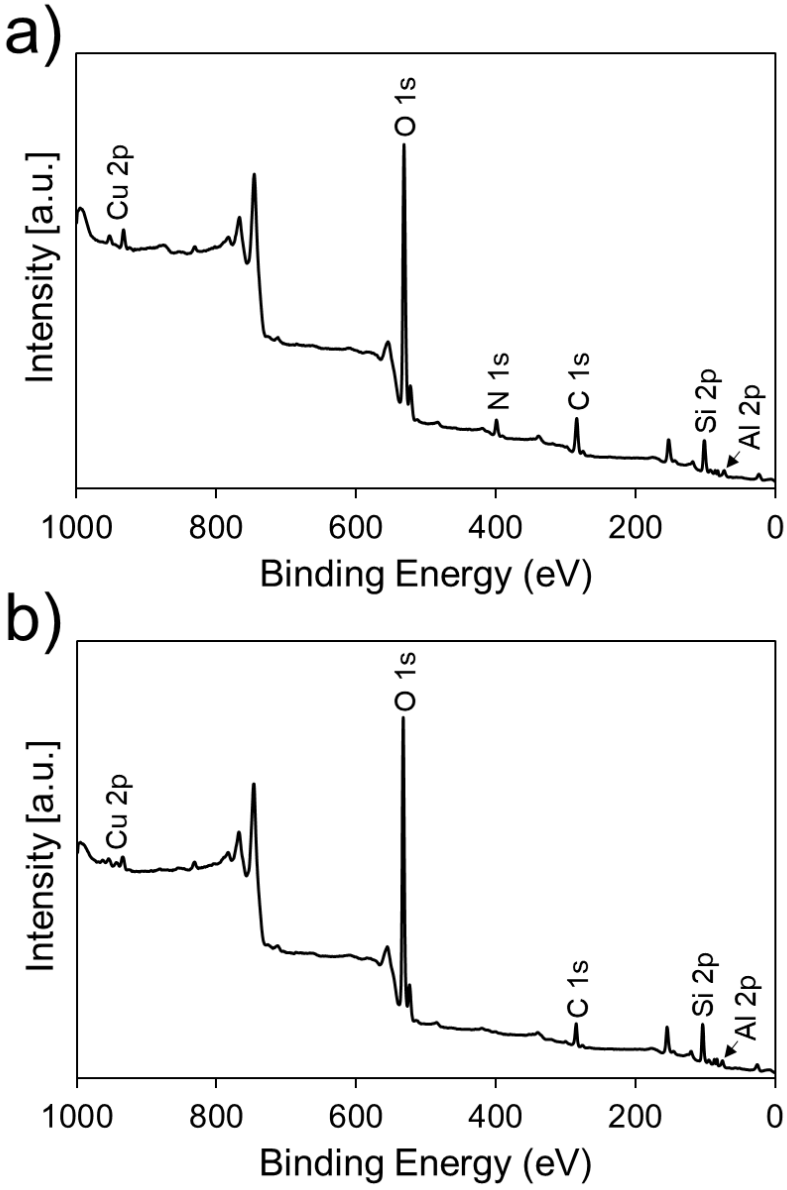

Figure 3-10. XPS survey scans for a) MT/PEI500-Cu and b) MT/PEI500-Cu 500 °C.

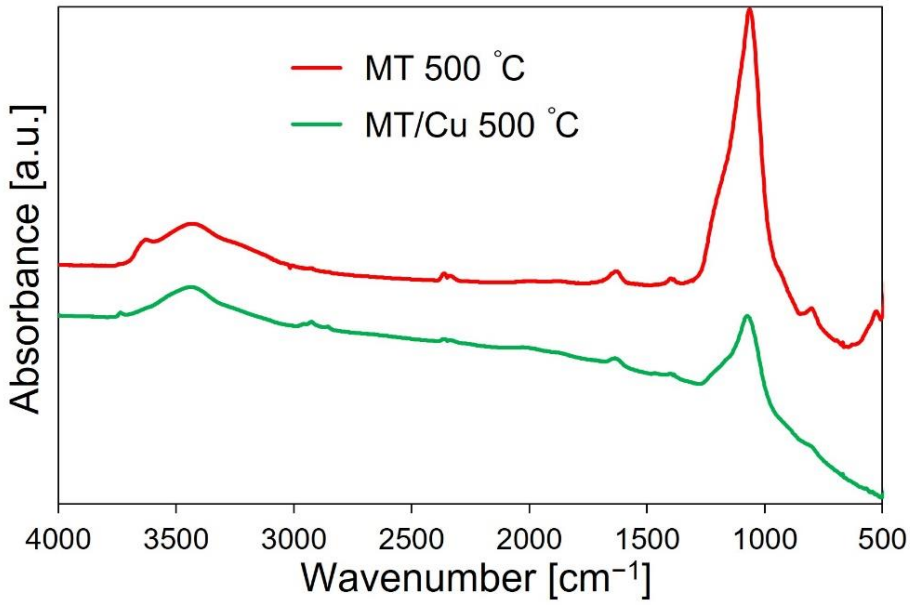

Figure 3-11. FTIR spectra of MT 500 °C and MT/Cu 500 °C.

The conversion of Cu species to CuO_x was also confirmed by heating pristine $Cu(OAc)_2 \cdot H_2O$ at 500 °C for 5 h under an air atmosphere and recording the XRD pattern of the obtained product, in which the typical peaks of CuO were detected (Figure 3-12).[49] In addition, no peaks attributable to CuO_x species (CuO and Cu_2O) were confirmed in the XRD patterns of MT/PEI500-Cu 500 °C and MT/Cu 500 °C (Figure 3-8), suggesting the highly dispersion of CuO_x on the MT carriers or small ratio of CuO_x in each material.[49–52] The chemical state of Cu species was analyzed using XPS. The Cu 2p XPS spectra of MT/PEI500-Cu and MT/PEI500-Cu 500 °C (Figure 3-13) showed bands ascribable to Cu $2p_{3/2}$ (929–939 eV) and Cu $2p_{1/2}$ (948–958 eV). The shake-up bands observed in CuO (Cu^{2+}) appeared at 944 and 964 eV in the Cu 2p XPS spectrum of MT/PEI500-Cu 500 °C, suggesting the conversion of the Cu state.[53,54] In MT/PEI500-Cu, no satellite peaks derived from Cu^{2+} were observed; diamagnetic Cu^{+} compounds do not represent the satellite peaks in contrast to paramagnetic Cu^{2+} compounds, suggesting that a reduction of Cu^{2+} species may be caused by amine in PEI.[55,56] The spectrum of MT/Cu 500 °C was similar to that of MT/PEI500-Cu 500 °C (Figure 3-14).

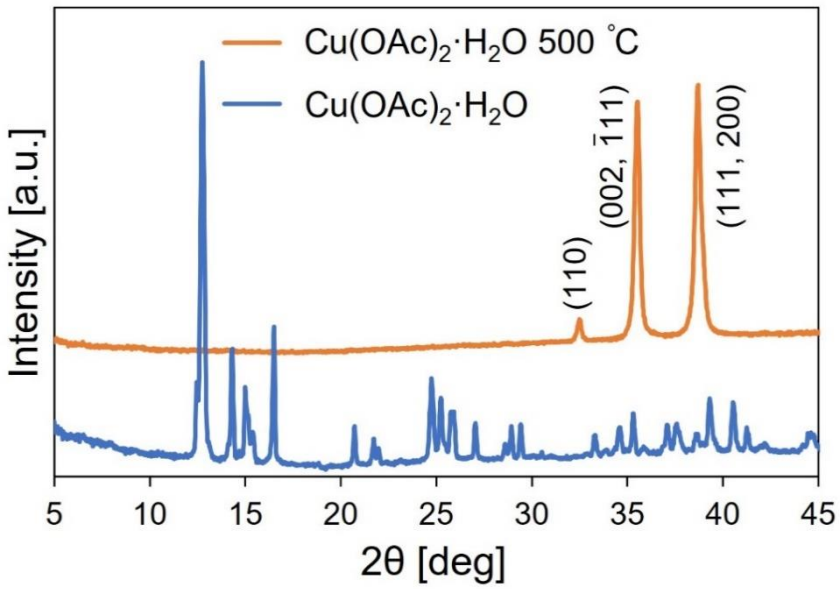

Figure 3-12. XRD patterns of $Cu(OAc)_2 \cdot H_2O$ and $Cu(OAc)_2 \cdot H_2O$ 500 °C, which is prepared with heating $Cu(OAc)_2 \cdot H_2O$ at 500 °C for 5 h (ramping rate: 5 °C min^{-1}).

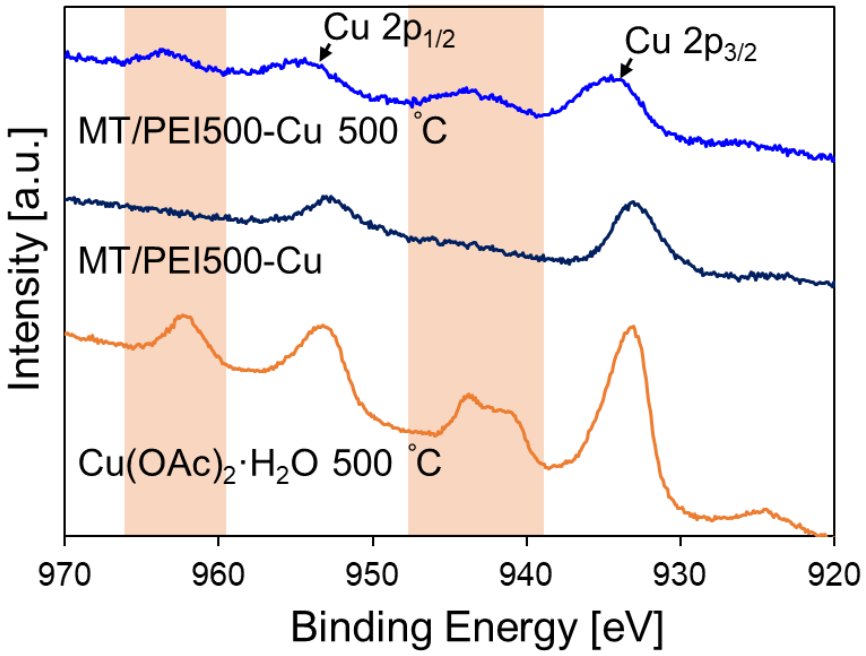

Figure 3-13. High-resolution XPS spectra in the Cu 2p region of $Cu(OAc)_2 \cdot H_2O$ 500 °C, MT/PEI500-Cu, and MT/PEI500-Cu 500 °C.

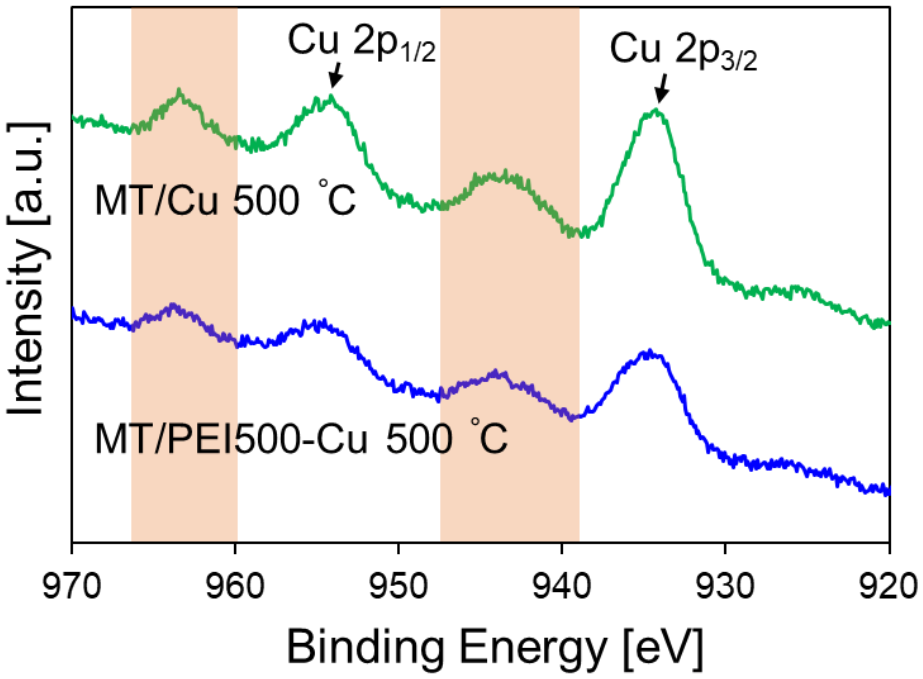

Figure 3-14. High-resolution XPS spectra in the Cu 2p region of MT/PEI500-Cu 500 °C and MT/Cu 500 °C.

The element composition of the materials was analyzed via EDX, and the results are summarized in Table 3-1. The higher actual Cu/Si values of the CuO_x/clay nanocomposites compared with that of MT 500 °C confirms the introduction of Cu. Corrected Cu/Si values of MT/Cu 500 °C and MT/PEI500-Cu 500 °C were 0.051 and 0.027 (at%/at%), respectively. Furthermore, upon altering the PEI amount (Cu^{2+}/PEI ratio), the Cu/Si values of MT/PEI300-Cu 500 °C, MT/PEI200-Cu 500 °C, and MT/PEI100-Cu 500 °C were 0.037, 0.036, and 0.044, respectively. Hence, the Cu ratio in the CuO_x/clay nanocomposites can be tuned by adjusting the PEI amount.

Table 3-1. Element ratios of Si, Al, Cu, and Cu/Si value.

	Al [at%]	**Si** [at%]	**Cu** [at%]	***Cu/Si^{A}** [-]	****Cu/Si^{C}** [-]
MT 500 °C	22.8 ± 3.3	75.3 ± 3.4	1.9 ± 0.5	0.025	—
MT/Cu 500 °C	19.2 ± 2.2	75.1 ± 2.0	5.7 ± 0.8	0.076	0.051
MT/PEI100-Cu 500 °C	20.0 ± 1.9	74.9 ± 1.8	5.2 ± 0.5	0.069	0.044
MT/PEI200-Cu 500 °C	20.8 ± 2.5	74.6 ± 2.3	4.6 ± 0.6	0.061	0.036
M/TPEI300-Cu 500 °C	20.5 ± 3.7	74.9 ± 3.0	4.6 ± 0.9	0.062	0.037
MT/PEI500-Cu 500 °C	18.4 ± 2.8	77.5 ± 2.7	4.0 ± 0.8	0.052	0.027

*The actual value of Cu/Si obtained by dividing the element ratio of Cu by the element ratio of Si

**The corrected value of Cu/Si obtained by subtracting the Cu/Si^{A} value of MT 500 °C from each Cu/Si^{A} value of CuO_x/clay nanocomposites

The morphology of the samples was observed with SEM and TEM. The SEM images shown in Figure 3-15 display the overall morphology of the samples. MT 500 °C and MT/PEI500-Cu 500 °C exhibited a plate-like structure without any significant difference between both samples. Furthermore, the CuO_x morphology on MT were observed using TEM. According to the TEM images (Figure 3-16), the particle size of CuO_x in MT/PEI500-Cu 500 °C was smaller than that in MT/PEI100-Cu 500 °C; the CuO_x in MT/PEI500-Cu 500 °C was highly dispersed. The average particle sizes observed on clay with this TEM (n = 5) were 13.7 nm in MT/PEI500-Cu 500 °C

and 29.4 nm in MT/PEI100-Cu 500 °C, respectively. Further, the large particle (>35 nm) observed in MT/PEI100-Cu 500 °C were not confirmed in MT/PEI500-Cu 500 °C, suggesting that CuO_x nanoparticles in MT/PEI100-Cu 500 °C had larger size than those of MT/PEI500-Cu 500 °C. This particle size and dispersibility differences may be due to the number of Cu^{2+} ions per PEI molecule in PEI–Cu^{2+} complex and introduced amounts of PEI (PEI–Cu^{2+} complex) in MT/PEIx-Cu. As shown in Table 3-2, the number of Cu^{2+} ions per PEI molecule in MT/PEI100-Cu 500 °C, MT/PEI200-Cu 500 °C, and MT/PEI500-Cu 500 °C was 9.44, 4.72, and 1.89 mol mol^{-1}, respectively. Assuming that the number of Cu^{2+} ions per PEI affects the particle size of the CuO_x, the particle size of CuO_x on the MT surface might change by altering the Cu^{2+}/PEI ratio. Upon changing the PEI content introduced as PEI–Cu^{2+} complex in MT/PEIx-Cu, the dispersibility of CuO_x on the MT surface would also change (Figure 3-17). However, in dispersibility, it is necessary to consider the CuO_x falling from MT (Figure 3-18).

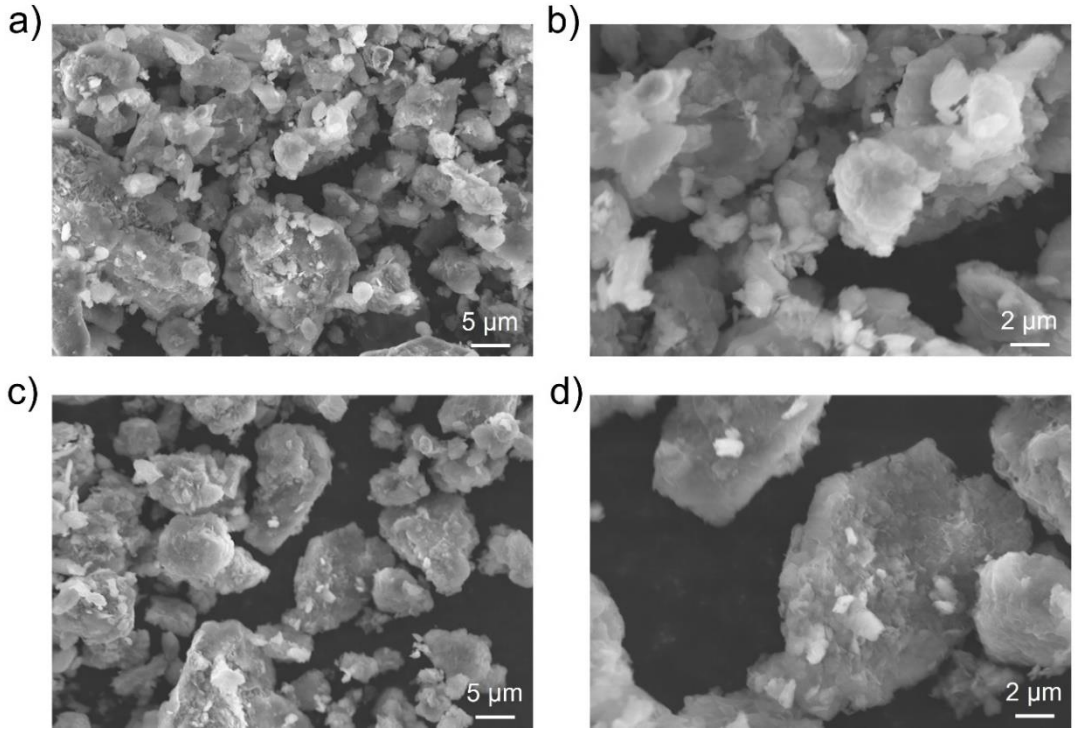

Figure 3-15. SEM images of MT 500 °C (a, b) and MT/PEI500-Cu 500 °C (c, d).

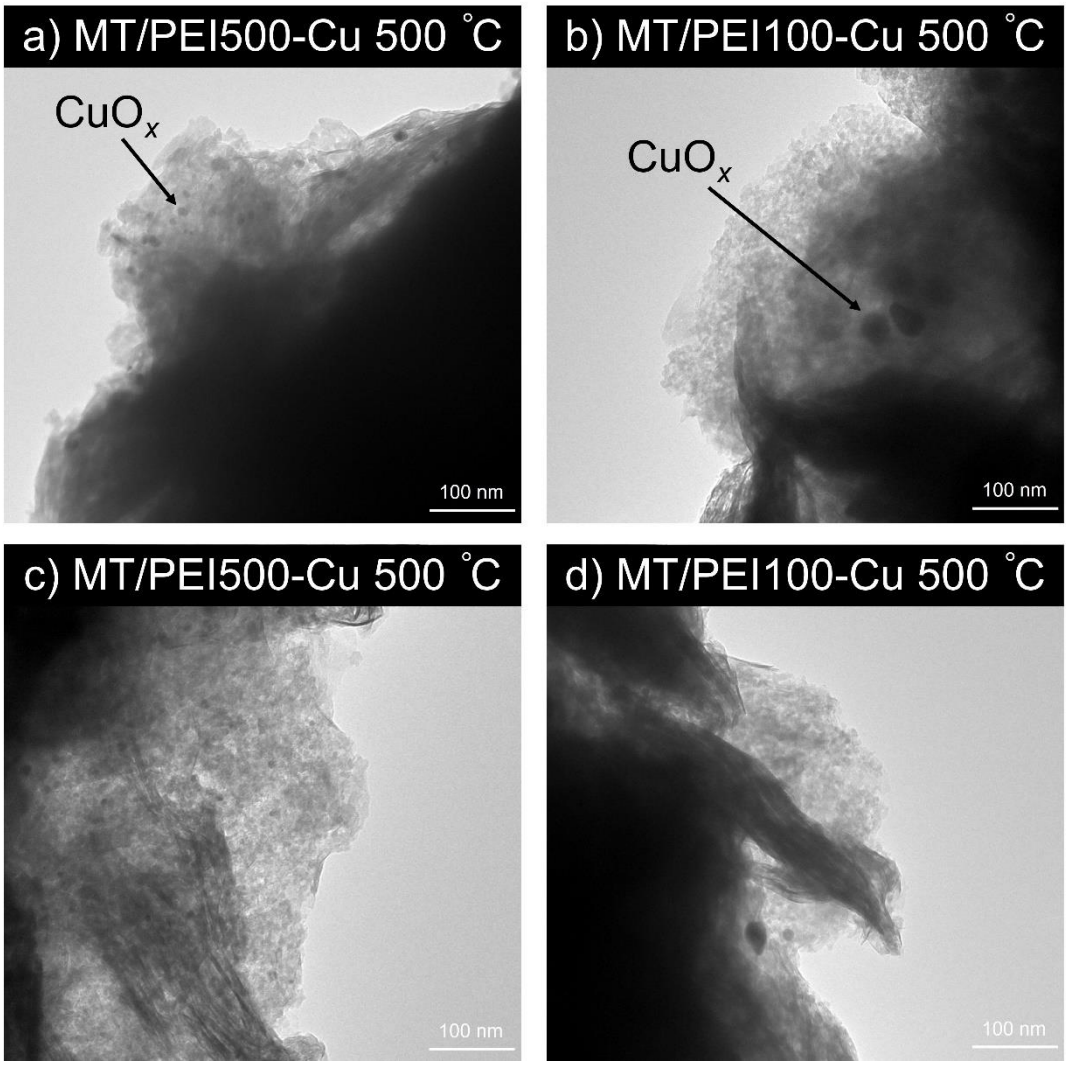

Figure 3-16. TEM images of MT/PEI500-Cu 500 °C (a, c) and MT/PEI100-Cu 500 °C (b, d).

Table 3-2. Calculation results of Cu^{2+} ions per PEI (mol mol^{-1}).

Entry	Cu^{2+} ions [mmol]	PEI [mmol]	Cu^{2+} ions per PEI [mol mol^{-1}]
MT/PEI100-Cu 500 °C		0.167	9.44
MT/PEI200-Cu 500 °C	1.57	0.333	4.72
MT/PEI500-Cu 500 °C		0.833	1.89

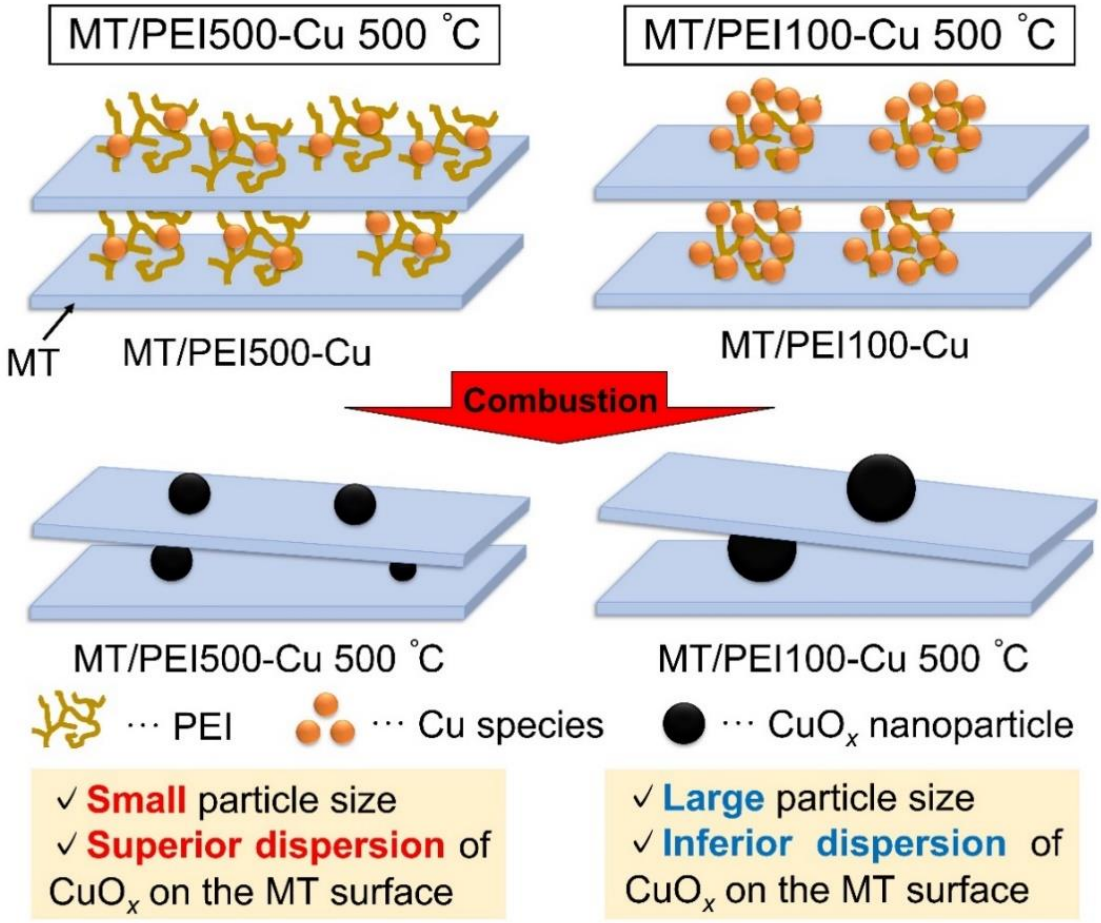

Figure 3-17. Schematic diagram of the CuO_x nanoparticles formation on the MT surface upon changing the Cu^{2+}/PEI ratios.

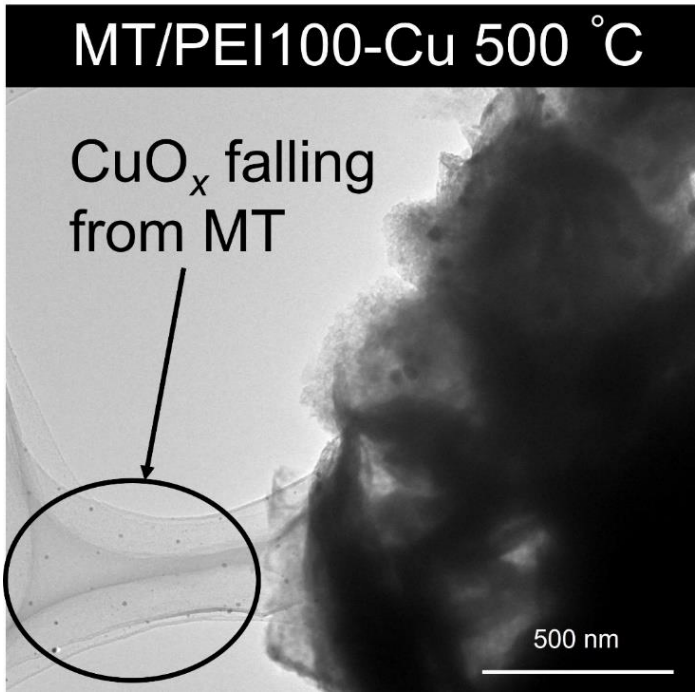

Figure 3-18. TEM image of MT/PEI100-Cu 500 °C.

The porous structure was investigated using N_2 adsorption–desorption tests, and the results are shown in Figure 3-19. All materials exhibited type IV isotherm, which indicates the present of mesopores, and hysteresis loops of type H3, which are in accord with the presence of plate-like particles.[57–59] The S_{BET} and V_{total} values are presented in Table 3-3. The S_{BET} and V_{total} of MT 500 °C were similar to those of MT, indicating no major change in porosity upon calcination. After introduced the CuO_x, in MT/Cu 500 °C and MT/PEIx-Cu 500 °C, the S_{BET} and V_{total} values were also relatively close to MT and MT 500 °C, suggesting that these CuO_x supporting methods retained the S_{BET} and V_{total} before supporting. Next, the pore structure was analyzed by determining the pore size distributions using the BJH method. The pore size distributions of MT/PEIx-Cu 500 °C were similar (Figure 3-20). MT/PEIx-Cu 500 °C had a pore size distribution close to MT 500 °C (Figure 3-20). According to the N_2 adsorption–desorption tests, these methods of CuO_x supporting retained the porous structure of MT and MT 500 °C.

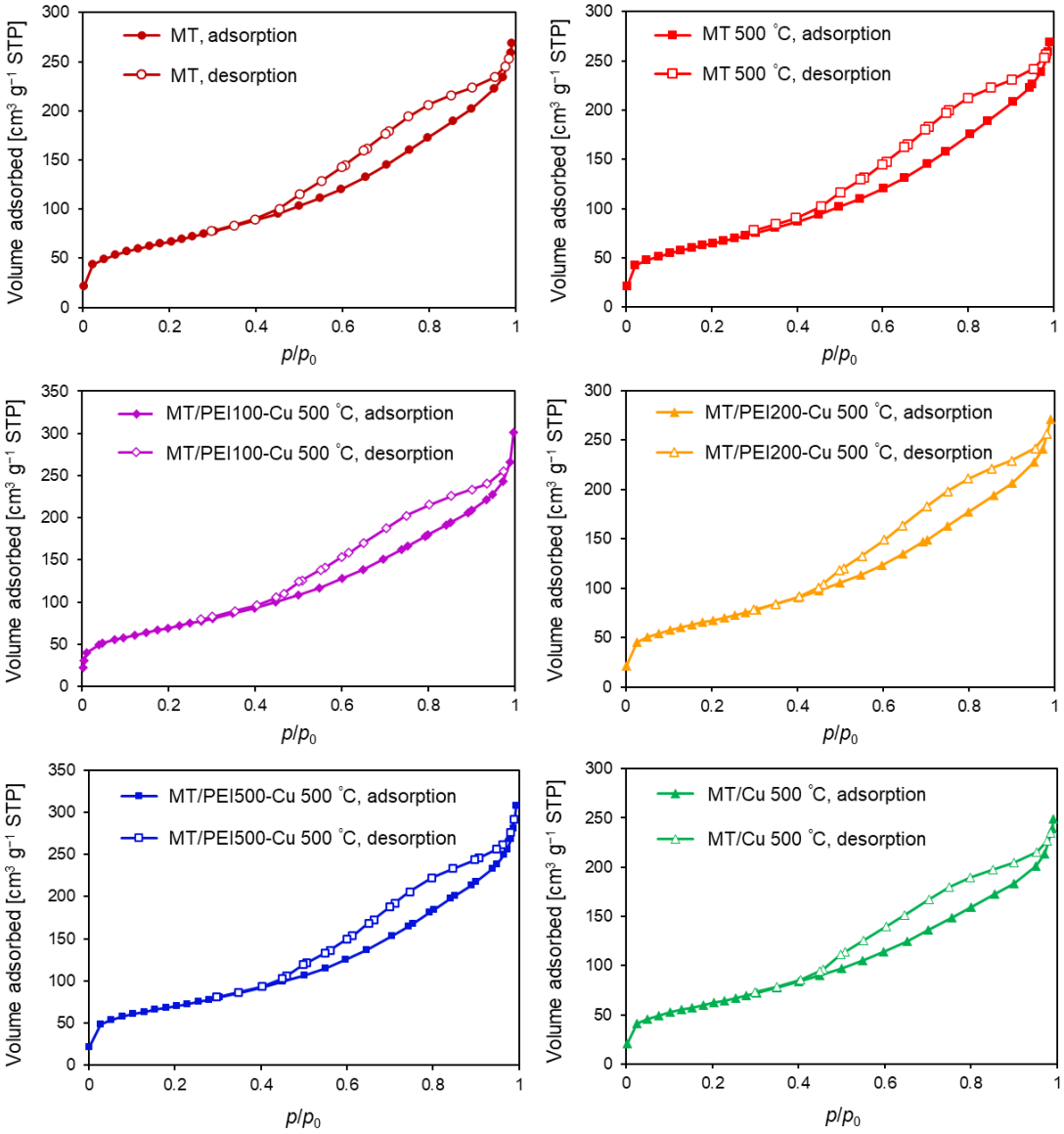

Figure 3-19. N_2 adsorption–desorption isotherms of MT, MT 500 °C, MT/PEI100-Cu 500 °C, MT/PEI200-Cu 500 °C, and MT/Cu 500 °C.

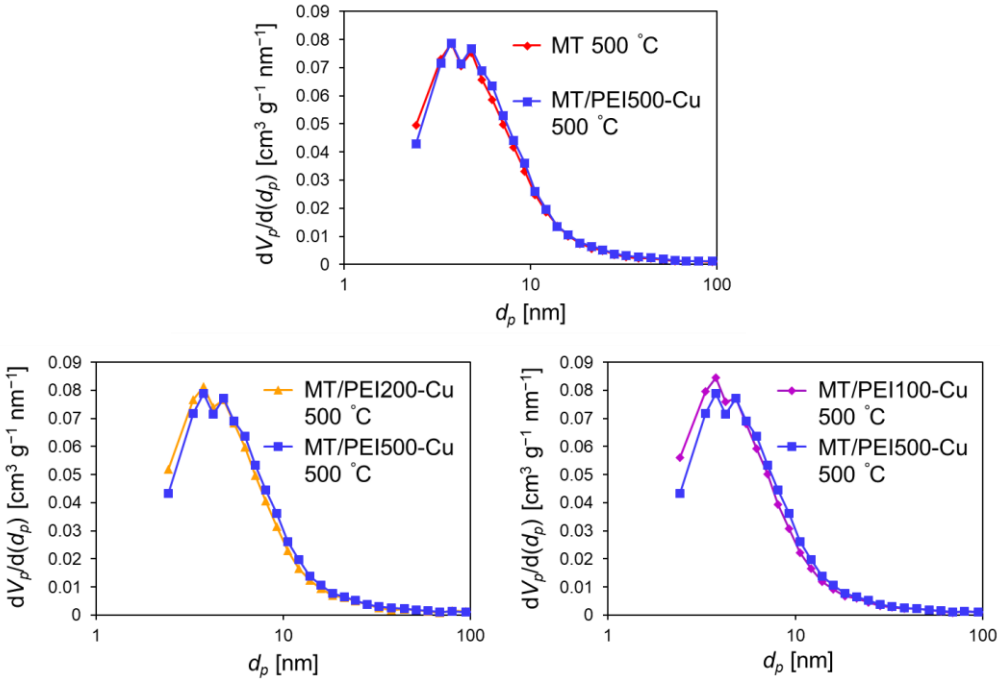

Figure 3-20. BJH pore size distributions of MT 500 °C, MT/PEI100-Cu 500 °C, MT/PEI200-Cu 500 °C, and MT/PEI500-Cu 500 °C.

Table 3-3. S_{BET} and V_{total} of each material.

Entry	S_{BET} [$m^2\ g^{-1}$]	V_{total} [$cm^3\ g^{-1}$]
MT	240	0.403
MT 500 °C	235	0.412
MT/Cu 500 °C	225	0.377
MT/PEI100-Cu 500 °C	252	0.418
MT/PEI200-Cu 500 °C	244	0.418
MT/PEI500-Cu 500 °C	247	0.451

This method for supporting metal oxides on clay nanosheets using polymer templates is expected to be applicable to different metal (Co, Ni, Zn, etc.) species, other polymers capable of forming complexes with metals, and other porous carriers (e.g., mesoporous silica).

3-1-3-2. CO_2 adsorption performance

CO_2 adsorption tests were conducted at 303 K, and the resulting isotherms are shown in Figure 3-21, 3-22, and 3-23. The CO_2 uptakes at 1 bar of MT/PEI100-Cu 500 °C, MT/PEI200-Cu 500 °C, and MT/PEI500-Cu 500 °C were 0.330, 0.351, and 0.404 mmol g^{-1}, respectively (Figure 3-21). Whereas the CuO_x loading was increased, the CO_2 uptakes of MT/PEIx-Cu 500 °C decreased as the value of x decreased. The uptake differences were most likely due to the supported state differences of CuO_x in the nanocomposites. The Cu 2p XPS spectra of MT/PEI100-Cu 500 °C and MT/PEI500-Cu 500 °C (Figure 3-24) were similar, suggesting that CuO_x was present in both nanocomposites in the similar chemical states. The adsorption property of metal nanoparticles for CO_2 and CO is known to be changed by the metal nanoparticle size.[60,61] Furthermore, there is the paper considering that the dispersibility of metal oxides on the carrier affected the CO_2 adsorption characteristics due to the changes of the possible number of CO_2 adsorption sites.[1] In Figure 3-16, the CuO_x particle sizes and dispersibilities between MT/PEI100-Cu 500 °C and MT/PEI500-Cu 500 °C were different; the CuO_x nanoparticles in MT/PEI500-Cu 500 °C were smaller compared with that in MT/PEI100-Cu 500 °C, and CuO_x in MT/PEI500-Cu 500 °C was highly dispersed in the state of observation. Hence, these particle size and dispersibility changes might affect the CO_2 adsorption properties of MT/PEIx-Cu 500 °C. As shown in Figure 3-22, the CO_2 uptake of MT/PEI500-Cu 500 °C was about 13% and 3340% higher than that of MT 500 °C (0.356 mmol g^{-1}) and $Cu(OAc)_2 \cdot H_2O$ 500 °C (CuO, 0.012 mmol g^{-1}), respectively. The CO_2 uptake increase upon loading CuO_x on MT might be due to an increase in the CO_2 affinity as a result of the acid–base interaction between CuO_x species and CO_2, and the porosity improvement of CuO_x species.[1] This enhancement in the CO_2 uptake suggests that the present method for supporting CuO_x affords an effective surface and porous structure for CO_2 capture. In comparison with MT 500 °C, MT/PEI100-Cu 500 °C and MT/PEI200-Cu 500 °C had the lower CO_2

adsorption capacity; this decrease may be due to the structural change of MT (e.g., the decrease of Al–OH sites) during CuO_x supporting, which confirmed with FTIR spectra (Figure 3-1, 3-9, and 3-11). Further, the CO_2 uptake of MT/Cu 500 °C (0.399 mmol g^{-1}, Figure 3-23) was higher than that of MT/PEI100-Cu 500 °C (0.330 mmol g^{-1}) having a similar CuO_x loading, which may be due to differences in the CuO_x particle size and dispersion. Thus, the method for CuO_x supporting affects the CO_2 adsorption properties of the CuO_x/clay nanocomposites.

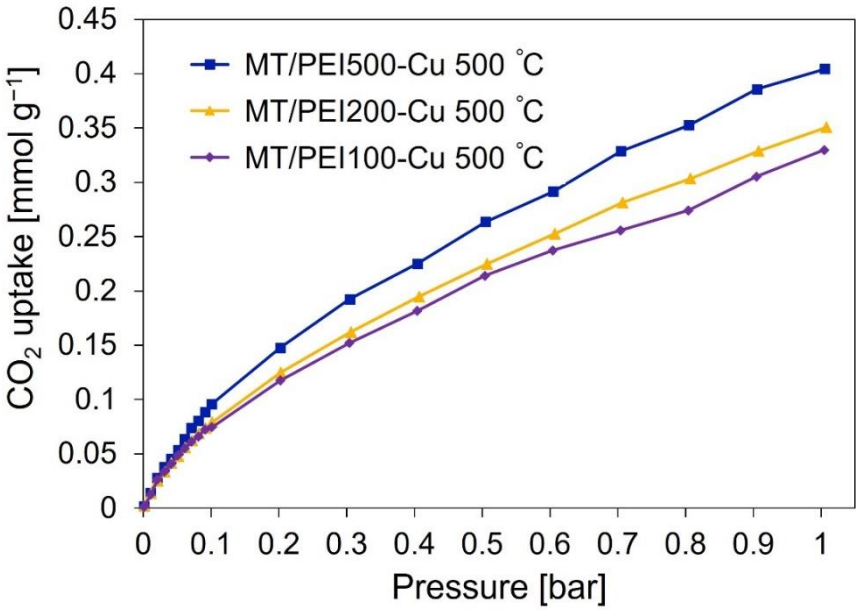

Figure 3-21. CO_2 adsorption isotherms of MT/PEI100-Cu 500 °C, MT/PEI200-Cu 500 °C, and MT/PEI500-Cu 500 °C.

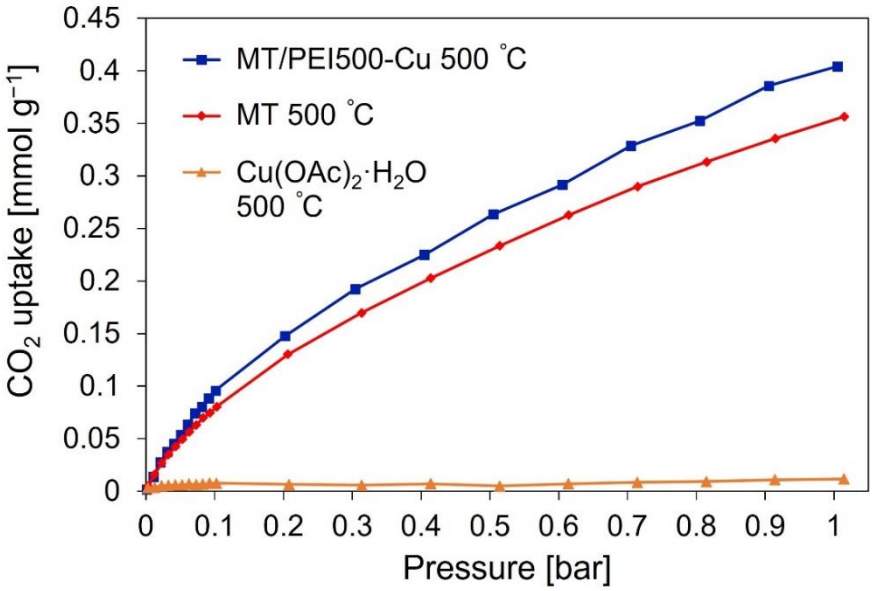

Figure 3-22. CO_2 adsorption isotherms of $Cu(OAc)_2 \cdot H_2O$ 500 °C, MT 500 °C, and MT/PEI500-Cu 500 °C.

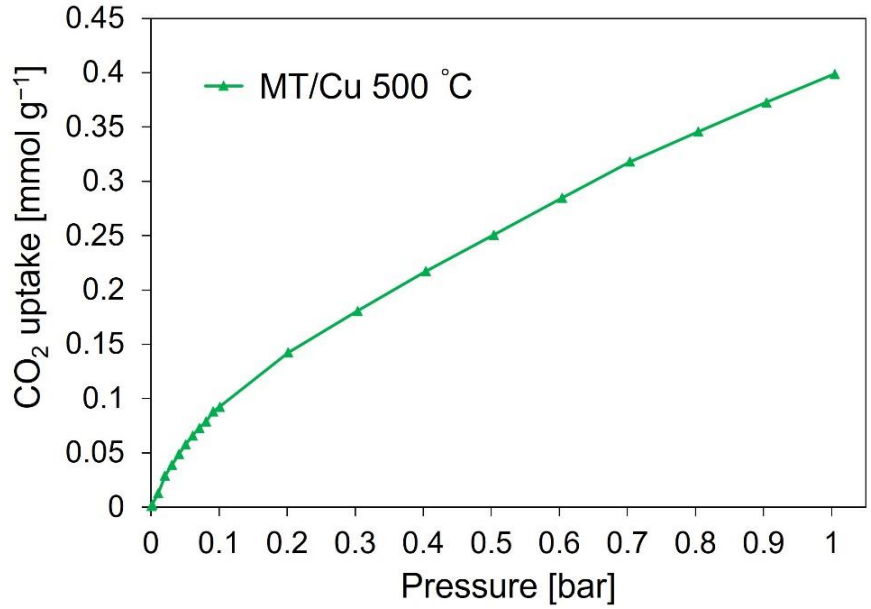

Figure 3-23. CO_2 adsorption isotherm of MT/Cu 500 °C.

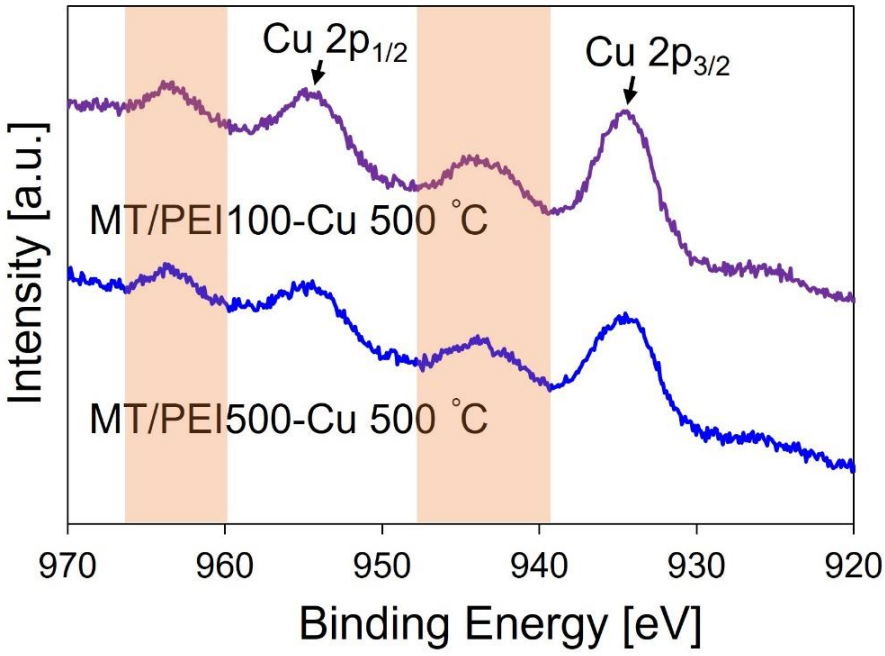

Figure 3-24. High-resolution XPS spectra in the Cu 2p region of MT/PEI100-Cu 500 °C and MT/PEI500-Cu 500 °C.

3-1-4. Conclusion

In summary, a soft-template method for supporting CuO_x on activated clay nanosheets were developed using PEI as the template. The introduced amount of PEI–Cu^{2+} complex and the CuO_x loading on the clay nanosheets depended on the states of the PEI–Cu^{2+} complex, and charge neutralization played an important role in intercalating the PEI–Cu^{2+} complexes between the clay nanosheets. Upon changing the Cu^{2+}/PEI ratio in PEI–Cu^{2+} complex, the CuO_x states formed on activated clay such as partice size can be controlled due to the changes of introduced PEI–Cu^{2+} complex (PEI) amounts and the the number of Cu^{2+} ions per PEI molecule. The CuO_x supporting method developed in the current study provided that constructed CuO_x/clay nanocomposites preserved the porosity of clay. Furthermore, the CO_2 uptake of MT/PEI500-Cu 500 °C was higher than that of MT 500 °C, suggesting that the present method provides a superior surface structure for CO_2 adsorption. Thus, this study offers new insights into the fabrication of metal oxide-supported porous (nanoporous) materials with potential application in diverse fields, such as adsorption/separation, energy devices, and catalysts. Further development of this research content

(CuO_x formation control), such as precise control of particle size and valence state of CuO_x, will contribute to the development of materials science (e.g., synthesis of high-performance catalytic materials).

3-1-5. References

(1) Boruban, C.; Esenturk, E. N. Activated Carbon-Supported CuO Nanoparticles: A Hybrid Material for Carbon Dioxide Adsorption. *J. Nanopart. Res.* **2018**, *20*, 59.

(2) Yang, Y.; Zhao, S.; Bi, F.; Chen, J.; Li, Y.; Cui, L.; Xu, J.; Zhang, X. Oxygen-Vacancy-Induced O_2 Activation and Electron-Hole Migration Enhance Photothermal Catalytic Toluene Oxidation. *Cell Rep. Phys. Sci.* **2022**, *3*, 101011.

(3) Zhang, X.; Zhao, Z.; Zhao, S.; Xiang, S.; Gao, W.; Wang, L.; Xu, J.; Wang, Y. The Promoting Effect of Alkali Metal and H_2O on Mn-MOF Derivatives for Toluene Oxidation: A Combined Experimental and Theoretical Investigation. *J. Catal.* **2022**, *415*, 218–235.

(4) Yang, Y.; Dong, H.; Wang, Y.; Wang, Y.; Liu, N.; Wang, D.; Zhang, X. A Facile Synthesis for Porous CuO/Cu_2O Composites Derived from MOFs and Their Superior Catalytic Performance for CO Oxidation. *Inorg. Chem. Commun.* **2017**, *86*, 74–77.

(5) Bi, F.; Zhao, Z.; Yang, Y.; Gao, W.; Liu, N.; Huang, Y.; Zhang, X. Chlorine-Coordinated Pd Single Atom Enhanced the Chlorine Resistance for Volatile Organic Compound Degradation: Mechanism Study. *Environ. Sci. Technol.* **2022**, *56*, 17321–17330.

(6) Wang, Z.; Zhou, L.; Lou, X. W. Metal Oxide Hollow Nanostructures for Lithium-ion Batteries. *Adv. Mater.* **2012**, *24*, 1903–1911.

(7) Smith, R. D. L.; Prévot, M. S.; Fagan, R. D.; Zhang, Z.; Sedach, P. A.; Siu, M. K. J.; Trudel, S.; Berlinguette, C. P. Photochemical Route for Accessing Amorphous Metal Oxide Materials for Water Oxidation Catalysis. *Science* **2013**, *340*, 60–63.

(8) Feng, B.; An, H.; Tan, E. Screening of CO_2 Adsorbing Materials for Zero Emission Power Generation Systems. *Energy Fuels* **2007**, *21*, 426–434.

(9) Jiao, F.; Frei, H. Nanostructured Cobalt Oxide Clusters in Mesoporous Silica as Efficient Oxygen-Evolving Catalysts. *Angew. Chem.* **2009**, *121*, 1873–1876.

(10) Jiang, H.; Ma, J.; Li, C. Mesoporous Carbon Incorporated Metal Oxide Nanomaterials as Supercapacitor Electrodes. *Adv. Mater.* **2012**, *24*, 4197–4202.

(11) Das, T.; Chatterjee, R.; Majee, A.; Uyama, H.; Morgan, D.; Nandi, M. *In Situ* Synthesis of CuO Nanoparticles over Functionalized Mesoporous Silica and Their Application in

Catalytic Syntheses of Symmetrical Diselenides. *Dalton Trans.* **2019**, *48*, 17874–17886.

(12) Li, M.; Huang, K.; Schott, J. A.; Wu, Z.; Dai, S. Effect of Metal Oxides Modification on CO_2 Adsorption Performance over Mesoporous Carbon. *Microporous Mesoporous Mater.* **2017**, *249*, 34–41.

(13) Lakhi, K. S.; Singh, G.; Kim, S.; Baskar, A. V.; Joseph, S.; Yang, J.-H.; Ilbeygi, H.; Ruban, S. J. M.; Vu, V. T. H.; Vinu, A. Mesoporous Cu-SBA-15 with Highly Ordered Porous Structure and Its Excellent CO_2 Adsorption Capacity. *Microporous Mesoporous Mater.* **2018**, *267*, 134–141.

(14) Fishman, Z. S.; Rudshteyn, B.; He, Y.; Liu, B.; Chaudhuri, S.; Askerka, M.; Haller, G. L.; Batista, V. S.; Pfefferle, L. D. Fundamental Role of Oxygen Stoichiometry in Controlling the Band Gap and Reactivity of Cupric Oxide Nanosheets. *J. Am. Chem. Soc.* **2016**, *138*, 10978–10985.

(15) Wang, F.; Xiao, L.; Chen, J.; Chen, L.; Fang, R.; Li, Y. Regulating the Electronic Structure and Water Adsorption Capability by Constructing Carbon-Doped CuO Hollow Spheres for Efficient Photocatalytic Hydrogen Evolution. *ChemSusChem* **2020**, *13*, 5711–5721.

(16) Xu, X.; Yang, H.; Liu, Y. Self-Assembled Structures of CuO Primary Crystals Synthesized from $Cu(CH_3COO)_2$–NaOH Aqueous Systems. *CrystEngComm* **2012**, *14*, 5289–5298.

(17) Isahak, W. N. R. W.; Ramli, Z. A. C.; Samad, W. Z.; Yarmo, M. A. Capturing Greenhouse Gas Carbon Dioxide to Form Carbonate Compounds. *J. Teknol.* **2015**, *77*, 105–114.

(18) Patel, A.; Rufford, T. E.; Rudolph, V.; Zhu, Z. Selective Catalytic Reduction of NO by CO over CuO Supported on SBA-15: Effect of CuO Loading on the Activity of Catalysts. *Catal. Today* **2011**, *166*, 188–193.

(19) Zhang, J.; Liu, J.; Peng, Q.; Wang, X.; Li, Y. Nearly Monodisperse Cu_2O and CuO Nanospheres: Preparation and Applications for Sensitive Gas Sensors. *Chem. Mater.* **2006**, *18*, 867–871.

(20) Zhang, X.; Wang, G.; Liu, X.; Wu, J.; Li, M.; Gu, J.; Liu, H.; Fang, B. Different CuO

Nanostructures: Synthesis, Characterization, and Applications for Glucose Sensors. *J. Phys. Chem. C* **2008**, *112*, 16845–16849.

(21) Ko, S.; Lee, J.-I.; Yang, H. S.; Park, S.; Jeong, U. Mesoporous CuO Particles Threaded with CNTs for High-Performance Lithium-Ion Battery Anodes. *Adv. Mater.* **2012**, *24*, 4451–4456.

(22) Aher, R. D.; Gade, M. H.; Reddy, R. S.; Sudalai, A. Cu^{II}-Exchanged Montmorillonite K10 Clay-Catalyzed Direct Carboxylation of Terminal Alkynes with Carbon Dioxide. *Indian J. Chem.* **2012**, *51A*, 1325–1329.

(23) Cao, J.-L.; Shao, G.-S.; Wang, Y.; Liu, Y.; Yuan, Z.-Y. CuO Catalysts Supported on Attapulgite Clay for Low-Temperature CO Oxidation. *Catal. Commun.* **2008**, *9*, 2555–2559.

(24) Borah, B. J.; Dutta, D.; Saikia, P. P.; Barua, N. C.; Dutta, D. K. Stabilization of Cu(0)-Nanoparticles into the Nanopores of Modified Montmorillonite: An Implication on the Catalytic Approach for "Click" Reaction between Azides and Terminal Alkynes. *Green Chem.* **2011**, *13*, 3453–3460.

(25) Bagchi, B.; Kar, S.; Dey, S. K.; Bhandary, S.; Roy, D.; Mukhopadhyay, T. K.; Das, S.; Nandy, P. In Situ Synthesis and Antibacterial Activity of Copper Nanoparticle Loaded Natural Montmorillonite Clay Based on Contact Inhibition and Ion Release. *Colloids Surf. B Biointerfaces* **2013**, *108*, 358–365.

(26) Ghashghaee, M.; Shirvani, S.; Farzaneh, V.; Sadjadi, S. Hydrotalcite-Impregnated Copper and Chromium-Doped Copper as Novel and Efficient Catalysts for Vapor-Phase Hydrogenation of Furfural: Effect of Clay Pretreatment. *Braz. J. Chem. Eng.* **2018**, *35*, 669–678.

(27) Lee, D.; Char, K.; Lee, S. W.; Park, Y. W. Structural Changes of Polyaniline/Montmorillonite Nanocomposites and Their Effects on Physical Properties. *J. Mater. Chem.* **2003**, *13*, 2942–2947.

(28) Darder, M.; Colilla, M.; Ruiz-Hitzky, E. Biopolymer−Clay Nanocomposites Based on Chitosan Intercalated in Montmorillonite. *Chem. Mater.* **2003**, *15*, 3774–3780.

(29) Starodubtsev, S. G.; Lavrentyeva, E. K.; Shtykova, E. V.; Dembo, K. A.; Volkov, V. V.

Montmorillonite–Polycation Multilayers Incorporated in Polyacrylamide. *Appl. Clay Sci.* **2009**, *46*, 88–94.

(30) Öztekin, N.; Alemdar, A.; Güngör, N.; Erim, F. B. Adsorption of Polyethyleneimine from Aqueous Solutions on Bentonite Clays. *Mater. Lett.* **2002**, *55*, 73–76.

(31) Molnár, Á. The Use of Chitosan-Based Metal Catalysts in Organic Transformations. *Coord. Chem. Rev.* **2019**, *388*, 126–171.

(32) Chen, Y.; Yang, S.; Zhang, T.; Xu, M.; Zhao, J.; Zeng, M.; Sun, K.; Feng, R.; Yang, Z.; Zhang, P.; Wang, B.; Cao, X. Positron Annihilation Study of Chitosan and Its Derived Carbon/Pillared Montmorillonite Clay Stabilized Pd Species Nanocomposites. *Polym. Test.* **2022**, *114*, 107689.

(33) Stevanović, G.; Jović-Jovičić, N.; Krstić, J.; Milutinović-Nikolić, A.; Banković, P.; Popović, A.; Ajduković, M. Nanocomposite Co-Catalysts, Based on Smectite and Biowaste-Derived Carbon, as Peroxymonosulfate Activators in Degradation of Tartrazine. *Appl. Clay Sci.* **2022**, *230*, 106718.

(34) Kalidhasan, S.; Dror, I.; Berkowitz, B. Atrazine Degradation through PEI-Copper Nanoparticles Deposited onto Montmorillonite and Sand. *Sci. Rep.* **2017**, *7*, 1415.

(35) Chen, C.-C.; Kuo, P.-L. Gold Nanoparticles Prepared Using Polyethylenimine Adsorbed onto Montmorillonite. *J. Colloid Interface Sci.* **2006**, *293*, 101–107.

(36) Wang, Q.; Zhang, Y.; Zhou, Y.; Zhang, Z.; Xu, Y.; Zhang, C.; Sheng, X. Synthesis of Dendrimer-Templated Pt Nanoparticles Immobilized on Mesoporous Alumina for *p*-Nitrophenol Reduction. *New J. Chem.* **2015**, *39*, 9942–9950.

(37) Mohamed, Z.; Abdelkarim, A.; Ziat, K.; Mohamed, S. Adsorption of Cu(II) onto Natural Clay: Equilibrium and Thermodynamic Studies. *J. Mater. Environ. Sci.* **2016**, *7*, 566–570.

(38) Ravindra Reddy, T.; Kaneko, S.; Endo, T.; Lakshmi Reddy, S. Spectroscopic Characterization of Bentonite. *J. Lasers Opt. Photonics* **2017**, *4*, 171.

(39) Nayak, P. S.; Singh, B. K. Instrumental Characterization of Clay by XRF, XRD and FTIR. *Bull. Mater. Sci.* **2007**, *30*, 235–238.

(40) Navrátilová, Z.; Wojtowicz, P.; Vaculíková, L.; Šugárková, V. Sorption of

Alkylammonium Cations on Montmorillonite. *Acta Geodyn. Geomater.* **2007**, *4*, 59–65.

(41) Santha Moorthy, M.; Bharathiraja, S.; Manivasagan, P.; Lee, K. D.; Oh, J. Synthesis of Surface Capped Mesoporous Silica Nanoparticles for pH-Stimuli Responsive Drug Delivery Applications. *Med. Chem. Commun.* **2017**, *8*, 1797–1805.

(42) Demir, F.; Demir, B.; Yalcinkaya, E. E.; Cevik, S.; Odaci Demirkol, D.; Anik, U.; Timur, S. Amino Acid Intercalated Montmorillonite: Electrochemical Biosensing Applications. *RSC Adv.* **2014**, *4*, 50107–50113.

(43) Typical IR Absorption Frequencies For Common Functional Groups. Available online: https://www.niu.edu/clas/chembio/research/analytical-lab/ftir/ir-frequencies-table.shtml (accessed on 6 April 2023).

(44) Kooli, F.; Khimyak, Y. Z.; Alshahateet, S. F.; Chen, F. Effect of the Acid Activation Levels of Montmorillonite Clay on the Cetyltrimethylammonium Cations Adsorption. *Langmuir* **2005**, *21*, 8717–8723.

(45) Alemdar, A.; Öztekin, N.; Erim, F. B.; Ece, Ö. I.; Güngör, N. Effects of Polyethyleneimine Adsorption on Rheology of Bentonite Suspensions. *Bull. Mater. Sci.* **2005**, *28*, 287–291.

(46) Allan, G. G.; Akagane, K.; Neogi, A. N.; Reif, W. M.; Mattila, T. Physical Entrapment of Polyelectrolytes within Microporous Solids: the “Jack-in-the-Box” Effect. *Nature* **1970**, *225*, 175–176.

(47) Croitoru, C.; Pascu, A.; Roata, I. C.; Stanciu, E. M. Obtaining and Characterization of Polyolefin-Filled Calcium Carbonate Composites Modified with Stearic Acid. *IOP Conf. Ser.: Mater. Sci. Eng.* **2017**, *209*, 012041.

(48) Cai, G.-B.; Chen, S.-F.; Liu, L.; Jiang, J.; Yao, H.-B.; Xu, A.-W.; Yu, S.-H. 1,3-Diamino-2-Hydroxypropane-*N*,*N*,*N*′,*N*′-Tetraacetic Acid Stabilized Amorphous Calcium Carbonate: Nucleation, Transformation and Crystal Growth. *CrystEngComm* **2010**, *12*, 234–241.

(49) Xu, J. F.; Ji, W.; Shen, Z. X.; Tang, S. H.; Ye, X. R.; Jia, D. Z.; Xin, X. Q. Preparation and Characterization of CuO Nanocrystals. *J. Solid State Chem.* **1999**, *147*, 516–519.

(50) Aref, A. A.; Xiong, L.; Yan, N.; Abdulkarem, A. M.; Yu, Y. Cu_2O Nanorod Thin Films

Prepared by CBD Method with CTAB: Substrate Effect, Deposition Mechanism and Photoelectrochemical Properties. *Mater. Chem. Phys.* **2011**, *127*, 433–439.

(51) Chen, M.; Fan, L.; Qi, L.; Luo, X.; Zhou, R.; Zheng, X. The Catalytic Combustion of VOCs over Copper Catalysts Supported on Cerium-Modified and Zirconium-Pillared Montmorillonite. *Catal. Commun.* **2009**, *10*, 838–841.

(52) Li, H.; Gan, K.; Li, R.; Huang, H.; Niu, J.; Chen, Z.; Zhou, J.; Yu, Y.; Qiu, J.; He, X. Highly Dispersed NiO Clusters Induced Electron Delocalization of Ni–N–C Catalysts for Enhanced CO_2 Electroreduction. *Adv. Funct. Mater.* **2023**, *33*, 2208622.

(53) Liu, P.; Cheng, Z.; Ma, L.; Zhang, M.; Qiu, Y.; Chen, M.; Cheng, F. Cuprous Oxide Template Synthesis of Hollow-Cubic $Cu_2O@Pd_xRu_y$ Nanoparticles for Ethanol Electrooxidation in Alkaline Media. *RSC Adv.* **2016**, *6*, 76684–76690.

(54) Ma, M.; Djanashvili, K.; Smith, W. A. Selective Electrochemical Reduction of CO_2 to CO on CuO-Derived Cu Nanowires. *Phys. Chem. Chem. Phys.* **2015**, *17*, 20861–20867.

(55) Rupp, H.; Weser, U. X-Ray Photoelectron Spectroscopy of Copper(II), Copper(I), and Mixed Valence Systems. *Bioinorg. Chem.* **1976**, *6*, 45–59.

(56) Ivanova, T. M.; Maslakov, K. I.; Sidorov, A. A.; Kiskin, M. A.; Linko, R. V.; Savilov, S. V.; Lunin, V. V.; Eremenko, I. L. XPS Detection of Unusual Cu(II) to Cu(I) Transition on the Surface of Complexes with Redox-Active Ligands. *J. Electron Spectros. Relat. Phenomena* **2020**, *238*, 146878.

(57) Zhang, X.; Bi, F.; Zhu, Z.; Yang, Y.; Zhao, S.; Chen, J.; Lv, X.; Wang, Y.; Xu, J.; Liu, N. The Promoting Effect of H_2O on Rod-like MnCeOx Derived from MOFs for Toluene Oxidation: A Combined Experimental and Theoretical Investigation. *Appl. Catal. B* **2021**, *297*, 120393.

(58) Yang, Y.; Zhao, S.; Bi, F.; Chen, J.; Wang, Y.; Cui, L.; Xu, J.; Zhang, X. Highly Efficient Photothermal Catalysis of Toluene over Co_3O_4/TiO_2 p-n Heterojunction: The Crucial Roles of Interface Defects and Band Structure. *Appl. Catal. B* **2022**, *315*, 121550.

(59) Thommes, M.; Kaneko, K.; Neimark, A. V.; Olivier, J. P.; Rodriguez-Reinoso, F.; Rouquerol, J.; Sing, K. S. W. Physisorption of Gases, with Special Reference to the

Evaluation of Surface Area and Pore Size Distribution (IUPAC Technical Report). *Pure Appl. Chem.* **2015**, *87*, 1051–1069.

(60) Mendes, P. C. D.; Ocampo-Restrepo, V. K.; Da Silva, J. L. F. *Ab Initio* Investigation of Quantum Size Effects on the Adsorption of CO_2, CO, H_2O, and H_2 on Transition-Metal Particles. *Phys. Chem. Chem. Phys.* **2020**, *22*, 8998–9008.

(61) Yudanov, I. V.; Genest, A.; Schauermann, S.; Freund, H.-J.; Rösch, N. Size Dependence of the Adsorption Energy of CO on Metal Nanoparticles: A DFT Search for the Minimum Value. *Nano Lett.* **2012**, *12*, 2134–2139.

Chapter 4. Material synthesis using carbon nitride

ABSTRACT: In Chapters 2 and 3, the formation of silica (SiO_2) and CuO_x species was individually induced. In Chapter 4, carbon nitride was used as the structure-directing agent for simultaneously controlling SiO_2 and CuO formation in the development of nanoporous CuO–SiO_2 nanocomposites by calcining a mixture of Cu^{2+}, polyhedral oligomeric silsesquioxane (POSS), and carbon nitride to solve CuO problems (e.g., porosity control and low efficiency per weight relative to light materials). Furthermore, the formation factors of the nanocomposites were investigated using comparative experiments to understand the roles of Cu^{2+}, POSS, and carbon nitride. During calcination, carbon nitride induced SiO_2 formation, which supported CuO; the effect of Cu species contributed to the removal of carbon nitride. Subsequently, nanoporous CuO–SiO_2 nanocomposites were formed, presenting a unique morphology (i.e., a fluffy structure), high surface area, and narrow optical band gap. First, the silica/g-C_3N_4 nanocomposite was synthesized by inducing SiO_2 formation only, as shown in Section 4-1. Subsequently, in Section 4-2, nanoporous CuO–SiO_2 nanocomposites were constructed by adding Cu species to the system described in Section 4-1.

4-1. Synthesis of silica/g-C_3N_4 nanocomposite

4-1-1. Introduction

g-C_3N_4 is synthesized via the pyrolysis of N-rich precursors, such as melamine and urea. g-C_3N_4 has a graphitic structure consisting of C and N; it has the advantages of abundant elemental resources, high thermal stability, biocompatibility, and a suitable band structure as a photocatalyst.[1] Research on photocatalysts has been actively conducted by leveraging these characteristics. However, in applying g-C_3N_4 to photocatalysts, g-C_3N_4 has several issues, such as a low specific surface area and limited (insufficient) visible-light response range.[2] Improvement of the catalytic performance, such as CO_2 reduction[3] and H_2 evolution,[4] requires synthesizing g-C_3N_4 with high porosity and a controlled electronic state. Porous (nanoporous) g-C_3N_4 has been prepared using various methods, including exfoliation with thermal treatment,[5] templated synthesis using silica nanoparticles as templates,[6] and the fabrication of composites

with other materials, such as silica nanosheets.[7]

In addition to the porosity mentioned above, controlling the electronic structure of g-C_3N_4 by doping different elements and introducing defects leads to the construction of g-C_3N_4 with excellent surface structure and electronic properties, contributing to performance improvement in the adsorption/separation and conversion of substances. g-C_3N_4 can be synthesized using the bottom-up method from N-rich precursors. Therefore, specific elements and structures can be introduced by adding compounds with these elements and structures to the synthesis system. In elemental doping, B and S are introduced using boron oxide[8] or thiourea.[9] Furthermore, g-C_3N_4 with amino/imino moieties and an aromatic structure can be synthesized using organic compounds with several NH_x groups and aromatic compounds with suitable structures (dibromo aromatic compounds), respectively.[10,11] The use of ionic liquids has also been investigated.[12]

In this section, a silica/g-C_3N_4 nanocomposite was synthesized using POSS, whose structure has Si and O arranged in a cage structure, as a silica source, and quaternary ammonium cations used for controlling the electronic structure of g-C_3N_4, in the POSS–quaternary ammonium complex (PSS) to construct g-C_3N_4, which has high porosity and excellent electronic properties.

4-1-2. Experimental section

4-1-2-1. Chemicals

Urea was purchased from FUJIFILM Wako Pure Chemical Corporation, Japan. Octakis(tetramethylammonium) pentacyclo[9.5.1.$1^{3,9}$.$1^{5,15}$.$1^{7,13}$]octasiloxane-1,3,5,7,9,11,13,15-octakis(yloxide)hydrate (PSS, lot MKCL1508) was purchased from Sigma-Aldrich. Distilled water was produced using a purification system (RFD240NA, ADVANTEC) and was used in all experiments.

4-1-2-2. Synthesis

Preparation of g-C_3N_4 precursor

Urea (30 g) was placed in a closed alumina box (the length, width, and height of the box were 70, 70, and 50 mm, respectively). It was heated at 400 °C for 2 h (ramping rate: 3 °C min^{-1}) under

an air atmosphere. Subsequently, carbon nitride (U400) was obtained by naturally cooling the resultant product to room temperature.

As a comparative sample, U500 was synthesized by heating urea (30 g) at 500 °C for 2 h (ramping rate: 3 °C min^{-1}) in a closed alumina box and under an air atmosphere.

Synthesis of silica/g-C_3N_4 nanocomposite

PSS (500 mg) was added to 100 mL of water, and the mixture was sonicated for 30 min to disperse PSS. 1 g of U400 was added to the dispersion and sonicated for 30 min to disperse each material. The obtained dispersion was transferred to a container and heated at 90 °C (ramping rate: 3 °C min^{-1}) for 18 h to evaporate water. After grinding the dried powder at the bottom of the container, it was transferred to a closed alumina box and calcined at 550 °C for 2 h (ramping rate: 3 °C min^{-1}) under an air atmosphere to synthesize the silica/g-C_3N_4 nanocomposite (U400/PSS 550 °C) (Scheme 4-1).

As a comparative sample, U400 550 °C was synthesized by heating U400 at 550 °C for 2 h (ramping rate: 3 °C min^{-1}) in a closed alumina box and under an air atmosphere.

Scheme 4-1. The synthesis of the silica/g-C_3N_4 nanocomposite.

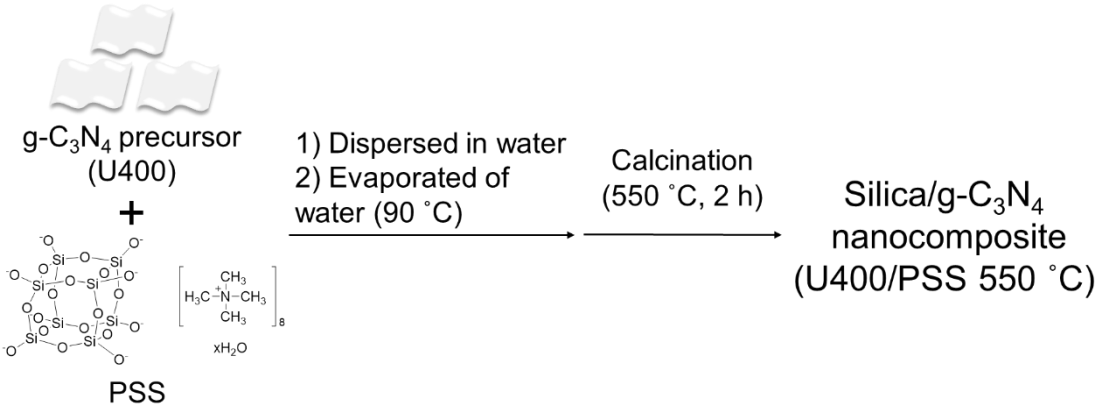

4-1-2-3. Characterization

Powder XRD was conducted using a MiniFlex II (Rigaku Corporation, Japan) with

monochromatic X-rays of Cu Kα (λ = 0.154 nm) at room temperature. The tube voltage, current, 2θ range, and step size were 30 kV, 15 mA, 5–60°, and 0.02°, respectively. TGA was conducted using a thermogravimetric-differential thermal analyzer (Rigaku Corporation, Japan, Thermo plus EVO2 TG-DTA8122). After maintaining the temperature at 95 °C to remove water attached to the materials, the temperature was raised to 800 °C (ramping rate: 10 °C min^{-1}), and weight loss was calculated from the result of weight fluctuations. The elemental states were analyzed using XPS (JEOL, JPS-9030), and the X-ray source was Mg Kα (1253.6 eV). The path energies were 50 eV for wide scans and 10 eV for narrow scans. The measured sample was coated over the carbon tape on the substrate. (There is a possibility of carbon and silicone contamination.) Charge compensation was achieved using a flood gun. The binding energy of the C 1s peak at 284.8 eV was used as a reference to calibrate the binding energy scale. In addition, the porous structure was evaluated using BELSORP-mini (MicrotracBEL Corp., Japan). N_2 adsorption–desorption tests were performed at 77 K to obtain the adsorption–desorption isotherms of the samples. All samples were evacuated at 150 °C for 3 h before measurements. The isotherms were analyzed using the BET equation to determine S_{BET}. The pore size distribution was obtained by analyzing the adsorption isotherms using the BJH method. Ultraviolet-visible (UV–vis) spectra were obtained using a Jasco V-770 spectrophotometer (Jasco, Japan) employed for UV–vis diffuse reflectance spectroscopy over a wavelength range of 200–800 nm.

4-1-3. Results and discussion

g-C_3N_4 precursors (U400) were prepared by heating urea at 400 °C. Crystalline structures were obtained using XRD. The XRD pattern of U400 showed different peaks compared to that of urea, indicating the conversion of urea (Figure 4-1). The XRD pattern of U400 was similar to that synthesized in a previous report.[13] The peak positions were relatively close to those of g-C_3N_4 [27.4° (002) and 13.0° (100)],[14] indicating the construction of the g-C_3N_4 intermediate (e.g., melem and carbon nitride). The elemental states of U400 were confirmed using XPS (Figure 4-2). The XPS survey scan (Figure 4-2a) revealed the presence of C and N derived from carbon nitride in U400. The C 1s region (Figure 4-2b) showed two peaks derived from adventitious

hydrocarbons from the XPS instrument, and defect-containing sp^2-hybridized carbon atoms existed in the graphitic domains (284.8 eV) and C–N–C (288.3 eV).[15] The peak in the N 1s region was deconvoluted into three components: neutral imine (398.6 eV), neutral amine (399.3 eV), and positively charged N species (400.4 eV) (Figure 4-2c).[16] Furthermore, U400 was highly dispersed in water—the dispersion medium in the process of intermediate preparation—compared with U500, which was prepared by heating urea at 500 °C for 2 h (Figure 4-3). Consequently, U400 was used in material synthesis.

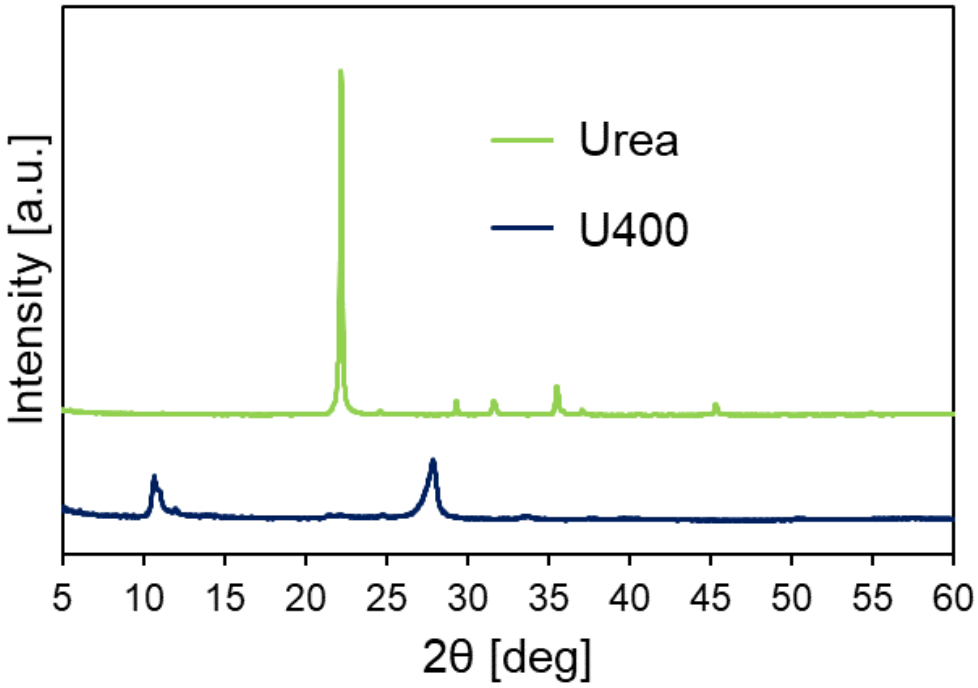

Figure 4-1. XRD patterns for urea and U400.

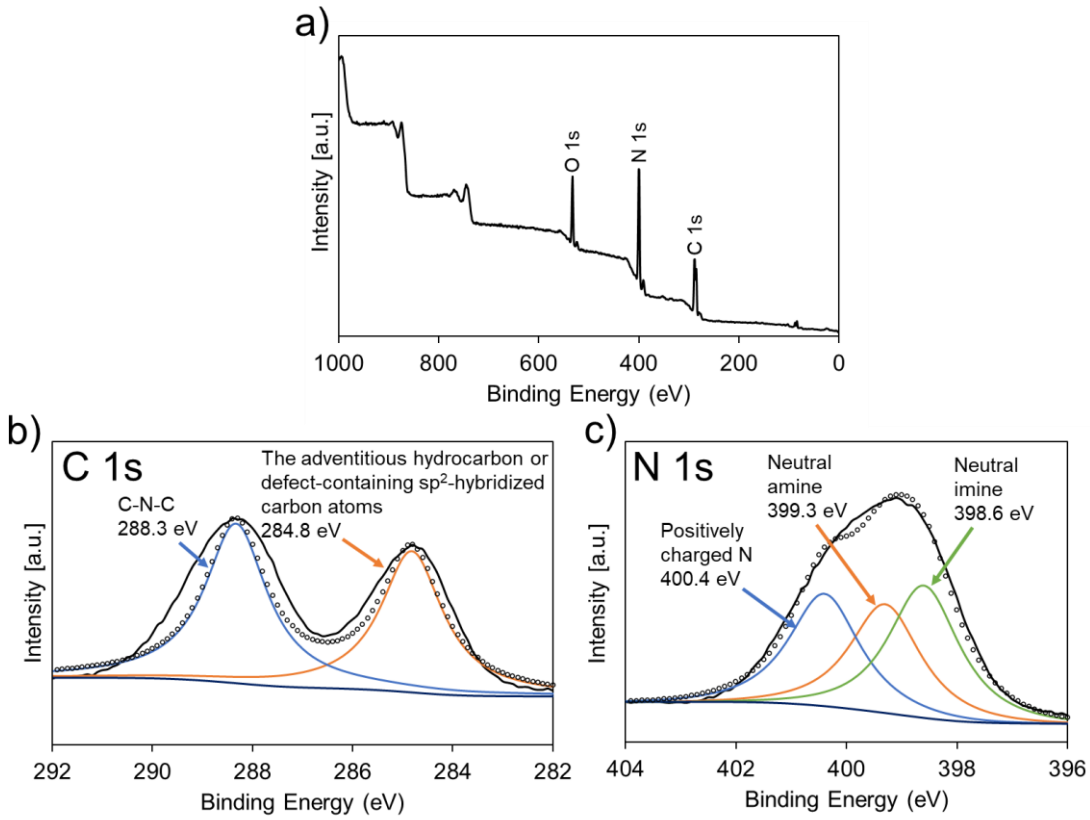

Figure 4-2. a) XPS survey scan and high-resolution XPS spectra in b) C 1s region and c) N 1s region for U400.

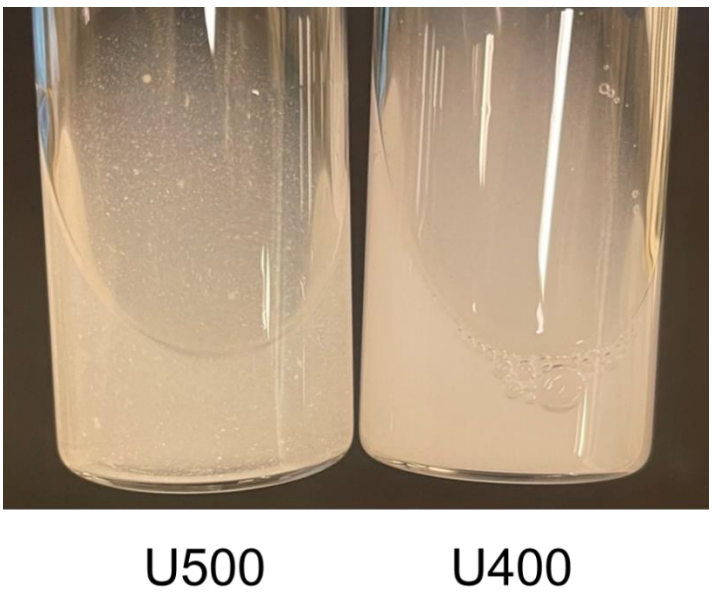

Figure 4-3. The dispersibility of U400 and U500 in water after sonication for approximately 5 min.

Subsequently, the intermediate of the silica/g-C_3N_4 nanocomposite (U400/PSS 90 °C) was prepared by mixing U400 and PSS, and the prepared intermediate was calcined to form the silica/g-C_3N_4 nanocomposite (U400/PSS 550 °C). The crystalline structure was analyzed using XRD (Figure 4-4). In the XRD pattern of U400/PSS 550 °C, the (002) peak was confirmed,[14] indicating the formation of g-C_3N_4. XPS spectra were measured to confirm the elemental state of each sample. Figure 4-5 shows the XPS spectra of the samples after calcination (U400/PSS 550 °C). The XPS survey scan confirmed the elements of C and N derived from g-C_3N_4 (Figure 4-5a). Similar to U400, the spectrum of the C 1s region (Figure 4-5b) showed two peaks: the adventitious hydrocarbon and the defect-containing sp^2-hybridized carbon atoms (284.8 eV) and C–N–C (287.9 eV).[15] In the spectrum in the N 1s region (Figure 4-5c), the peak was deconvoluted to four peaks derived from g-C_3N_4 (C=N–C (398.6 eV), N-$(C)_3$ (399.5 eV), N–H (400.9 eV), and charging effects (404.1 eV)),[15,17] indicating that g-C_3N_4 was synthesized. The XPS spectra in the Si 2p range of the samples before (U400/PSS 90 °C) and after calcination at 550 °C (U400/PSS 550 °C) were analyzed to confirm SiO_2 formation, as shown in Figure 4-6. In U400/PSS 90 °C, the peak position was 102.6 eV, attributed to Si–O.[18] However, in U400/PSS 550 °C, the peak position was shifted toward the higher binding energy side (103.4 eV). As the position around 103.7 eV was attributed to silica (SiO_2) in an earlier study,[18] the formation of silica proceeded with calcination. In addition, according to the TGA results in U400/PSS 550 °C (Figure 4-7), the residue ratio at 800 °C (approximate silica ratio) was approximately 32 wt%.

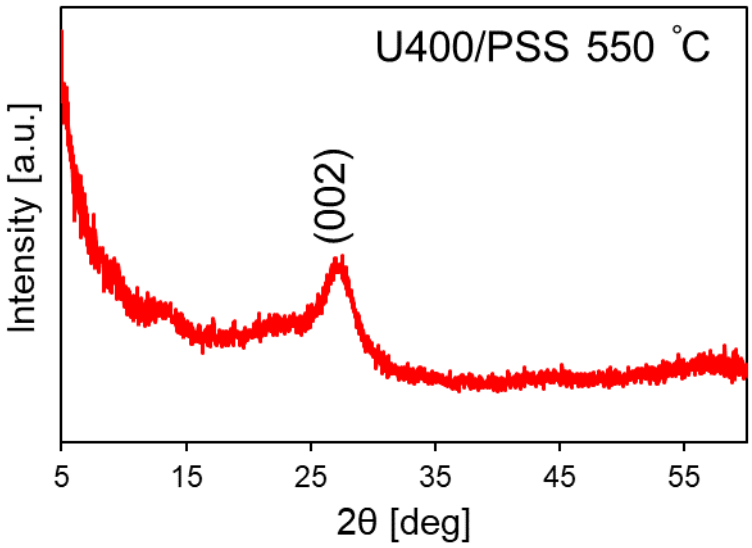

Figure 4-4. XRD pattern of U400/PSS 550 °C.

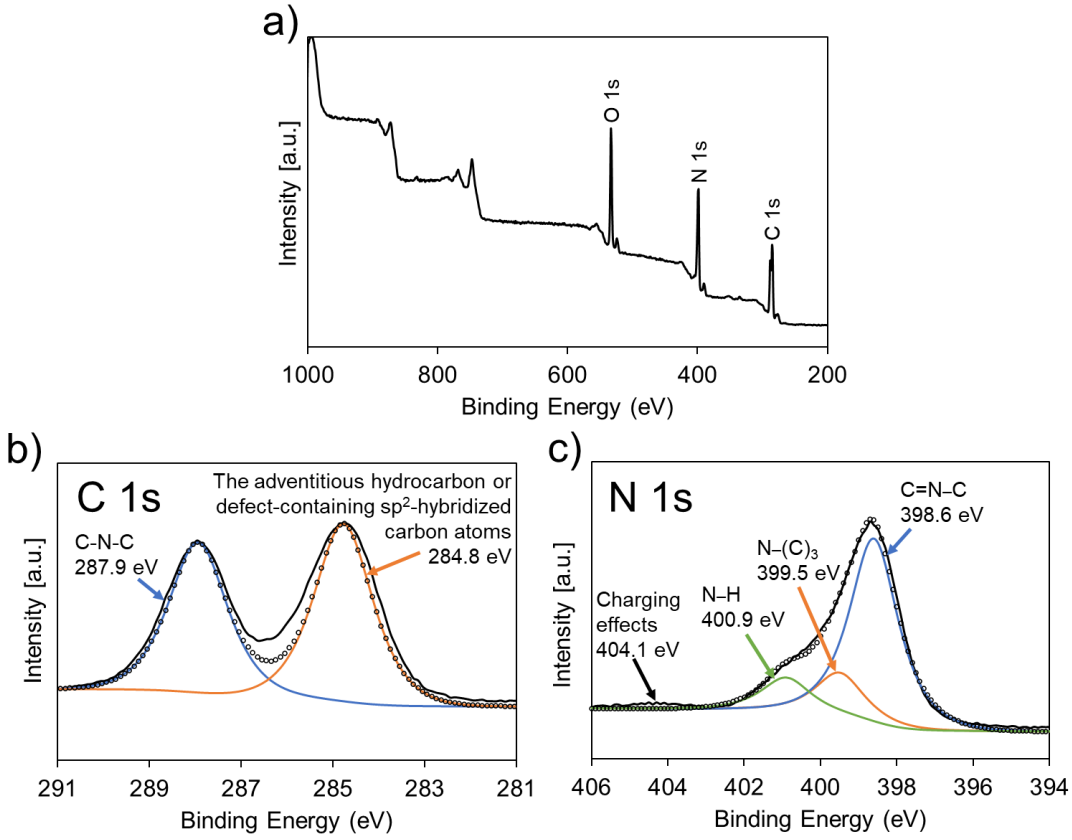

Figure 4-5. a) XPS survey scan and high-resolution XPS spectra in b) the C 1s region and c) the N 1s region for U400/PSS 550 °C.

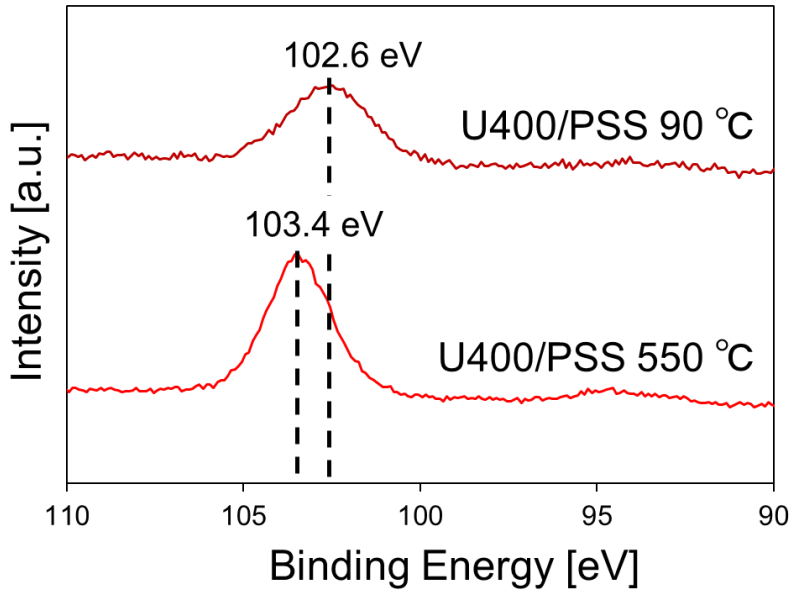

Figure 4-6. High-resolution XPS spectra in the Si 2p region for U400/PSS 90 °C and U400/PSS 550 °C.

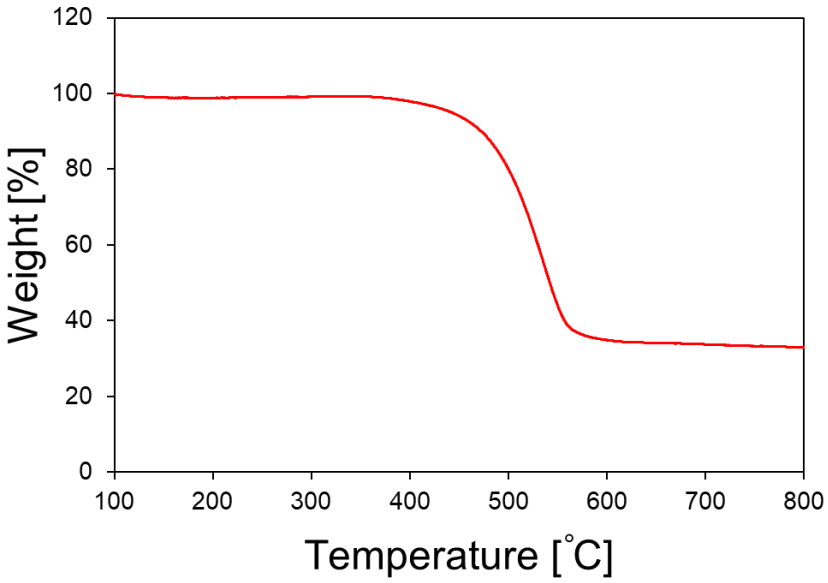

Figure 4-7. TGA curve for U400/PSS 550 °C.

N_2 adsorption–desorption isotherms in U400/PSS 550 °C and U400 550 °C are shown in Figure 4-8. S_{BET} were 89 m^2 g^{-1} for U400/PSS 550 °C and 39 m^2 g^{-1} for U400 550 °C, and U400/PSS 550 °C had larger S_{BET}. This increase might result from the introduction of silica.

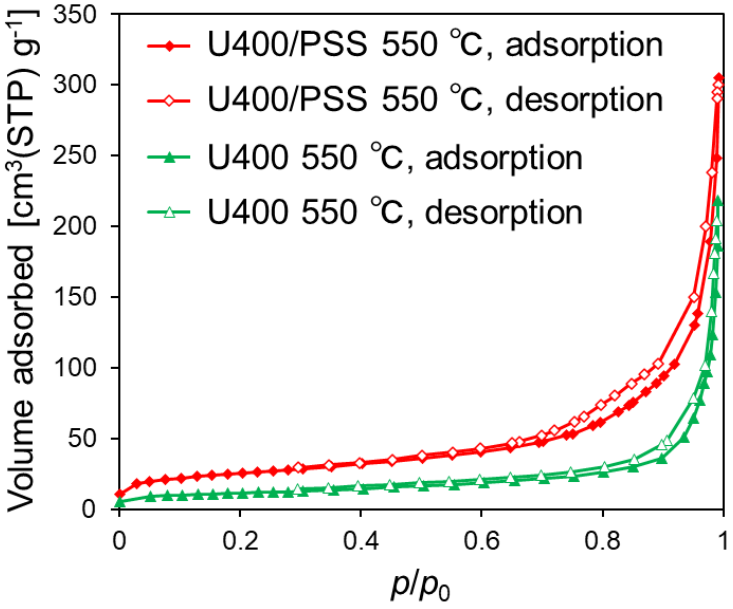

Figure 4-8. N_2 adsorption–desorption isotherms for U400/PSS 550 °C and U400 550 °C.

The UV–vis absorption spectra of U400 550 °C and U400/PSS 550 °C are shown in Figure 4-9. The absorption region of U400/PSS 550 °C was shifted to a higher wavelength side compared to that of U400 550 °C and exhibited a higher visible-light absorption property. The optical band gaps were calculated using the Tauc approach (Figure 4-10) $[F(R\infty)hv]^n = A\,(hv - E_g)$, where A is a constant, n is a coefficient (n = 1/2 for the materials with an indirection band gap and n = 2 for the materials with a direction band gap), h is the Planck constant, v is the photon frequency rate, E_g is the band gap, and $F(R\infty)$ is the Kubelka–Munk function.[19–21] The band gaps were 2.75 eV for U400 550 °C and 2.49 eV for U400/PSS 550 °C; U400/PSS 550 °C had a narrower band gap than U400 550 °C. This change might result from the introduction of defective structures (e.g., N defects)[4] into the g-C_3N_4 framework through the influence of quaternary ammonium cations in PSS.

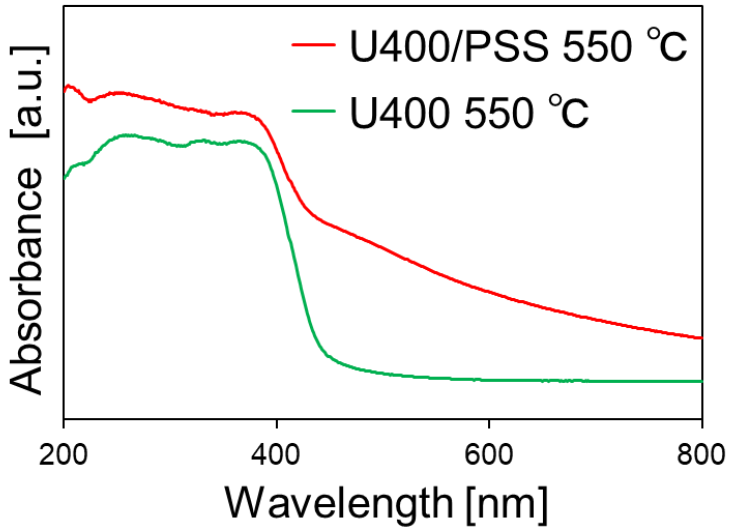

Figure 4-9. UV–vis absorption spectra of U400 550 °C and U400/PSS 550 °C.

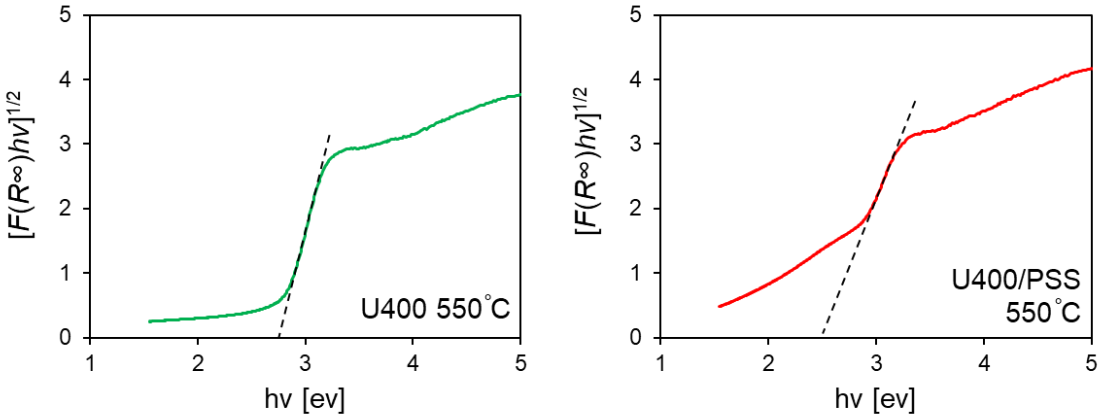

Figure 4-10. Optical band gaps of U400 550 °C and U400/PSS 550 °C determined with plots of $[F(R\infty)h\nu]^{1/2}$ *versus* photon energy ($h\nu$).

4-1-4. Conclusion

In summary, a silica/g-C_3N_4 nanocomposite was synthesized using POSS as a silica source and quaternary ammonium cations to control the electronic states of g-C_3N_4 in PSS. The constructed silica/g-C_3N_4 nanocomposite exhibited higher porosity and visible-light absorption characteristics than g-C_3N_4 synthesized without adding PSS. The synthesized material is expected to be applied to adsorbents and photocatalysts.

4-2. Structure-directing synthesis of nanoporous CuO–SiO_2 nanocomposites using carbon nitride

4-2-1. Introduction

g-C_3N_4 has a two-dimensional structure composed of hexatomic rings, containing C and N, and a charged superficial structure;[22] it is also used as a template for material synthesis. Silica,[23,24] metal oxide (CuO),[25] TMD,[22] and carbon[26] nanosheets are examples of template-synthesized substances. Furthermore, composites such as Ni–CeO_2,[27] Mo_2C–carbon,[28] VN/nitrogen-doped carbon,[29] and single-atom Fe/nitrogen-rich carbon[30] were fabricated using carbon nitride as a template. However, studies have not investigated the use of carbon nitride to control the nanocomposite structure in CuO and SiO_2, which have elemental abundance, low toxicity, and high thermal and chemical stability.[31]

In this study, nanoporous CuO–SiO_2 nanocomposites with a high specific surface area and unique morphologies were developed using a structure-directing synthesis to control CuO and SiO_2 formation. POSS, in which Si and O are arranged in a cage structure, and carbon nitride were used as the SiO_2 source and the structure-directing agent, respectively. Nanoporous CuO–SiO_2 nanocomposites were fabricated by calcining a mixture of Cu^{2+}, POSS, and carbon nitride (Scheme 4-2). The properties of the nanoporous CuO–SiO_2 nanocomposites (e.g., their morphology and porosity) were analyzed, and the effects of Cu^{2+}, POSS, and carbon nitride on the design and structure of the CuO–SiO_2 nanocomposites were investigated.

4-2-2. Experimental section

4-2-2-1. Chemicals

Urea was obtained from FUJIFILM Wako Pure Chemical Corporation, Japan. PSS (lot MKCL1508) was purchased from Sigma-Aldrich. $Cu(OAc)_2 \cdot H_2O$ was purchased from Nacalai Tesque Inc., Japan. Distilled water was produced using a purification system (RFD240NA, ADVANTEC) and was used in all experiments.

4-2-2-2. Synthesis

Preparation of carbon nitride

Urea (30 g) was placed in a closed alumina box (the length, width, and height of the box were 70, 70, and 50 mm, respectively) and heated at 400 °C for 2 h (ramping rate: 3 °C min^{-1}) under an air atmosphere. Subsequently, carbon nitride (U400) was obtained by naturally cooling the resultant product to room temperature.

Synthesis of nanoporous CuO–SiO_2 nanocomposites

I added PSS (250, 500, 1500 mg) and $Cu(OAc)_2 \cdot H_2O$ (350, 700, 2100 mg) to water (100 mL), where the ratio of PSS and $Cu(OAc)_2 \cdot H_2O$ was fixed at 1:8 (mol:mol) and PSS was assumed to contain no H_2O. The mixture was sonicated for 30 min. Subsequently, U400 (1 g) was added to the dispersed water, and the mixture was sonicated for 30 min to disperse each material. The obtained dispersion was transferred to a container and heated at 90 °C for 18 h (3 °C min^{-1}) to evaporate the water. The dried powder at the bottom of the container was ground. (The intermediate product name up to this point in the process was U400/PSSx/Cu 90 °C, x: PSS amount.) U400/PSSx/Cu 90 °C was placed in a closed alumina box and calcined at 550 °C for 2 h (ramping rate: 3 °C min^{-1}) under an air atmosphere. As a result, nanoporous CuO–SiO_2 nanocomposites (U400/PSSx/Cu 550 °C) were obtained.

Synthesis of comparative samples

Comparative samples were synthesized to investigate the role of each material based on the amounts of PSS (500 mg) and $Cu(OAc)_2 \cdot H_2O$ (700 mg) without adding U400 (the intermediate product name was PSS/Cu 90 °C, and the final product name was PSS/Cu 550 °C); PSS (the intermediate product name was U400/Cu 90°C, and the final product name was U400/Cu 550 °C); and $Cu(OAc)_2 \cdot H_2O$ (the intermediate product name was U400/PSS 90 °C, the final product name was U400/PSS 550 °C), respectively. Pristine CuO ($Cu(OAc)_2 \cdot H_2O$ 550 °C) was obtained by calcining $Cu(OAc)_2 \cdot H_2O$ at 550 °C for 2 h (ramping rate: 3 °C min^{-1}) under an air atmosphere.

The effect of calcination temperature was investigated using U400/PSS1500/Cu 90 °C.

U400/PSS1500/Cu 90 °C was placed in a closed alumina box and calcined at 200 °C, 400 °C, and 550 °C (ramping rate: 3 °C min^{-1}) under an air atmosphere without maintaining the temperature. After the samples cooled naturally to room temperature, comparative samples U400/PSS1500/Cu y °C (0 h) (y: calcination temperature) were obtained.

4-2-2-3. Characterization

Powder XRD was conducted using a MiniFlex II instrument (Rigaku Corporation, Japan) with monochromatic X-rays of Cu Kα (λ = 0.154 nm) at room temperature. The tube voltage, current, 2θ range, and step size were 30 kV, 15 mA, 5–60°, and 0.02°, respectively. XPS (JEOL JPS-9030, Japan) was used to analyze the states of C, N, Si, and Cu in the materials. The X-ray source was Mg Kα (1253.6 eV). The path energies were 50 eV for the wide scans and 10 eV for the narrow scans. Carbon tape was used to fix the sample to the substrate. (There is a possibility of carbon and silicone contamination.) Charge compensation was achieved using a flood gun. The binding energy of the C 1s peak at 284.8 eV was employed as a reference to calibrate the binding energy scale. ^{29}Si solid-state NMR (ssNMR) spectra were obtained using an Avance III NMR spectrometer (Bruker) with an 11.7 T magnet. In addition, this study used an ϕ4 mm NMR sample rotor for magic angle spinning (MAS) measurements with an 8 kHz rotation. A single-pulse sequence with a 4.2 μs pulse was applied. Sample morphologies were observed using SEM (Keyence Corporation, Japan, VE-9800), and the SEM images were captured at an accelerating voltage of 5 kV. EDX (Keyence Corporation, Japan, 971863SP) was used to measure the element ratios of Si and Cu, and the average of 10 measurements was used as the element ratio. TEM and annular dark-field scanning transmission electron microscopy (ADF-STEM)-EDX measurements were conducted using a JEM-ARM200F (JEOL, Japan). The TEM and STEM observations were performed at 200 kV. The porous structure was examined using a BELSORP-mini (MicrotracBEL Corp., Japan). N_2 adsorption–desorption tests were performed at 77 K to obtain the adsorption–desorption isotherms of the samples. All samples were evacuated at 150 °C for 3 h before measurements. The isotherms were analyzed using the BET equation to determine S_{BET} of the samples. Moreover, the adsorption isotherm was analyzed using the BJH method to obtain the

pore size distribution. UV–vis spectra were obtained using a Jasco V-770 spectrophotometer (Jasco, Japan) for UV–vis diffuse reflectance spectroscopy over a wavelength of 200–1200 nm.

4-2-2-4. CO_2 adsorption test

CO_2 adsorption tests were conducted using BELSORP-max (MicrotracBEL Corp., Japan) at 303 K. The sample was evacuated at 110 °C for 12 h before measurement.

4-2-3. Results and discussion

4-2-3-1. Synthesis and characterization of nanoporous CuO–SiO_2 nanocomposites

Nanoporous CuO–SiO_2 nanocomposites (U400/PSSx/Cu 550 °C) were synthesized by calcining a mixture of Cu^{2+}, POSS, and U400 using PSS as the silica source and carbon nitride as the structure-directing agent (Scheme 4-2).

Scheme 4-2. Construction of nanoporous CuO–SiO_2 nanocomposites using carbon nitride as a structure-directing agent.

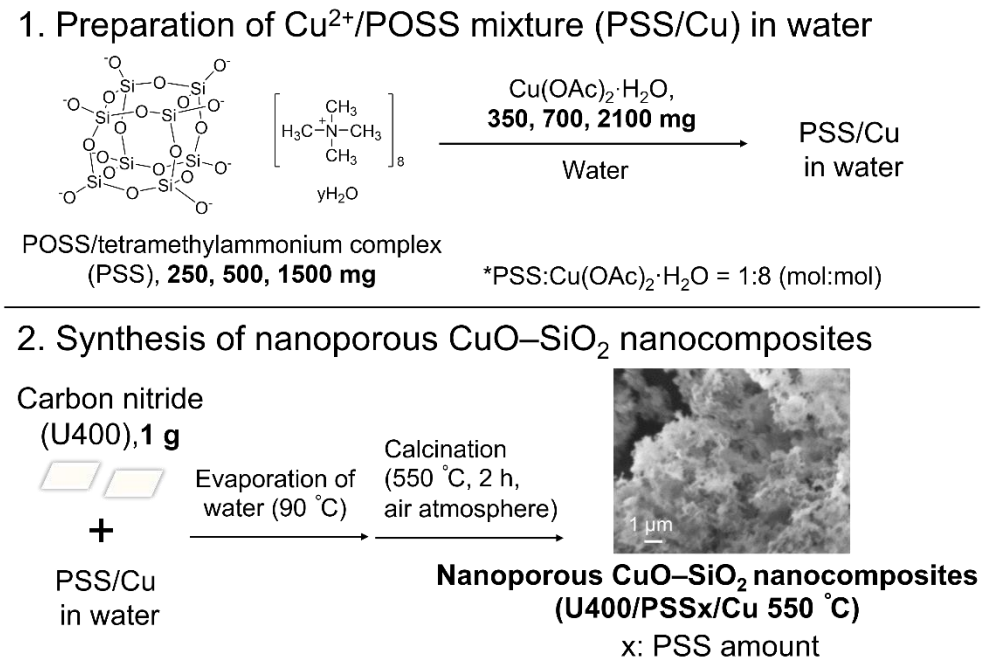

First, a mixture of Cu^{2+} and POSS (PSS/Cu) was prepared. The PSS/Cu states were confirmed

by analyzing the crystalline structure of PSS/Cu 90 °C, which was synthesized by drying a mixture of PSS and $Cu(OAc)_2 \cdot H_2O$ in water using XRD. The XRD patterns for PSS/Cu 90 °C are shown in Figure 4-11 and 4-12. A peak at $2\theta = 11.5°$ was detected in PSS/Cu 90 °C, which was not observed in PSS or $Cu(OAc)_2 \cdot H_2O$ (Figure 4-11), indicating that structural changes occurred in PSS and $Cu(OAc)_2 \cdot H_2O$ during the mixing or drying process. Second, a mixture of Cu^{2+}, POSS, and U400 (U400/PSSx/Cu 90 °C) was prepared by mixing U400 with Cu^{2+}/POSS-dispersed water and evaporating water in U400/Cu^{2+}/POSS-containing water. The XRD pattern of U400/PSS250/Cu 90 °C was similar to that of U400 (Figure 4-12). Although the peak at $2\theta = 9.3°$ was confirmed in U400/PSS250/Cu 90°C, it was not detected in U400 or PSS/Cu 90°C (Figure 4-12). Furthermore, peaks, for example, between 14° and 17° and around 25°, which were not confirmed in U400/PSS250/Cu 90°C or U400/PSS500/Cu 90°C, were observed in U400/PSS1500/Cu 90°C (Figure 4-13). These facile peaks and pattern changes might result from structural changes in U400, Cu^{2+}, or POSS when they were combined during the fabrication of U400/PSSx/Cu 90°C and the concentration differences of Cu^{2+}/POSS in U400/Cu^{2+}/POSS mixtures.

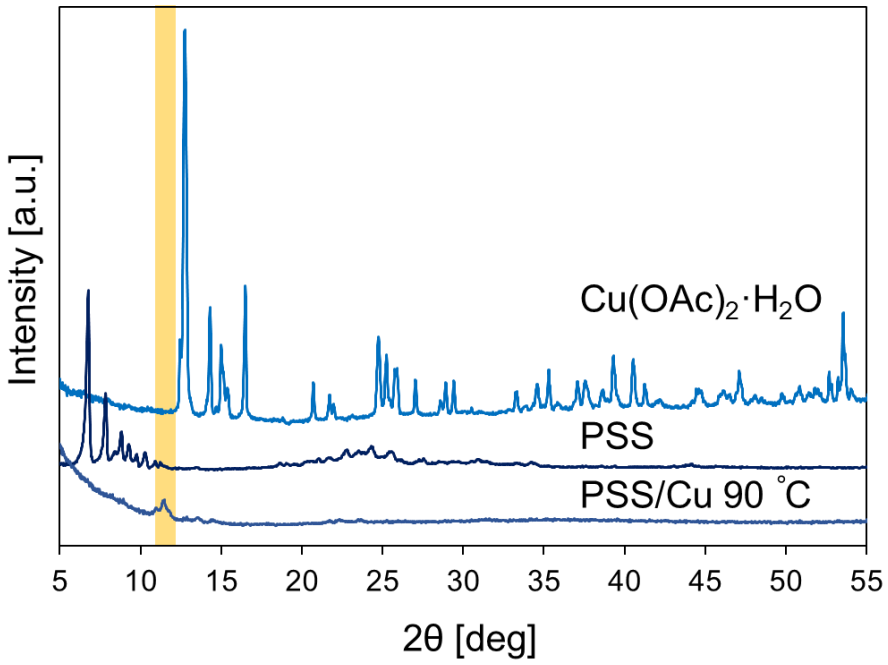

Figure 4-11. XRD patterns for $Cu(OAc)_2 \cdot H_2O$, PSS, and PSS/Cu 90 °C.

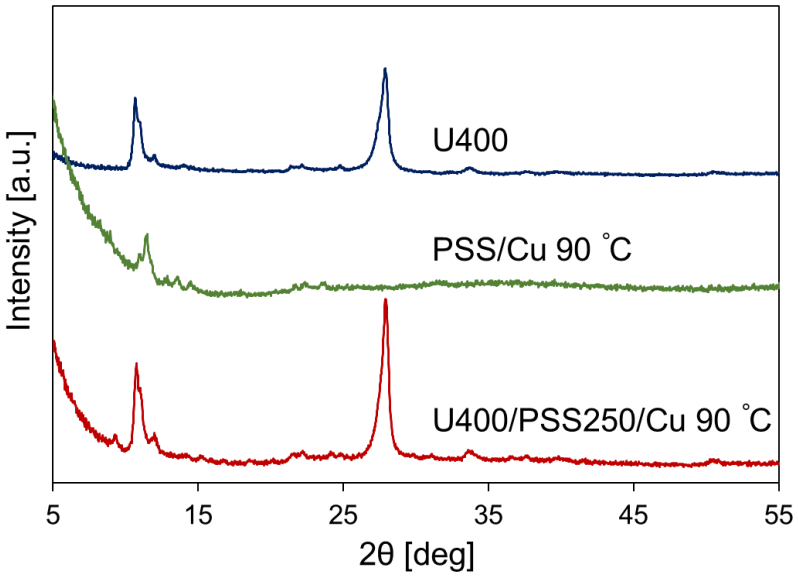

Figure 4-12. XRD patterns for U400, PSS/Cu 90 °C, and U400/PSS250/Cu 90 °C.

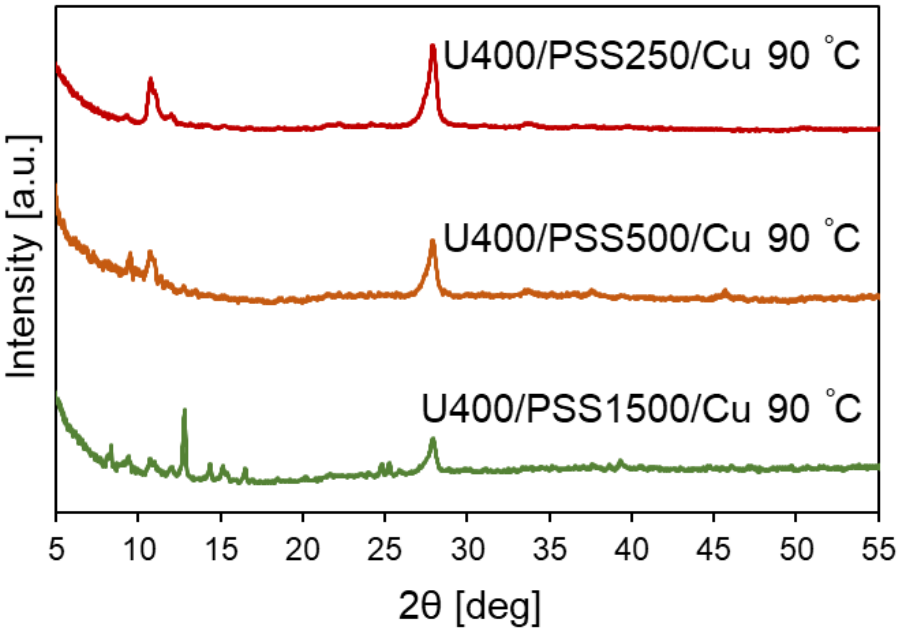

Figure 4-13. XRD patterns for each U400/PSSx/Cu 90 °C.

Subsequently, nanoporous CuO–SiO_2 nanocomposites (U400/PSSx/Cu 550 °C) were constructed by calcining the obtained intermediates (U400/PSSx/Cu 90 °C) at 550 °C under an air atmosphere. The CuO and SiO_2 formation and removal of carbon nitride were confirmed using XRD and XPS. According to the XRD patterns of U400/PSSx/Cu 550 °C (Figure 4-14 and 4-15), the peaks attributed to CuO[32] were detected, and the patterns were close to that of $Cu(OAc)_2 \cdot H_2O$ 550 °C synthesized by heating $Cu(OAc)_2 \cdot H_2O$ at 550 °C under an air atmosphere. Accordingly, CuO was formed by calcining U400/PSSx/Cu 90 °C. The peak intensity at 36° was higher than that at 39° in U400/PSSx/Cu 550 °C. In addition, the tendency was opposite to $Cu(OAc)_2 \cdot H_2O$ 550 °C, indicating that the crystal growth of CuO was directed by carbon nitride, PSS (-derived SiO_2), or both. Furthermore, the widths at the half-maximum intensity of the peaks at 36° were 0.32° in U400/PSS250/Cu 550 °C and 0.29° in $Cu(OAc)_2 \cdot H_2O$ 550 °C. Those at 39° in U400/PSS250/Cu 550 °C and $Cu(OAc)_2 \cdot H_2O$ were 0.41° and 0.31°, respectively. A comparison between U400/PSS250/Cu 550 °C and $Cu(OAc)_2 \cdot H_2O$ 550 °C revealed that the widths at 36° were close. However, the width at 39° in U400/PSS250/Cu 550 °C was wider than that in $Cu(OAc)_2 \cdot H_2O$ 550 °C. According to the Scherrer equation ($D_{hkl} = K\lambda/B\cos\theta$, where D_{hkl} represents the length of crystallite in the direction perpendicular to the lattice planes (*hkl*), K is the Scherrer constant, λ is the wavelength of the X-ray, B represents the corrected band broadening after subtraction of equipment broadening, and θ is the half diffraction angle[33–35]), when B increases, D_{hkl} decreases. Accordingly, $D_{111,200}$ in U400/PSS250/Cu 550 °C was smaller than that in $Cu(OAc)_2 \cdot H_2O$ 550 °C. These XRD results indicate that crystal growth in the direction perpendicular to the (111, 200) planes was suppressed in U400/PSS250(x)/Cu 550 °C compared with $Cu(OAc)_2 \cdot H_2O$ 550 °C.

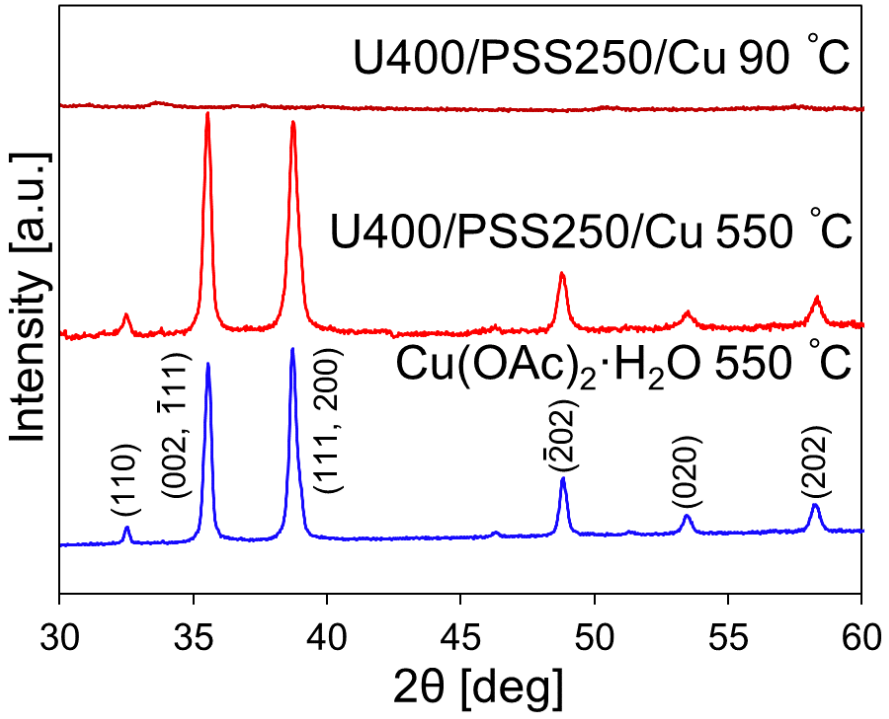

Figure 4-14. XRD patterns for U400/PSS250/Cu 90 °C, U400/PSS250/Cu 550 °C, and $Cu(OAc)_2 \cdot H_2O$ 550 °C.

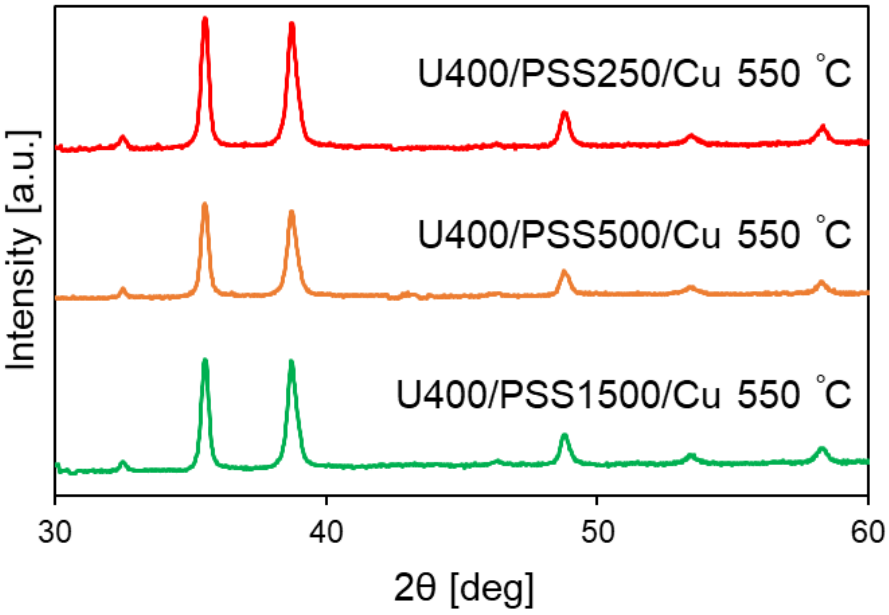

Figure 4-15. XRD patterns for each U400/PSSx/Cu 550 °C.

The elemental states of N, Si, and Cu were confirmed using XPS (Figure 4-16 and 4-17a–c). The survey scans showed that C, N, O, Si, and Cu existed in U400/PSS250/Cu 90 °C and C, O, Si, and Cu were detected in the U400/PSS250/Cu 550 °C (Figure 4-16).

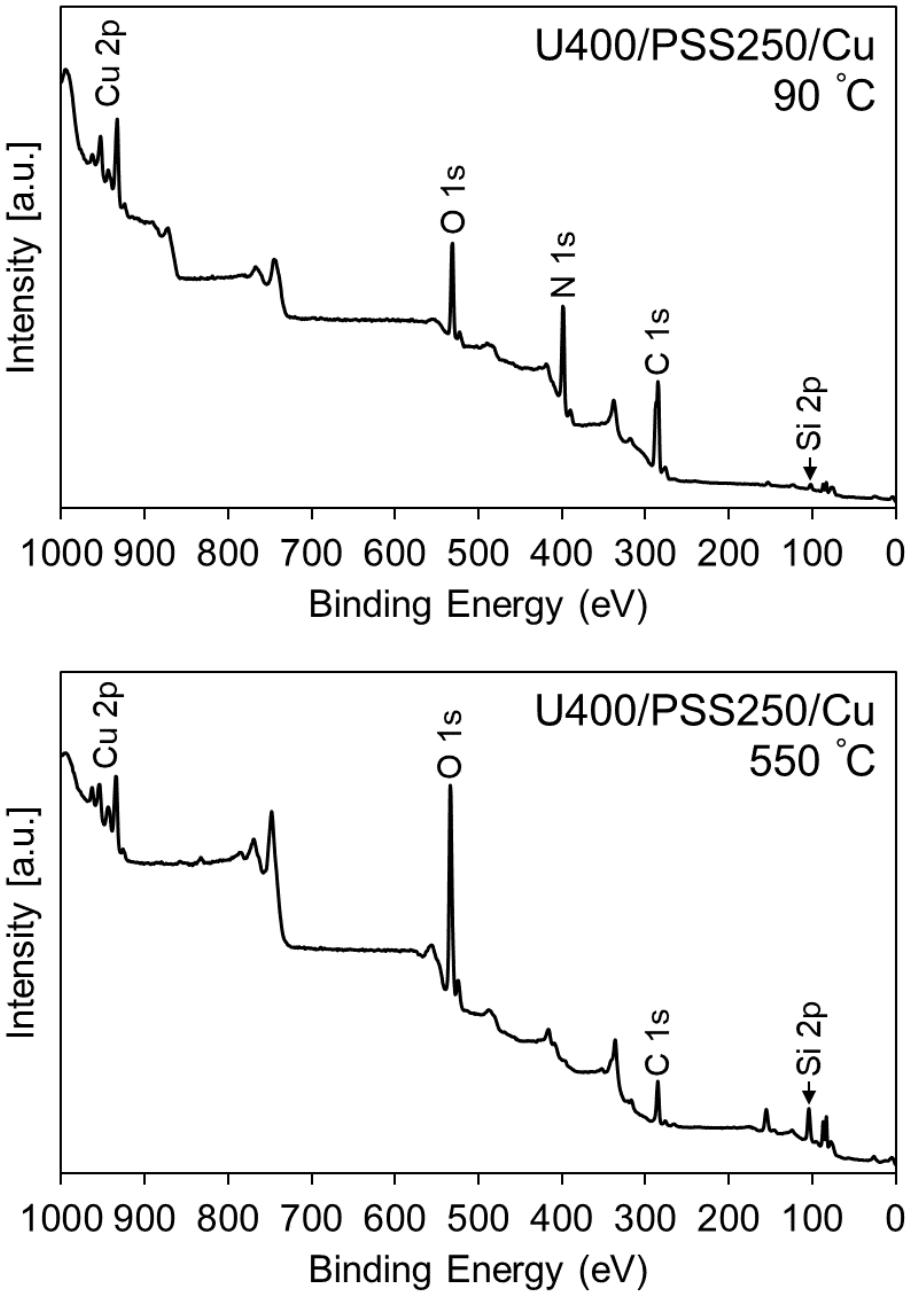

Figure 4-16. XPS survey scan for U400/PSS250/Cu 90 °C and U400/PSS250/Cu 550 °C.

The results of the Cu 2p region (Figure 4-17a) revealed that satellite peaks (940–946 eV and 960–965 eV) derived from Cu^{2+} (CuO) were present in U400/PSS250/Cu 550 °C.[36] The Auger parameters were calculated using the Cu $2p_{3/2}$ photoelectron peaks (Figure 4-17a) and the Cu $L_3M_{4,5}M_{4,5}$ Auger peaks (Figure 4-18).[37,38] The Auger parameters (Table 4-1) in $Cu(OAc)_2 \cdot H_2O$ 550 °C (1851.6 eV) and U400/PSS250/Cu 550 °C (1851.8 eV) were close to those of CuO (1851.5 eV) rather than Cu_2O (1849.2 eV),[38] which supports the XRD results and CuO formation. In U400/PSS250/Cu 90 °C, the value (1848.5 eV) was close to that of the Cu^+ compound, such Cu_2O (1849.2 eV), indicating that Cu^{2+} species in $Cu(OAc)_2 \cdot H_2O$ may be reduced to Cu^+ species by the amino groups in U400. U400 removal was verified using the spectra in the N 1s region (Figure 4-17b). According to the comparison of the spectra between U400/PSS250/Cu 90 °C and U400/PSS250/Cu 550 °C, although the peak derived from carbon nitride was confirmed in U400/PSS250/Cu 90 °C, the peak was not detected in U400/PSS250/Cu 550 °C. Accordingly, N (carbon nitride) was removed during calcination. SiO_2 formation was analyzed using XPS and ^{29}Si MAS NMR.XPS spectra in the Si 2p region are shown in Figure 4-17c. Si peaks were detected in U400/PSS250/Cu 90 °C and U400/PSS250/Cu 550 °C. However, the peak positions were different. Compared with the peak position of U400/PSS250/Cu 90 °C (102.3 eV), the peak position of U400/PSS250/Cu 550 °C (104.2 eV) shifted to a higher binding energy. Kaur et al. reported that the peaks at 102.7 eV and 103.7 eV corresponded to Si–O (as well as Si–O–C) bonds and SiO_2, respectively,[18] indicating that SiO_2 formation was induced by calcination at 550 °C. ^{29}Si MAS NMR spectrum in U400/PSS250/Cu 550 °C (Figure 4-17d) detected two SiO_2 components: a main component at −112 ppm and a shoulder structure at −102 ppm. These components were assigned to the Q^4 and Q^3 sites of the SiO_4 structure, respectively.[39,40] The ratio of Q^4 and Q^3 was estimated to be 4.9:1, indicating that fully condensed sites were abundant and supporting the SiO_2 formation.

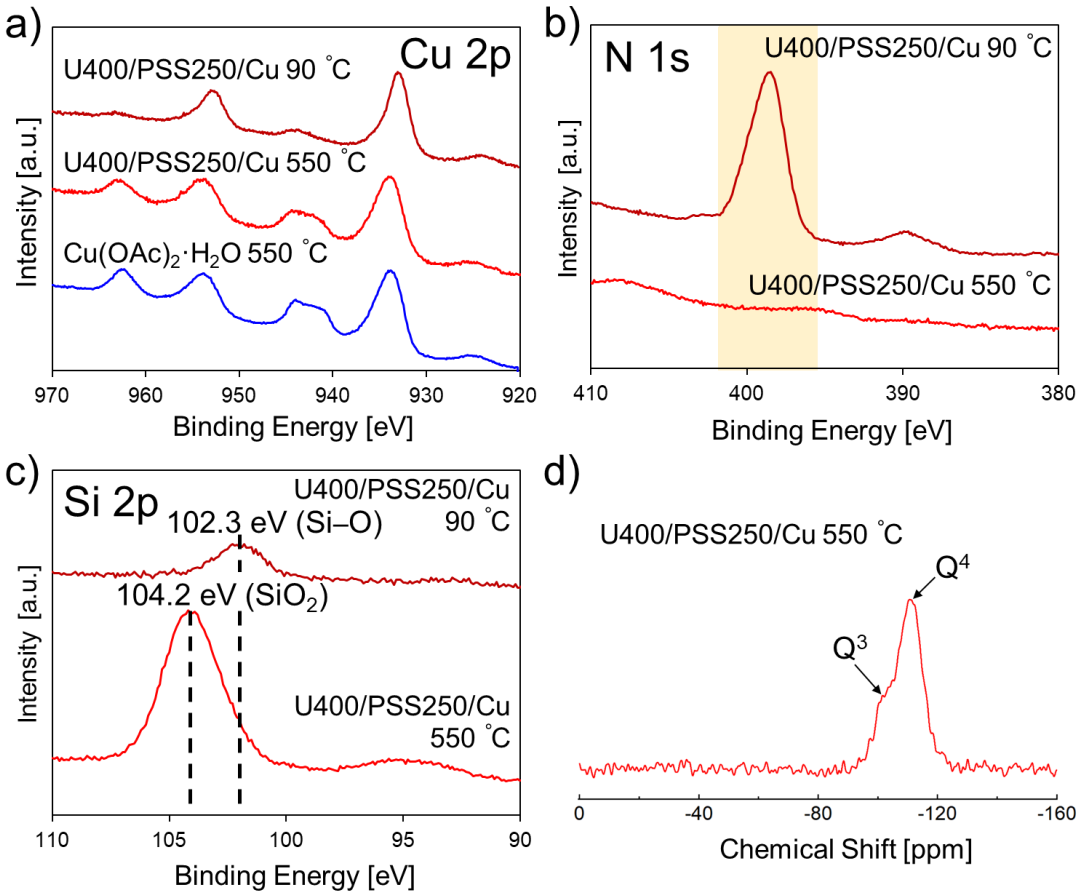

Figure 4-17. High-resolution XPS spectra in a) the Cu 2p region for U400/PSS250/Cu 90 °C, U400/PSS250/Cu 550 °C, and $Cu(OAc)_2 \cdot H_2O$ 550 °C; b) the N 1s region; and c) the Si 2p region for U400/PSS250/Cu 90 °C and U400/PSS250/Cu 550 °C. d) ^{29}Si MAS NMR spectrum of U400/PSS250/Cu 550 °C.

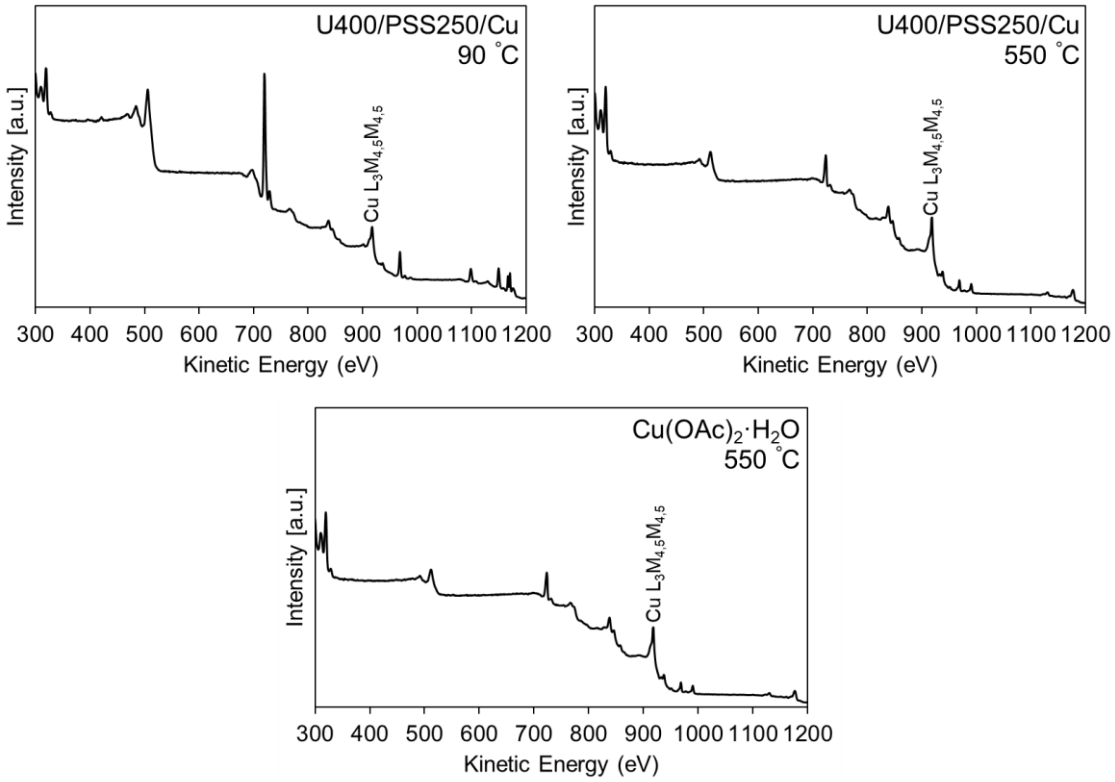

Figure 4-18. XPS survey scan for U400/PSS250/Cu 90 °C, U400/PSS250/Cu 550 °C, and $Cu(OAc)_2 \cdot H_2O$ 550 °C in the kinetic energy scale.

Table 4-1. Calculated Auger parameters.

	Cu $2p_{3/2}$ photoelectron peak [eV]	**Cu $L_3M_{4,5}M_{4,5}$ Auger peak [eV]**	**Auger parameter [eV]**
U400/PSS250/Cu 90 °C	933.04	915.44	1848.5
U400/PSS250/Cu 550 °C	934.08	917.70	1851.8
$Cu(OAc)_2 \cdot H_2O$ 550 °C	933.59	918.05	1851.6

EDX was performed to obtain the Si and Cu ratios, and the results are shown in Tables 4-2, 4-3, and 4-4. The element ratios of Si and Cu in U400/PSS250/Cu 550 °C, U400/PSS500/Cu 550 °C, and U400/PSS1500/Cu 550 °C were 46:54, 37:63, 48:52, respectively; the values of U400/PSSx/Cu 550 °C were relatively close. The experimental yields in U400/PSS250/Cu 550 °C, U400/PSS500/Cu 550 °C, and U400/PSS1500/Cu 550 °C were 11.7, 19.3, and 30.3%, respectively. The experimental yields were close to the theoretical CuO and SiO_2 yields (Table 4-5), indicating that U400/PSSx/Cu 550 °C mainly contained CuO and SiO_2.

Table 4-2. The element ratio of Si and Cu in U400/PSS250/Cu 550 °C.

	1	2	3	4	5	
Si [at%]	43.81	44.41	38.32	46.58	46.77	
Cu [at%]	56.19	55.59	61.68	53.42	53.23	
	6	**7**	**8**	**9**	**10**	**Average**
Si [at%]	46.86	48.01	50.91	45.75	47.33	45.9
Cu [at%]	53.14	51.99	49.09	54.25	52.67	54.1

Table 4-3. The element ratio of Si and Cu in U400/PSS500/Cu 550 °C.

	1	2	3	4	5	
Si [at%]	36.77	38.36	29.14	39.30	44.05	
Cu [at%]	63.23	61.64	70.86	60.70	55.95	
	6	**7**	**8**	**9**	**10**	**Average**
Si [at%]	34.01	30.60	29.61	45.96	45.46	37.3
Cu [at%]	65.99	69.40	70.39	54.04	54.54	62.7

Table 4-4. The element ratio of Si and Cu in U400/PSS1500/Cu 550 °C.

	1	2	3	4	5	
Si [at%]	53.07	48.86	48.00	41.55	44.20	
Cu [at%]	46.93	51.14	52.00	58.45	55.80	
	6	**7**	**8**	**9**	**10**	**Average**
Si [at%]	42.88	50.68	53.35	47.46	49.10	47.9
Cu [at%]	57.12	49.32	46.65	52.54	50.90	52.1

Table 4-5. Experimental yields of U400/PSSx/Cu 550 °C and theoretical yields of CuO and SiO_2.

Product name	**Precursors (U400/PSSx/Cu 90 °C) [mg]**	**Products (U400/PSSx/Cu 550 °C) [mg]**	**Experimental yield [%]**	**Theoretical yield of CuO and SiO_2 [%]**
U400/PSS250/Cu 550 °C	987	115	11.7	15.5
U400/PSS500/Cu 550 °C	1449	280	19.3	22.5
U400/PSS1500/Cu 550 °C	1705	516	30.3	32.3

According to the XRD patterns, XPS spectra, and the element ratios of Si and Cu, the CuO–SiO_2 nanocomposites were fabricated via the calcination of U400/Cu^{2+}/POSS mixtures (U400/PSSx/Cu 90 °C) inducing SiO_2 and CuO formation and carbon nitride removal.

The morphologies of the CuO–SiO_2 nanocomposites were analyzed using SEM. The SEM images of U400/PSSx/Cu 550 °C are shown in Figure 4-19. U400/PSSx/Cu 550 °C had a fluffy structure. Microstructure and elemental mapping were obtained using TEM and STEM-EDX measurements (Figure 4-20). TEM and STEM images and EDX elemental mappings in

U400/PSS250/Cu 550 °C and U400/PSS1500/Cu 550 °C indicate that SiO_2 had a fluffy structure and SiO_2 supported CuO. The preferential formation of fluffy SiO_2 compared with CuO might result from the possible number of interactions between carbon nitride (U400) and precursors of SiO_2 and CuO (PSS and $Cu(OAc)_2 \cdot H_2O$). PSS had a greater possible number of sites that could interact with U400 per molecule rather than $Cu(OAc)_2 \cdot H_2O$, indicating that PSS was greatly influenced by the structure-directing effect of U400.

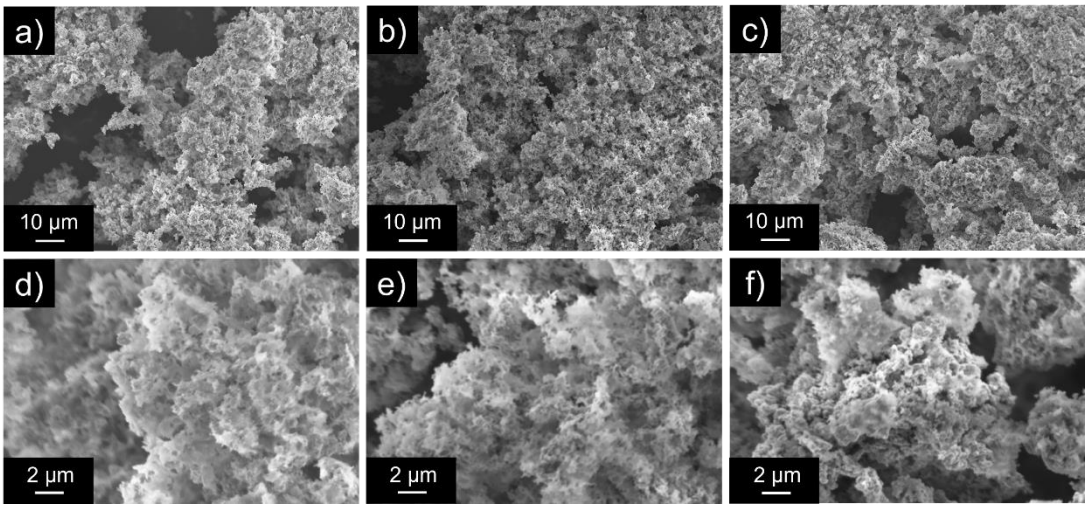

Figure 4-19. SEM images of U400/PSS250/Cu 550 °C (a, d), U400/PSS500/Cu 550 °C (b, e), and U400/PSS1500/Cu 550 °C (c, f).

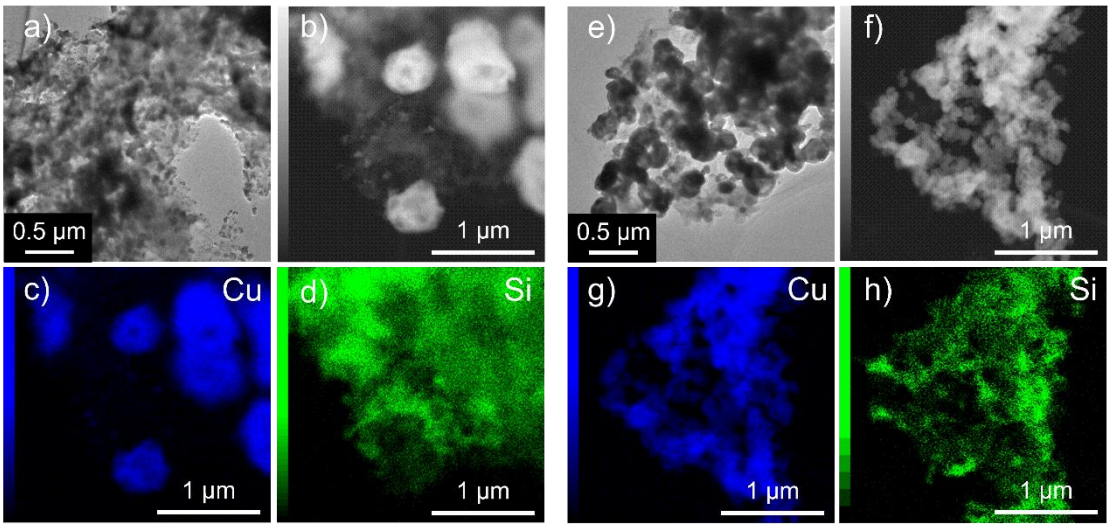

Figure 4-20. TEM images of U400/PSS250/Cu 550 °C (a) and U400/PSS1500/Cu 550 °C (e).

STEM images and EDX elemental mappings of U400/PSS250/Cu 550 °C (b−d) and U400/PSS1500/Cu 550 °C (f−h).

The porosity of the CuO–SiO_2 nanocomposites was measured using N_2 adsorption–desorption tests. The N_2 adsorption–desorption isotherms are shown in Figure 4-21. The isotherm types of U400/PSSx/Cu 550 °C were assigned to lV(a), representing the presence of mesopores.[41] In addition, according to isotherms and pore size distributions obtained using the BJH method (Figure 4-22), U400/PSSx/Cu 550 °C had a pore structure comprising micropores and small mesopores (<10 nm). S_{BET} of U400/PSS250/Cu 550 °C, U400/PSS500/Cu 550 °C, and U400/PSS1500/Cu 550 °C were 157, 153, and 214 $m^2\ g^{-1}$, respectively. S_{BET} of U400/PSS1500/Cu 550 °C was higher than those of U400/PSS250/Cu 550 °C and U400/PSS500/Cu 550 °C. This change might result from an increase in the concentration of Cu^{2+}/POSS in the U400/Cu^{2+}/POSS mixtures or the structural differences of the U400/Cu^{2+}/POSS mixtures (U400/PSSx/Cu 90 °C) confirmed using XRD (Figure 4-13). Furthermore, U400/PSSx/Cu 550 °C had higher specific surface areas than $Cu(OAc)_2 \cdot H_2O$ 550°C (1 $m^2\ g^{-1}$). Compared with porous (nanoporous) CuO and CuO–SiO_2 composites [which contain high Cu or CuO content (>25 wt%)] in a previous study (Table 4-6),[42−50] the developed U400/PSSx/Cu 550 °C had a relatively higher value of specific surface area.

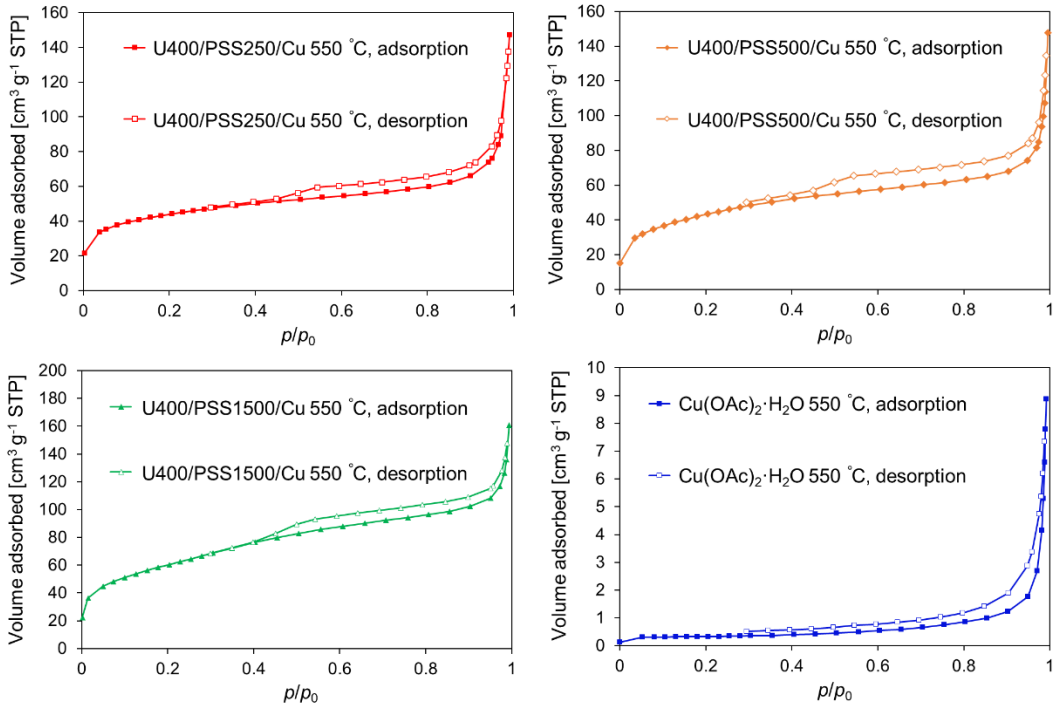

Figure 4-21. N_2 adsorption–desorption isotherms of U400/PSSx/Cu 550 °C and $Cu(OAc)_2 \cdot H_2O$ 550 °C.

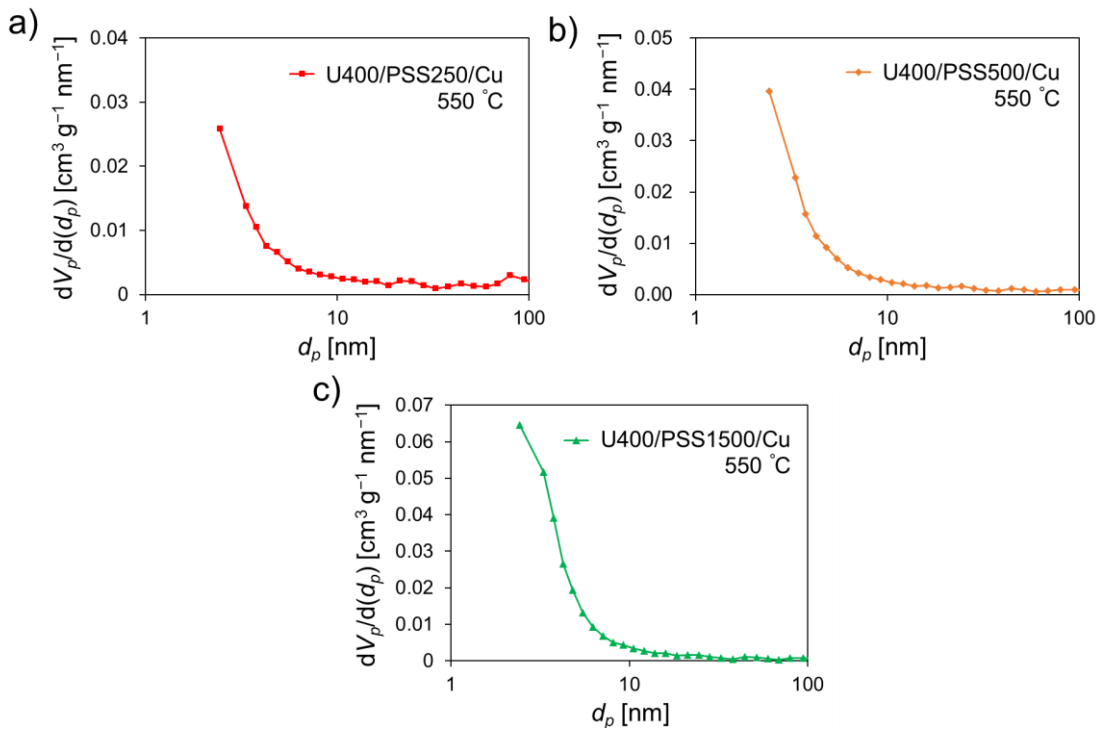

Figure 4-22. BJH pore size distributions of a) U400/PSS250/Cu 550 °C, b) U400/PSS500/Cu 550 °C, and c) U400/PSS1500/Cu 550 °C.

Table 4-6. Comparative table from the literature on porosity.

	Method	**Specific surface area [m^2 g^{-1}]**	**Ref.**
CuO nanochains	Wet chemical route using polyethylene glycol as a soft template	123.1	42
CuO nanosheet clusters	Hydrothermal method with/without surfactants	75.40, 95.31, 93.87	43
CuO hollow microspheres	Carbon spheres used as templates	74.81	44
Porous CuO	Calcination of MOF	69.57, 89.18	45
CuO ultrathin nanobelts	The wet chemical method combined with a fast calcination strategy	109.13	46
Mesoporous CuO dandelion structures	Hydrothermal route	325	47
Porous CuO	Calcination process via chemical solution deposition to prepare the copper oxalate precursor	165, 193, 295	48
CuO/SiO_2 composites	Solution exchange of wet silica gel (CuO content: 30 wt%)	158	49
Hollow CuO@SiO_2 spheres	Templated synthesis using Cu@C composite as a hard template (Cu content: 26 wt%)	85	50
Nanoporous CuO–SiO_2 nanocomposites	Structure-directing synthesis via calcination using carbon nitride	153, 157, 214	This study

The optical properties (band gaps) of the nanocomposites were analyzed using UV–vis absorption spectra. Figure 4-23 shows that U400/PSS500/Cu 550 °C and U400/PSS1500/Cu 550 °C exhibited high visible-light absorption properties and similar spectra. The shapes of the spectra were close to the shape of $Cu(OAc)_2 \cdot H_2O$ 550 °C (pristine CuO). The optical band gaps were calculated using the Tauc approach (Figure 4-24).[19,20] The band gaps of U400/PSS500/Cu 550 °C and U400/PSS1500/Cu 550 °C were 1.32 and 1.31 eV, respectively, which were close to the band gap of $Cu(OAc)_2 \cdot H_2O$ 550 °C (1.24 eV). Slight increases in the band gaps of U400/PSSx/Cu 550 °C might result from the introduction of SiO_2 or differences in the crystal growth of CuO. According to the literature (Table 4-7),[51–55] the band gap values of U400/PSSx/Cu 550 °C were relatively close to those of other CuO composite materials. Given the SEM results, N_2 adsorption–desorption tests, and UV–vis absorption spectra, nanoporous CuO–SiO_2 nanocomposites with unique morphologies (e.g., fluffy structures), high surface areas, and narrow optical band gaps were constructed.

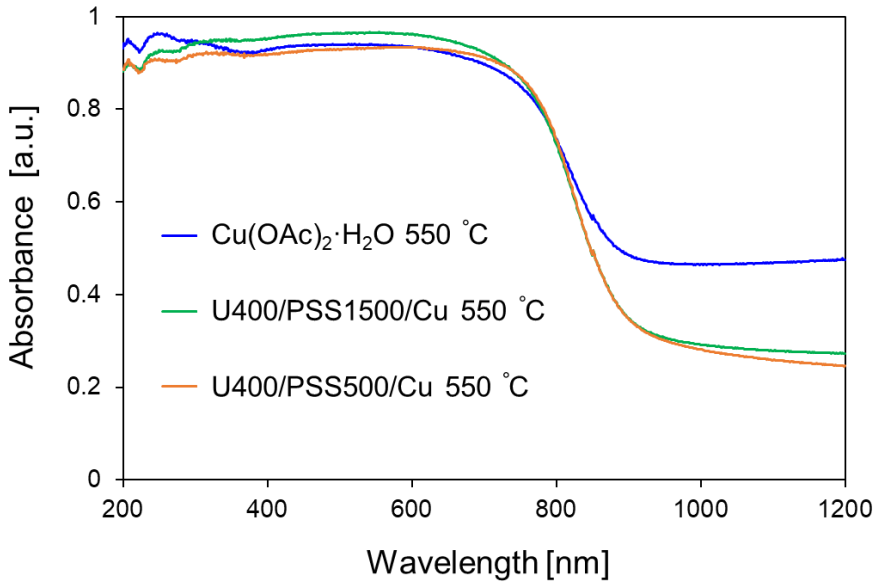

Figure 4-23. UV–vis absorption spectra of U400/PSS500/Cu 550 °C, U400/PSS1500/Cu 550 °C, and $Cu(OAc)_2 \cdot H_2O$ 550 °C.

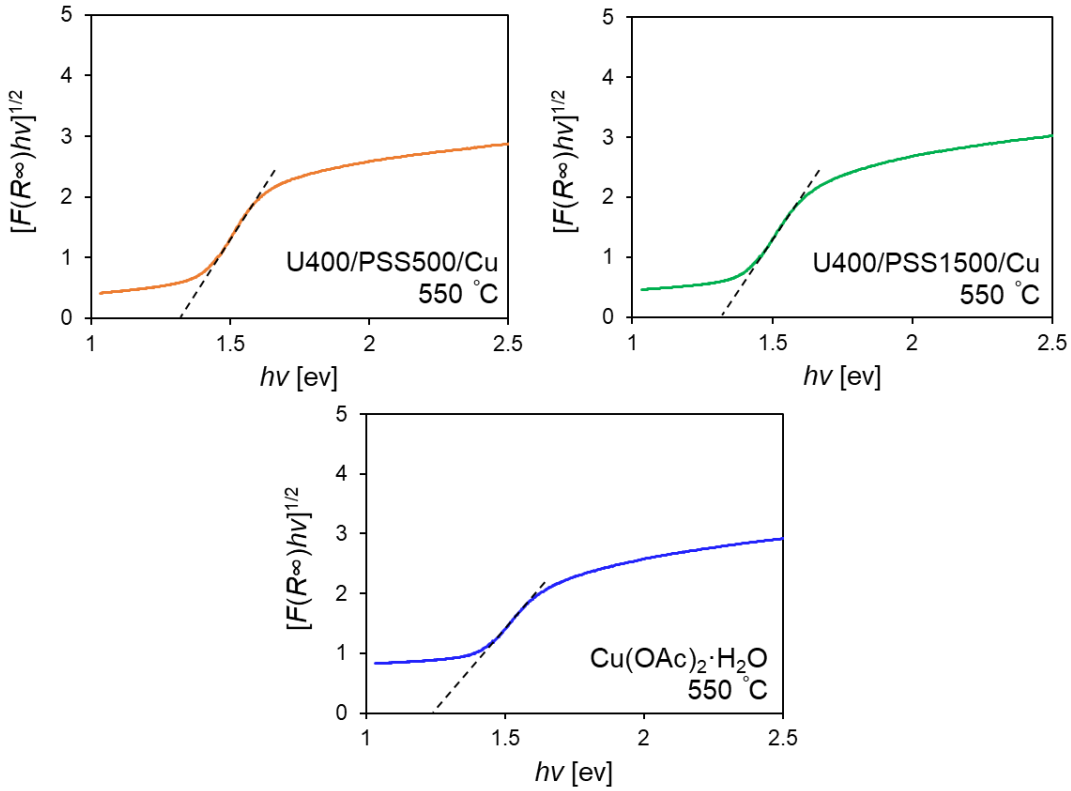

Figure 4-24. Optical band gaps of U400/PSS500/Cu 550 °C, U400/PSS1500/Cu 550 °C, and $Cu(OAc)_2 \cdot H_2O$ 550 °C determined with the plots of $[F(R\infty)hv]^{1/2}$ *versus* photon energy (hv).

Table 4-7. Comparative table from the literature in the band gap.

	Band gap [eV]	**Ref.**
CuO–ZnO core–shell nanowire	1.5–1.6	51
CuO@TiO_2 heterostructure composite	2.35	52
CuO/$CuFe_2O_4$ nanocomposites	1.37–1.72	53
Core–shell nanoparticles of SiO_2@CuO	2.63–4.20	54
CuO–SiO_2 monolith	1.33	55
Nanoporous CuO–SiO_2 nanocomposites	1.3	This study

Given their unique morphologies, high specific surface areas, and narrow band gaps, the synthesized CuO–SiO_2 nanocomposites can be applied to adsorption–separation applications and used as catalysts. CO_2 adsorption tests were performed at 303 K, and the isotherms are shown in Figure 4-25. Compared to the CO_2 uptake of $Cu(OAc)_2 \cdot H_2O$ 550 °C (0.0056 mmol g^{-1}), that of U400/PSS1500/Cu 550 °C (0.21 mmol g^{-1}) was enhanced because of the improved porosity, indicating performance improvement in the application of CO_2 capture and/or utilization.

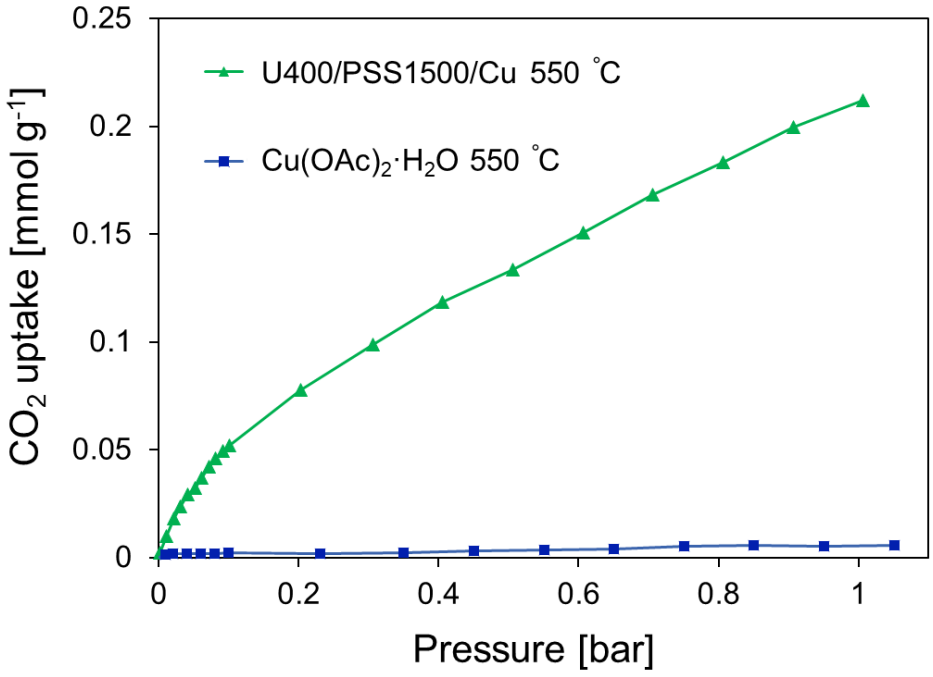

Figure 4-25. CO_2 adsorption isotherms of U400/PSS1500/Cu 550 °C and $Cu(OAc)_2 \cdot H_2O$ 550 °C.

4-2-3-2. Elucidation of the formation factors

The formation factors of nanoporous CuO–SiO_2 nanocomposites were elucidated through comparative experiments to investigate the roles of Cu^{2+}, POSS, and carbon nitride. First, the SiO_2 formation was discussed. The ratio of Si to Cu in the nanoporous CuO–SiO_2 nanocomposites (U400/PSSx/Cu 550 °C) was almost 1:1 (Tables 4-2, 4-3, and 4-4). In contrast, PSS/Cu 550 °C, prepared without adding U400, exhibited a lower Si ratio than U400/PSSx/Cu 550 °C (Table 4-8), indicating that carbon nitride (U400) suppressed POSS removal and induced SiO_2 formation.

Table 4-8. The element ratio of Si and Cu in PSS/Cu 550 °C.

	1	2	3	4	5	
Si [at%]	0	0	0	11.48	7.39	
Cu [at%]	100	100	100	88.52	92.61	
	6	**7**	**8**	**9**	**10**	**Average**
Si [at%]	0	0	6.61	10.06	4.77	4.03
Cu [at%]	100	100	93.39	89.94	95.23	95.97

Second, carbon nitride removal was investigated using U400/Cu 550 °C, prepared without adding PSS, and U400/PSS 550°C, prepared without adding $Cu(OAc)_2 \cdot H_2O$. U400/Cu 550°C exhibited no peak around 399 eV in the XPS spectra (Figure 4-26a), and the peak derived from carbon nitride remained in U400/PSS 550 °C (Figure 4-26b). These results reveal that N (carbon nitride) removal was induced by the effect of Cu species.

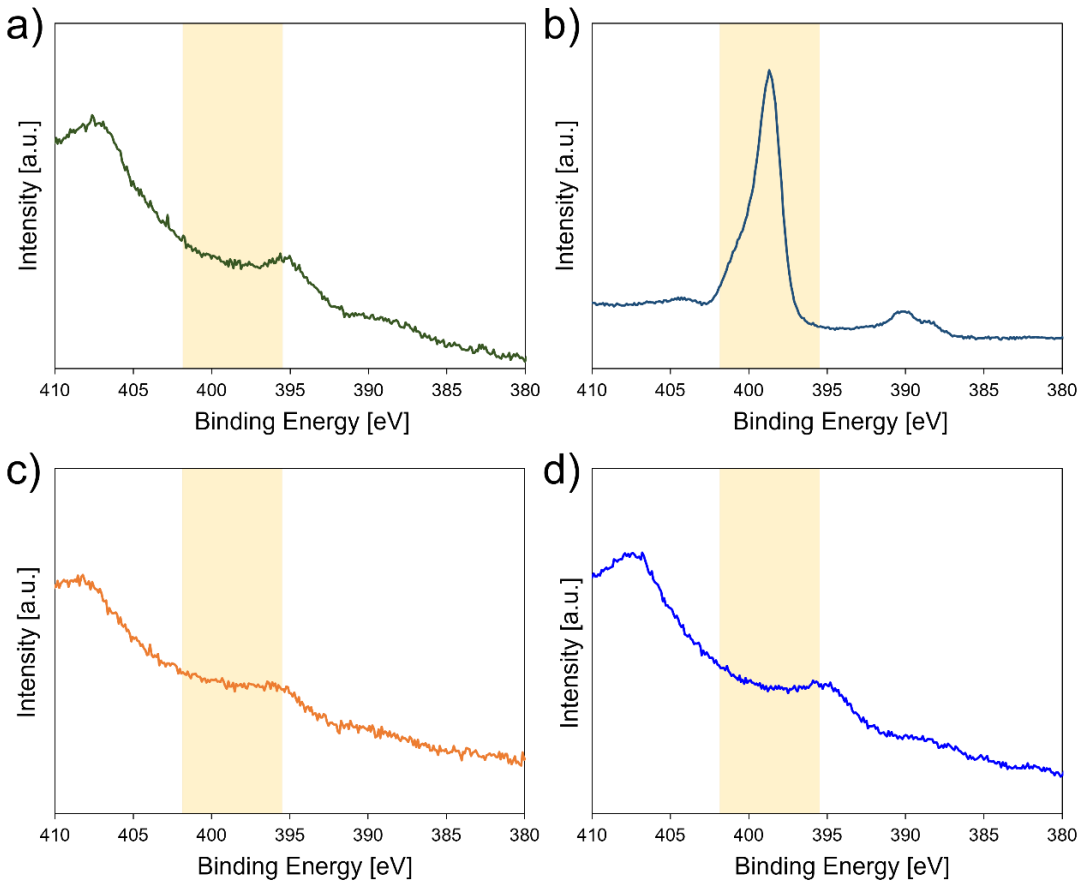

Figure 4-26. High-resolution XPS spectra in the N 1s region for a) U400/Cu 550 °C, b) U400/PSS 550 °C, c) U400/PSS500/Cu 550 °C, and d) the background [$Cu(OAc)_2 \cdot H_2O$ 550°C].

Third, the factors determining morphology and porosity were examined. The SEM images revealed that rigid structures were confirmed in PSS/Cu 550 °C, U400/Cu 550 °C, and $Cu(OAc)_2 \cdot H_2O$ 550 °C; however, fluffy structures, which were observed in U400/PSSx/Cu 550 °C, could not be observed (Figure 4-27 and 4-28). Furthermore, in terms of porosity, the N_2-adsorbed volume of U400/Cu 550 °C (Figure 4-29) was extremely smaller than that of U400/PSSx/Cu 550 °C. Accordingly, the SiO_2 formation process induced by carbon nitride played a vital role in the porosity enhancement of U400/PSSx/Cu 550 °C.

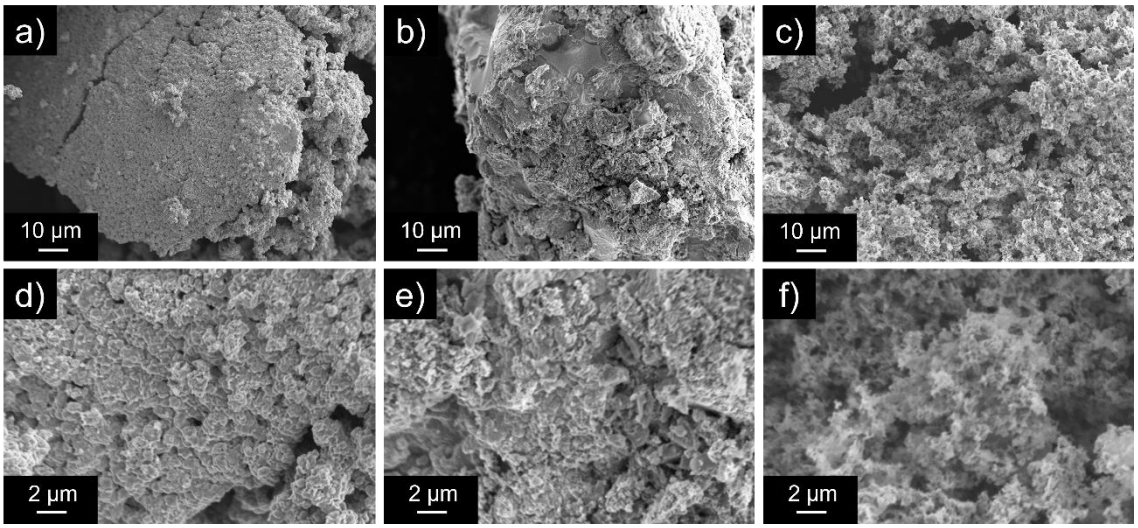

Figure 4-27. SEM images of U400/Cu 550 °C (a, d), PSS/Cu 550 °C (b, e), and U400/PSS500/Cu 550 °C, in which the location was different from Figure 4-19b and 4-19e (c, f).

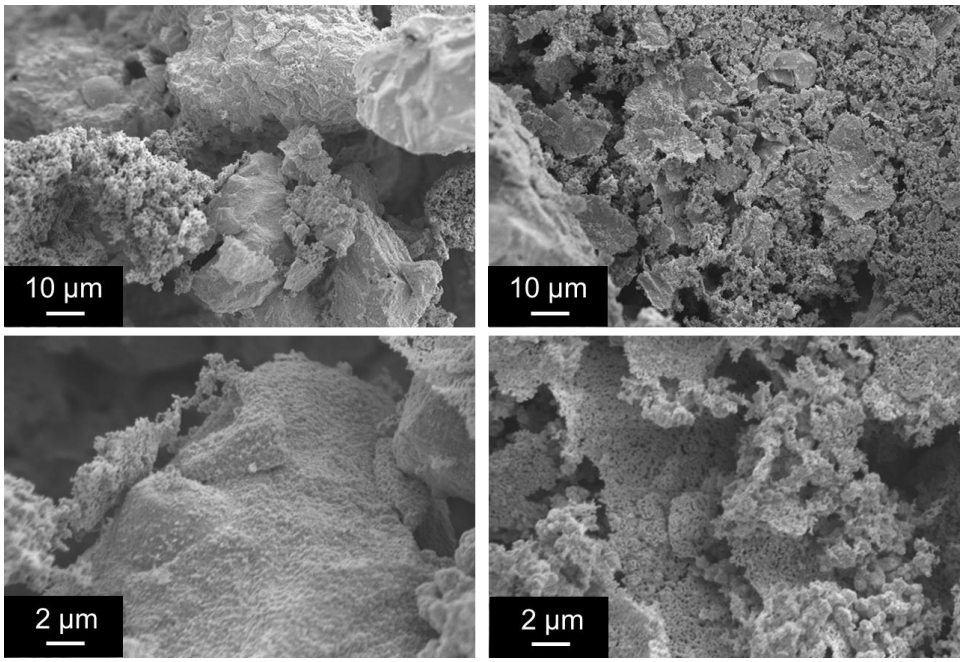

Figure 4-28. SEM images of $Cu(OAc)_2 \cdot H_2O$ 550 °C.

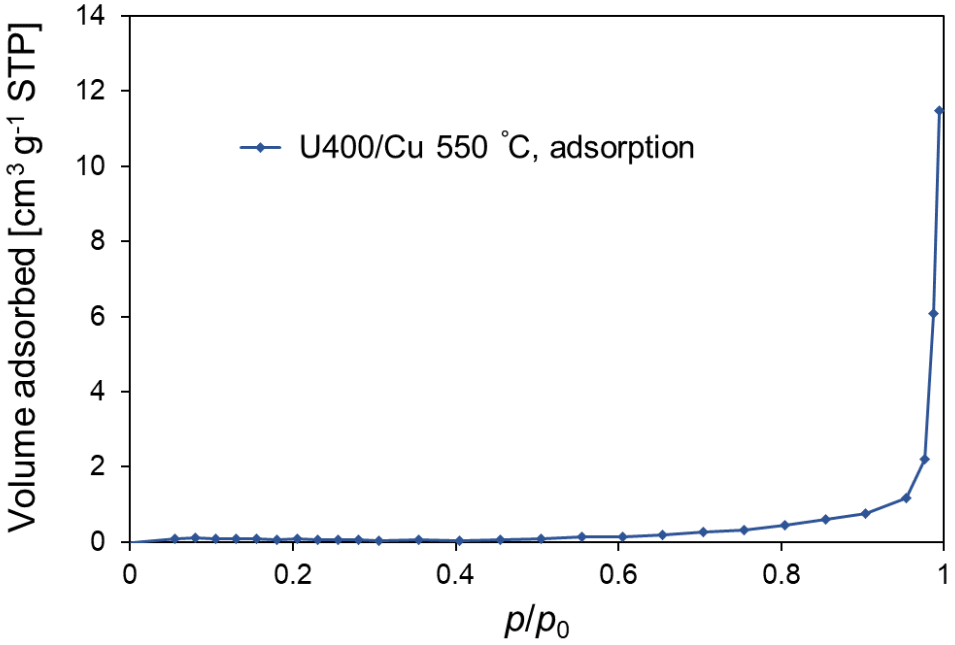

Figure 4-29. The N_2 adsorption isotherm of U400/Cu 550 °C.

According to the results of EDX, SEM, and N_2 adsorption–desorption tests, nanoporous CuO–SiO_2 nanocomposites with a fluffy structure and high surface areas were constructed owing to the structural control of CuO through the SiO_2 formation process induced by carbon nitride rather than the individual effects of U400 and PSS.

Finally, the effects of the calcination temperature were investigated. According to the Cu 2p region (Figure 4-30a), the sample peak shape [peak position and satellite peaks (940–946 and 960–965 eV) derived from Cu^{2+} (CuO)] after calcination at a temperature exceeding 400 °C was close to that of U400/PSS1500/Cu 550 °C, indicating that CuO was formed between 200 °C and 400 °C. In the N 1s region (Figure 4-30b), the peak derived from carbon nitride completely disappeared in U400/PSS1500/Cu 550 °C (0 h) after CuO formation. In addition, with an increase in the calcination temperature, the peak positions in the Si 2p region (Figure 4-30c) gradually shifted to the higher binding energy side, indicating that SiO_2 formation gradually occurred while increasing the temperature and retaining it at 550 °C.

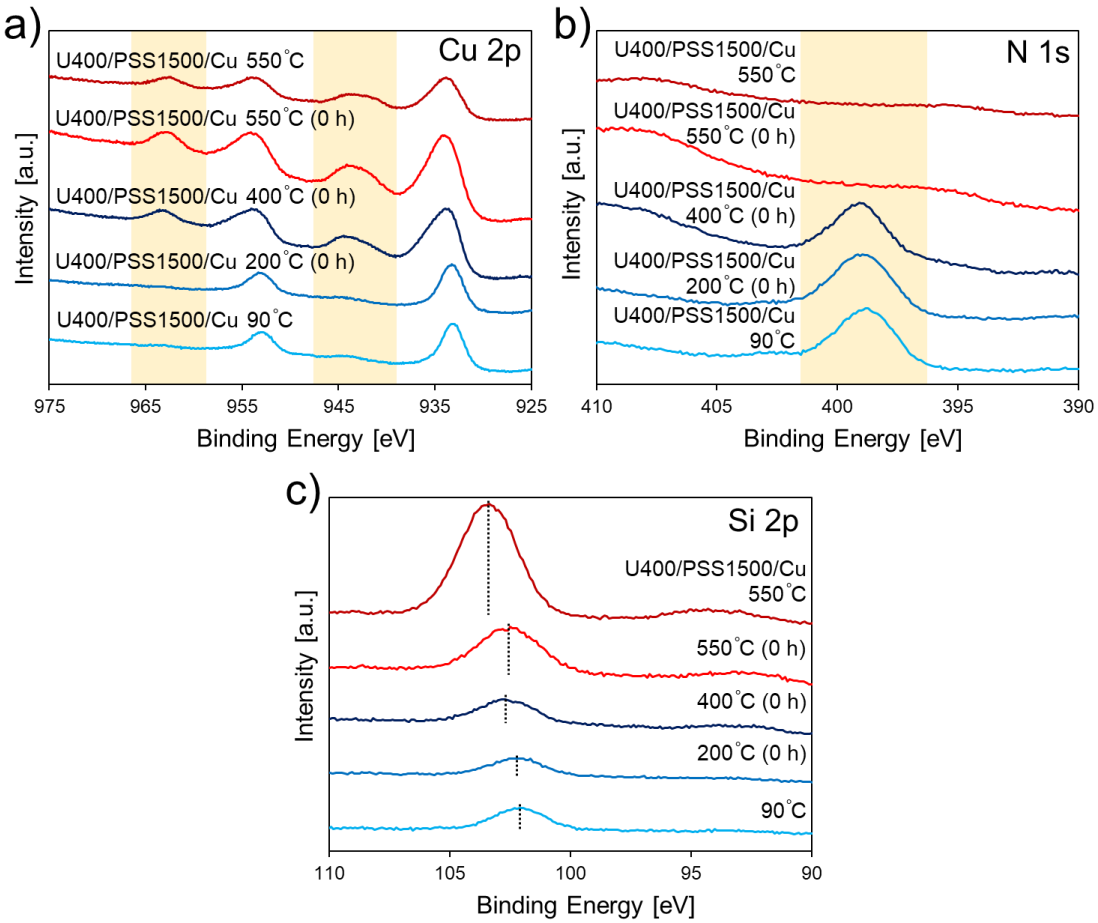

Figure 4-30. High-resolution XPS spectra in a) the Cu 2p region, b) the N 1s region, and c) the Si 2p region for U400/PSS1500/Cu 90 °C and the samples obtained by calcining U400/PSS1500/Cu 90 °C at different conditions.

The results indicate that the proposed formation processes of the fluffy nanoporous CuO–SiO_2 nanocomposites can be described as follows:

a) Carbon nitride (U400) suppressed POSS removal and induced SiO_2 formation, and fluffy SiO_2 supported CuO.

b) Carbon nitride was removed by the effect of Cu species (e.g., CuO) during calcination, and the fluffy nanoporous CuO–SiO_2 nanocomposites were synthesized.

This study developed fluffy nanoporous CuO–SiO_2 nanocomposites by controlling the CuO and SiO_2 formation using carbon nitride as a structure-directing agent. Previously, two-dimensional materials were used as the template for various materials (e.g., SiO_2 and metal oxide).[23–25] However, carbon nitride could not control the CuO structure (morphology and porosity) by itself in this synthesis system; the SiO_2 formation process induced by carbon nitride controlled the structure of CuO (–SiO_2 nanocomposites), and fluffy nanoporous CuO–SiO_2 nanocomposites were fabricated. According to this study, the synthesis method using the SiO_2 formation process induced by carbon nitride (two-dimensional materials) in the presence of the precursor may control the structure of the desired materials, which cannot be controlled by two-dimensional materials alone (although SiO_2 remains in the product). Furthermore, regarding the synthesis process, the method used in this study concurrently induced CuO and SiO_2 formation. The synthesis method simultaneously forming CuO and SiO_2 may reduce the number of steps of substance formation compared to two-step formation processes, such as CuO modification after the synthesis of porous (nanoporous) silica. This study contributes to the exploration of structural control and synthesis technology in solid-state materials.

4-2-4. Conclusion

Nanoporous CuO–SiO_2 nanocomposites with high surface areas and unique morphologies were developed by calcining a mixture of Cu^{2+}, POSS, and carbon nitride, which was used as a structure-directing agent to control the structure of the CuO–SiO_2 nanocomposites. Carbon nitride suppressed POSS removal and induced SiO_2 formation in the nanoporous CuO–SiO_2 nanocomposites. The formed SiO_2 exhibited a fluffy structure that supported CuO. Carbon nitride was removed by the effect of Cu species (e.g., CuO), and nanoporous CuO–SiO_2 nanocomposites were developed. Changing the Cu^{2+}/POSS mixture to the carbon nitride ratio in the Cu^{2+}/POSS/carbon nitride mixture changed the porosity of the nanoporous CuO–SiO_2 nanocomposites. The synthesized nanoporous CuO–SiO_2 nanocomposites, with narrow optical band gaps, have potential applications as adsorbents and catalysts. The constructed materials and the proposed synthesis method may contribute to the development of porous (nanoporous)

materials and their applications as adsorbents and catalysts.

The content of this section was adapted with permission from the following paper:

Takeuchi, Y.; Toyoda, Y.; Gotoh, K.; Ohkubo, T. Structure-Directing Synthesis of Porous CuO–SiO_2 Nanocomposites Using Carbon Nitride. *CrystEngComm* **2024**, *26*, 3044-3053. (© 2024 The Royal Society of Chemistry)

https://doi.org/10.1039/D4CE00183D

4-3. References

(1) Zhang, J.-H.; Wei, M.-J.; Wei, Z.-W.; Pan, M.; Su, C.-Y. Ultrathin Graphitic Carbon Nitride Nanosheets for Photocatalytic Hydrogen Evolution. *ACS Appl. Nano Mater.* **2020**, *3*, 1010–1018.

(2) Gao, J.; Wang, Y.; Zhou, S.; Lin, W.; Kong, Y. A Facile One-Step Synthesis of Fe-Doped g-C_3N_4 Nanosheets and Their Improved Visible-Light Photocatalytic Performance. *ChemCatChem* **2017**, *9*, 1708–1715.

(3) Kuriki, R.; Sekizawa, K.; Ishitani, O.; Maeda, K. Visible-Light-Driven CO_2 Reduction with Carbon Nitride: Enhancing the Activity of Ruthenium Catalysts. *Angew. Chem. Int. Ed.* **2015**, *54*, 2406–2409.

(4) Tang, H.; Xia, Z.; Chen, R.; Liu, Q.; Zhou, T. Oxygen Doped g-C_3N_4 with Nitrogen Vacancy for Enhanced Photocatalytic Hydrogen Evolution. *Chem. Asian J.* **2020**, *15*, 3456–3461.

(5) Liang, Q.; Li, Z.; Huang, Z.-H.; Kang, F.; Yang, Q.-H. Holey Graphitic Carbon Nitride Nanosheets with Carbon Vacancies for Highly Improved Photocatalytic Hydrogen Production. *Adv. Funct. Mater.* **2015**, *25*, 6885–6892.

(6) Goettmann, F.; Fischer, A.; Antonietti, M.; Thomas, A. Chemical Synthesis of Mesoporous Carbon Nitrides Using Hard Templates and Their Use as a Metal-Free Catalyst for Friedel–Crafts Reaction of Benzene. *Angew. Chem. Int. Ed.* **2006**, *45*, 4467–4471.

(7) Yan, Z.; Yang, M.; Chen, Y.; Li, T.; Jing, Q.; Liu, P. Hydroxyl-Rich Porous Silica Nanosheets Decorated with Oxygen-Doped Carbon Nitride Nanoparticles for Photocatalytic Degradation of Rhodamine B. *ACS Appl. Nano Mater.* **2022**, *5,* 818–831.

(8) Yan, S. C.; Li, Z. S.; Zou, Z. G. Photodegradation of Rhodamine B and Methyl Orange over Boron-Doped g-C_3N_4 under Visible Light Irradiation. *Langmuir* **2010**, *26*, 3894–3901.

(9) Wang, K.; Li, Q.; Liu, B.; Cheng, B.; Ho, W.; Yu, J. Sulfur-Doped g-C_3N_4 with Enhanced Photocatalytic CO_2-Reduction Performance. *Appl. Catal. B* **2015**, *176–177*, 44–52.

(10) Tao, K.-Y.; Yuan, K.; Yang, W.; Zhong, D.-C.; Lu, T.-B. A Template Co-Pyrolysis Strategy towards the Increase of Amino/Imino Content within g-C_3N_4 for Efficient CO_2 Photoreduction. *Chem. Eng. J.* **2023**, *455*, 140630.

(11) Fan, X.; Zhang, L.; Cheng, R.; Wang, M.; Li, M.; Zhou, Y.; Shi, J. Construction of Graphitic C_3N_4-Based Intramolecular Donor–Acceptor Conjugated Copolymers for Photocatalytic Hydrogen Evolution. *ACS Catal.* **2015**, *5*, 5008–5015.

(12) Zhao, S.; Zhang, Y.; Wang, Y.; Zhou, Y.; Qiu, K.; Zhang, C.; Fang, J.; Sheng, X. Ionic Liquid-Assisted Synthesis of Br-Modified g-C_3N_4 Semiconductors with High Surface Area and Highly Porous Structure for Photoredox Water Splitting. *J. Power Sources* **2017**, *370*, 106–113.

(13) Fang, H.-B.; Luo, Y.; Zheng, Y.-Z.; Ma, W.; Tao, X. Facile Large-Scale Synthesis of Urea-Derived Porous Graphitic Carbon Nitride with Extraordinary Visible-Light Spectrum Photodegradation. *Ind. Eng. Chem. Res.* **2016**, *55*, 4506–4514.

(14) Ge, L. Synthesis and Photocatalytic Performance of Novel Metal-Free g-C_3N_4 Photocatalysts. *Mater. Lett.* **2011**, *65*, 2652–2654.

(15) Katsumata, H.; Sakai, T.; Suzuki, T.; Kaneco, S. Highly Efficient Photocatalytic Activity of g-C_3N_4/Ag_3PO_4 Hybrid Photocatalysts through Z-Scheme Photocatalytic Mechanism under Visible Light. *Ind. Eng. Chem. Res.* **2014**, *53*, 8018–8025.

(16) Lee, M.-S.; Park, M.; Kim, H. Y.; Park, S.-J. Effects of Microporosity and Surface Chemistry on Separation Performances of N-Containing Pitch-Based Activated Carbons for CO_2/N_2 Binary Mixture. *Sci. Rep.* **2016**, *6*, 23224.

(17) Bao, Y.; Chen, K. AgCl/Ag/g-C_3N_4 Hybrid Composites: Preparation, Visible Light-Driven Photocatalytic Activity and Mechanism. *Nanomicro Lett.* **2016**, *8*, 182–192.

(18) Kaur, A.; Chahal, P.; Hogan, T. Selective Fabrication of SiC/Si Diodes by Excimer Laser Under Ambient Conditions. *IEEE Electron Device Lett.* **2016**, *37*, 142–145.

(19) Suchanicz, J.; Konieczny, K.; Świerczek, K.; Lipiński, M.; Karpierz, M.; Sitko, D.; Czternastek, H.; Kluczewska, K. Electrical Transport in Low-Lead $(1-x)BaTiO_3$–$xPbMg_{1/3}Nb_{2/3}O_3$ Ceramics. *J. Adv. Ceram.* **2017**, *6*, 207–219.

(20) Wu, D.; Che, Q.; He, H.; El-Khouly, M. E.; Huang, S.; Zhuang, X.; Zhang, B.; Chen, Y. Room-Temperature Interfacial Synthesis of Vinylene-Bridged Two-Dimensional Covalent Organic Framework Thin Film for Nonvolatile Memory. *ACS Materials Lett.* **2023**, *5*, 874–

883.

(21) Makuła, P.; Pacia, M.; Macyk, W. How To Correctly Determine the Band Gap Energy of Modified Semiconductor Photocatalysts Based on UV–Vis Spectra. *J. Phys. Chem. Lett.* **2018**, *9*, 6814–6817.

(22) Wang, J.; Tang, J.; Guo, T.; Zhang, S.; Xia, W.; Tan, H.; Bando, Y.; Wang, X.; Yamauchi, Y. C_3N_4-Digested 3D Construction of Hierarchical Metallic Phase MoS_2 Nanostructures. *J. Mater. Chem. A* **2019**, *7*, 18388–18396.

(23) Du, X.; Zou, G.; Wang, X. Controllable and Scalable Synthesis of Ordered Mesoporous Silica Nanosheets by Using Acidified g-C_3N_4 as a Lamellar Surfactant. *Nanotechnology* **2017**, *28*, 29LT01.

(24) Shen, Z.; Cai, Q.; Yin, C.; Xia, Q.; Cheng, J.; Li, X.; Wang, Y. Facile Synthesis of Silica Nanosheets with Hierarchical Pore Structure and Their Amine-Functionalized Composite for Enhanced CO_2 Capture. *Chem. Eng. Sci.* **2020**, *217*, 115528.

(25) Liang, S.; Zhou, Y.; Wu, W.; Zhang, Y.; Cai, Z.; Pan, J. Preparation of Porous CuO Nanosheet-Liked Structure (CuO-NS) Using C_3N_4 Template with Enhanced Visible-Light Photoactivity in Degradation of Chlortetracycline. *J. Photochem. Photobiol. A* **2017**, *346*, 168–176.

(26) Yu, H.; Shang, L.; Bian, T.; Shi, R.; Waterhouse, G. I. N.; Zhao, Y.; Zhou, C.; Wu, L.-Z.; Tung, C.-H.; Zhang, T. Nitrogen-Doped Porous Carbon Nanosheets Templated from g-C_3N_4 as Metal-Free Electrocatalysts for Efficient Oxygen Reduction Reaction. *Adv. Mater.* **2016**, *28*, 5080–5086.

(27) Yu, Y.; Chan, Y. M.; Bian, Z.; Song, F.; Wang, J.; Zhong, Q.; Kawi, S. Enhanced Performance and Selectivity of CO_2 Methanation over g-C_3N_4 Assisted Synthesis of Ni–CeO_2 Catalyst: Kinetics and DRIFTS Studies. *Int. J. Hydrogen Energy* **2018**, *43*, 15191–15204.

(28) Alhajri, N. S.; Anjum, D. H.; Takanabe, K. Molybdenum Carbide–Carbon Nanocomposites Synthesized from a Reactive Template for Electrochemical Hydrogen Evolution. *J. Mater. Chem. A* **2014**, *2*, 10548–10556.

(29) Jiang, X.; Lu, W.; Li, Y.; Yu, Y.; Zhou, X.; Liu, X.; Xing, Y. An Eco-Friendly Nitrogen

Source for the Preparation of Vanadium Nitride/Nitrogen-Doped Carbon Nanocomposites for Supercapacitors. *ChemElectroChem* **2019**, *6*, 3445–3453.

(30) Wei, Q.; Wang, J.; Shen, W. Atomically Dispersed Feδ^+ Anchored on Nitrogen-Rich Carbon for Enhancing Benzyl Alcohol Oxidation through Mott-Schottky Effect. *Appl. Catal. B* **2021**, *292*, 120195.

(31) Birdsong, B. K.; Hoogendoorn, B. W.; Nilsson, F.; Andersson, R. L.; Capezza, A. J.; Hedenqvist, M. S.; Farris, S.; Guerrero, A.; Olsson, R. T. Large-Scale Synthesis of 2D-Silica (SiO_x) Nanosheets Using Graphene Oxide (GO) as a Template Material. *Nanoscale* **2023**, *15*, 13037–13048.

(32) Xu, J. F.; Ji, W.; Shen, Z. X.; Tang, S. H.; Ye, X. R.; Jia, D. Z.; Xin, X. Q. Preparation and Characterization of CuO Nanocrystals. *J. Solid State Chem.* **1999**, *147*, 516–519.

(33) Scherrer, P. Bestimmung der Größe und der inneren Struktur von Kolloidteilchen mittels Röntgenstrahlen. *Nachr. Ges. Wiss. Goettingen, Math.-Phys. Kl.* **1918**, *1918*, 98–100.

(34) Jeong, H. Y.; Lee, J. H.; Hayes, K. F. Characterization of Synthetic Nanocrystalline Mackinawite: Crystal Structure, Particle Size, and Specific Surface Area. *Geochim. Cosmochim. Acta* **2008**, *72*, 493–505.

(35) Tong, T.; Zhang, J.; Tian, B.; Chen, F.; He, D.; Anpo, M. Preparation of Ce–TiO_2 Catalysts by Controlled Hydrolysis of Titanium Alkoxide Based on Esterification Reaction and Study on Its Photocatalytic Activity. *J. Colloid Interface Sci.* **2007**, *315*, 382–388.

(36) Ma, M.; Djanashvili, K.; Smith, W. A. Selective Electrochemical Reduction of CO_2 to CO on CuO-Derived Cu Nanowires. *Phys. Chem. Chem. Phys.* **2015**, *17*, 20861–20867.

(37) Shima, M.; Tsutsumi, K.; Tanaka, A.; Onodera, H.; Tanemura, M. Chemical State Analysis Using Auger Parameters for XPS Spectrum Curve Fitted with Standard Auger Spectra. *Surf. Interface Anal.* **2018**, *50*, 1187–1190.

(38) Biesinger, M. C. Advanced Analysis of Copper X-ray Photoelectron Spectra. *Surf. Interface Anal.* **2017**, *49*, 1325–1334.

(39) Magi, M.; Lippmaa, E.; Samoson, A.; Engelhardt, G.; Grimmer, A. R. Solid-State High-Resolution Silicon-29 Chemical Shifts in Silicates. *J. Phys. Chem.* **1984**, *88*, 1518–1522.

(40) Leonardelli, S.; Facchini, L.; Fretigny, C.; Tougne, P.; Legrand, A. P. Silicon-29 NMR Study of Silica. *J. Am. Chem. Soc.* **1992**, *114*, 6412–6418.

(41) Thommes, M.; Kaneko, K.; Neimark, A. V.; Olivier, J. P.; Rodriguez-Reinoso, F.; Rouquerol, J.; Sing, K. S. W. Physisorption of Gases, with Special Reference to the Evaluation of Surface Area and Pore Size Distribution (IUPAC Technical Report). *Pure Appl. Chem.* **2015**, *87*, 1051–1069.

(42) Wang, P.; Gou, X.-X.; Xin, S.; Cao, F.-F. Facile Synthesis of CuO Nanochains as High-Rate Anode Materials for Lithium-Ion Batteries. *New J. Chem.* **2019**, *43*, 6535–6539.

(43) Gund, G. S.; Dubal, D. P.; Dhawale, D. S.; Shinde, S. S.; Lokhande, C. D. Porous CuO Nanosheet Clusters Prepared by a Surfactant Assisted Hydrothermal Method for High Performance Supercapacitors. *RSC Adv.* **2013**, *3*, 24099–24107.

(44) Shao, Q.; Wang, X.; Liu, Q.; Wang, L.; Kang, C.; Wang, Q.; Ge, S. Preparation and Photocatalytic Property of Porous CuO Hollow Microspheres via Carbon Sphere Templates. *J. Nanosci. Nanotechnol.* **2011**, *11*, 10271–10277.

(45) Kim, K.; Choi, P. G.; Itoh, T.; Masuda, Y. Effect of Coordinatively Unsaturated Sites in MOF-Derived Highly Porous CuO for Catalyst-Free ppb-Level Gas Sensors. *Adv. Mater. Interfaces* **2021**, *8*, 2100283.

(46) Wang, Q.; Zhou, Y.; Zhang, K.; Yu, Y.; Luo, Q.; Gao, S.; Xie, Y. Defect-Enrichment in Porous Interface of Ultrathin CuO Nanobelts Realizes a Novel CO_2 Photoreduction Pathway. *J. Mater. Chem. A* **2023**, *11*, 8776–8782.

(47) Manna, S.; Das, K.; De, S. K. Template-Free Synthesis of Mesoporous CuO Dandelion Structures For Optoelectronic Applications. *ACS Appl. Mater. Interfaces* **2010**, *2*, 1536–1542.

(48) Jia, Z.; Yue, L.; Zheng, Y.; Xu, Z. The Convenient Preparation of Porous CuO via Copper Oxalate Precursor. *Mater. Res. Bull.* **2008**, *43*, 2434–2440.

(49) Takahashi, R.; Sato, S.; Sodesawa, T.; Kato, M.; Yoshida, S. Preparation of Cu/SiO_2 Catalyst by Solution Exchange of Wet Silica Gel. *J. Sol–Gel Sci. Technol.* **2000**, *19*, 715–718.

(50) Niu, X.; Zhao, T.; Yuan, F.; Zhu, Y. Preparation of Hollow $CuO@SiO_2$ Spheres and Its Catalytic Performances for the NO + CO and CO Oxidation. *Sci. Rep.* **2015**, *5*, 9153.

(51) Costas, A.; Florica, C.; Preda, N.; Besleaga, C.; Kuncser, A.; Enculescu, I. Self-Connected CuO–ZnO Radial Core–Shell Heterojunction Nanowire Arrays Grown on Interdigitated Electrodes for Visible-Light Photodetectors. *Sci. Rep.* **2022**, *12*, 6834.

(52) Hamad, H.; Elsenety, M. M.; Sadik, W.; El-Demerdash, A.-G.; Nashed, A.; Mostafa, A.; Elyamny, S. The Superior Photocatalytic Performance and DFT Insights of S-Scheme CuO@TiO_2 Heterojunction Composites for Simultaneous Degradation of Organics. *Sci. Rep.* **2022**, *12*, 2217.

(53) Rashad, M. M.; Soltan, S.; Ramadan, A. A.; Bekheet, M. F.; Rayan, D. A. Investigation of the Structural, Optical and Magnetic Properties of CuO/$CuFe_2O_4$ Nanocomposites Synthesized via Simple Microemulsion Method. *Ceram. Int.* **2015**, *41*, 12237–12245.

(54) Rahimabadi, Z.; Bagheri-Mohagheghi, M. M.; Shirpay, A. Synthesis, Characterization, and the Study of Structural and Optical Properties of Core/Shell Nanoparticles of SiO_2@CuO for Solar Absorption Collectors Application. *J. Mater. Sci.: Mater. Electron.* **2022**, *33*, 7765–7780.

(55) Sharma, S.; Basu, S. Construction of an Efficient and Durable Hierarchical Porous CuO/SiO_2 Monolith for Synergistically Boosting the Visible-Light-Driven Degradation of Organic Pollutants. *Sep. Purif. Technol.* **2021**, *279*, 119759.

Chapter 5. Concluding remarks

Nanoporous materials were designed through substance formation on two-dimensional materials, such as carbon, oxide, and polymers, using calcination and employing these two-dimensional materials and polymers as templates and structure-directing agents. In addition, the phenomena induced in the two-dimensional materials and their formation processes were discussed in the chapters (research content).

Chapter 1 described the introduction of nanoporous materials and two-dimensional materials [nanosheets (laminates)], evaluation methods for pore structures, templated synthesis, and the purpose of this study.

In Chapter 2, GO was used as a template to control silica formation. Silica nanosheets were synthesized by modifying a silica precursor on the GO surface and subsequently calcining to simultaneously induce *in situ* silica formation on the GO surface and GO template removal. In precursor preparation, the presence of amino groups contributed to the modification of the silica precursors to GO in this preparation system. The synthesized silica nanosheets had excellent properties, including an ultrathin thickness (approximately 1 nm) and a high specific surface area (approximately 900 $m^2\ g^{-1}$).

Chapter 3 used a polymer template (PEI) to control CuO_x formation on activated clay. After introducing the PEI–Cu^{2+} complex into the clay, CuO_x formation and PEI removal were induced by calcination to form the CuO_x/clay nanocomposite. The amount of the PEI–Cu^{2+} complex (PEI) introduced into the clay was changed by changing the Cu^{2+}/PEI ratio, and the introduced amount of the complex (PEI) decreased as the Cu^{2+}/PEI ratio increased. In addition, changing the Cu^{2+}/PEI ratio could change the supported amount and size of CuO_x on the clay. When the Cu^{2+}/PEI ratio was small, the formed CuO_x nanoparticles tended to be small.

In Chapter 4, carbon nitride was used as a structure-directing agent to simultaneously induce CuO and silica (SiO_2) formation. In Section 4-1, the silica/g-C_3N_4 nanocomposite, with higher porosity and wider visible-light adsorption performance than g-C_3N_4, was constructed by calcining carbon nitride and PSS [POSS (SiO_2 precursor) and quaternary ammonium cations] only. In Section 4-2, CuO and SiO_2 formation and carbon nitride removal by Cu species were induced

by calcining a mixture of carbon nitride, Cu^{2+}, and POSS (PSS), and nanoporous CuO–SiO_2 nanocomposites were synthesized. The SiO_2 formation process played an important role in the enhancement of porosity and controlled the morphology of the CuO–SiO_2 nanocomposites. The synthesized CuO–SiO_2 nanocomposites exhibited a high specific surface area and unique structures (CuO supported on top of fluffy SiO_2).

Consequently, the nanoporous materials were synthesized by taking advantage of the characteristics of each two-dimensional material, including carbon, oxides, and polymers. In particular, this study demonstrated that the two-dimensional materials which can be removed with the calcination in an air atmosphere, such as GO, can be used as structure-directing agents and templates to simultaneously induce substance formation and template removal during calcination, enabling the synthesis of nanoporous materials with the desired composition. In addition, two-dimensional materials with thermal stability, such as clay, can be used as carriers for substance formation during calcination to functionalize the surface structure.

The content of this study can contribute to the construction of nanoporous (nanostructured) materials and nanocomposites with unique structures, such as those composed of ultrathin sheets, and the development of nanoporous materials with high porosity and excellent surface structure. Furthermore, this study focused on silica (SiO_2) and CuO; however, there is a possibility that the proposed synthesis concept can be applied to various other materials as there are precedents. Although the exploration of the application of the synthesized materials could not be fully conducted, this study may develop the application of nanoporous materials.

List of publications

Publications related to this dissertation

Chapter 2

1. Takeuchi, Y.; Obata, S.; Ohkura, K.; Nishina, Y. In Situ Synthesis of Ultrathin Amorphous Silica Nanosheet with Large Specific Surface Area on Graphene Oxide. *ACS Materials Lett.* **2022**, *4*, 2590–2596.

Chapter 3

2. Takeuchi, Y.; Ohkubo, T. Polymer Template Synthesis of CuO_x/Clay Nanocomposites with Controllable CuO_x Formation. *ChemistrySelect* **2023**, *8*, e202301644.

Chapter 4

3. Takeuchi, Y.; Toyoda, Y.; Gotoh, K.; Ohkubo, T. Structure-Directing Synthesis of Porous CuO–SiO_2 Nanocomposites Using Carbon Nitride. *CrystEngComm* **2024**, *26*, 3044-3053.

Other publication

1. Takeuchi, Y.; Ohkura, K.; Nishina, Y. Self-Assembly Strategies for Graphene Oxide/Silica Nanostructures: Synthesis and Structural Analysis. *Bull. Chem. Soc. Jpn.* **2023**, *96*, 113–119.

Acknowledgments

This paper summarized the results of research at the Graduate School of Science and Technology, Okayama University. I would like to express my gratitude to everyone involved in this research.

I would like to express my deepest gratitude to Prof. Takahiro Ohkubo (Okayama University) for providing research resources, discussing about the research, and performing the office procedures.

I appreciate Prof. Yasushige Kuroda (Okayama University) for his advice and discussion on the direction of my doctoral research. I thank the members of Inorganic Chemistry Laboratory at Okayama University for discussion.

I would like to express my gratitude to Prof. Tsutomu Ono, his lab member, and Prof. Takaichi Watanabe (Okayama University) for teaching me how to write reports and sentences, the manner for research in the bachelor's and master's programs. I appreciate Prof. Takaichi Watanabe for sharing his knowledge of the doctoral program as a senior who has experienced it.

I would like to appreciate Prof. Yuta Nishina and his lab member (Okayama University) for providing us the resources for research and GO, discussing about the research, providing guidance on how to write academic papers, and conducting applied research of silica nanosheets.

I would like to express my gratitude to Prof. Kazuma Gotoh and Mr. Yasuhiro Toyoda (Japan Advanced Institute of Science and Technology (JAIST)) for the measurements of NMR and discussions on the results.

I would like to express the gratitude to Prof. Tatsuo Fujii and his group members (Okayama University) for the support in using BELSORP-mini.

I thank Prof. Takashi Kambe and his group members (Okayama University) for their support in using SEM (VE-9800)-EDX (971863SP).

I appreciate Dr. Chiyuu Nakano (Okayama University) for conducting the entrusted measurement of XPS.

TEM and STEM-EDX meaurements were supported by "Advanced Research Infrastructure for Materials and Nanotechnology in Japan (ARIM)" of the Ministry of Education, Culture, Sports,

Science and Technology (MEXT) under Grant Number JPMXP1223JI0011 and JPMXP1223JI0054.

I would like to express my gratitude to Prof. Hisashi Machida (Okayama University) for consulting about my career during my master's and doctoral programs, and for teaching me the manner for spending time as a researcher and a member of society.

This work was supported by JST, the establishment of university fellowships towards the creation of science technology innovation, Grant Number JPMJFS2128 and JST SPRING, Grant Number JPMJSP2126. In addition, I would like to express my deepest gratitude to Okayama University Science and Technology Innovation Fellowship (OU Fellowship) and Okayama University Support for Research Initiated by the Next Generation (OU-SPRING) for holding interviews about research and seminars on research skills.

I would like to express the deepest gratitude to the Public Interest Incorporated Foundation ”Ohmoto Ikueikai” for their generous financial support over the past 3 years in carrying out this research.

Finally, I would also like to express my heartfelt gratitude to my friends, relatives, and family who have supported me in various aspects such as health and mental.

The Author

Yuki Takeuchi
Graduate School of Natural Science and Technology,
Okayama University
3-1-1, Tsushima-naka, kita-ku, Okayama 700-8530
Japan
March 2025